DOSHISHA UNIVERSITY

DOCTORAL THESIS

Characterization of target cavity confined plasmas produced by nanosecond laser pulses

Author:
James Edward Aquino Hernandez II

Supervisor:
Motoi Wada

A thesis submitted in fulfillment of the requirements for the Doctor of Philosophy

in

Electrical and Electronic Engineering

July 2022

Acknowledgements

First, I would like to thank Doshisha University, MEXT, and GRM programs for this opportunity to study in Japan. It is with great pleasure to have experienced learning in Japan and acclimating to a foreign culture while expanding my career avenues.

I would like to express my gratitude to my professor Motoi Wada, who has supported me in research ever since my Master's degree here in Doshisha. I would not have reached this point, nor would I have the confidence and skills to pursue this degree if not for his advice related to things within and outside research.

I would like to thank Dr. Kengo Moribayashi and Dr. James Koga of QST, as well as Dr. Naoki Miyamoto of Nissin Ion Equipment Ltd., for letting me experience internship and field research during my doctoral program. I have learned a lot from the methods, and I have adopted some of them in my current endeavors.

To the Global Resource Management Program professors: Ueda-sensei, Oyamada-sensei, and Okamoto-sensei, thank you very much for making me experience the opportunity of learning beyond that is required of my degree, while gaining understanding on how to develop infrastructures and communities bearing a social perspective.

I would like to thank the members of Plasma Physics Laboratory who formed me through the years as a student. Ever since 2017, all of you whom I struggled and spent time with, contributed to my perspectives about the reality of living as an international student. I may have some ups and downs, but in the end I have enjoyed my time in the lab with you guys. To my lab mates Glynnis and Jhoelle, thank you for all peculiar assistance. To Kim, Arnold, Anton, Jojee, Nica, Don, Allen, Keano, Ali, Oli, Jigo, Jarl, and Dane, thank you for making me feel at home while being here in Japan. To Sir Christian Mahinay, sir Ivan Culaba, and sir Mike Jallorina, thank you for supporting me, and all the MEXT scholars during our entry and stay in the laboratory.

To ISTC professors, as well as office staffs: Matsukawa-sensei, Yamane-sensei, Toda-sensei, Okita-san, Hida-san, Naoi-san, and other staffs I worked during the past university projects, thank you for assisting me and my group members in accomplishing school-wide outputs which deemed useful for the university and our lives as well. Thank you also for assisting me and fellow international students in times of dire need.

To the international student friends in Japan, thank you for the times you have spent with me–for all the meaningful conversations, the insights, and shared experiences that I learned from you. To my friends in the Philippines and all over the world, thank you for being my inspiration to work better and smarter in furthering my career.

To fellow staff in ULU: Yuko-san, Fumi-san, Seika, Isma, William, Kei, Ollie, Chai, Tei-kun, Amanda, Yunan, as well as staffs Oskar and Ayushi, thank you for letting me work with you. From the diverse activities we have done for almost two years, I get to experience the fun and wholesome

environment of Japan, while learning life skills as well. I also get to appreciate the little things from which big ones emerge. I am grateful for these wonderful people.

To office and student staffs from Saturday school: Mike, Chihiro, Yui, Maryam, Souka, Shouq, and other staffs: I am grateful for the experiences from working with you guys.

To Director Ikeda, who helped me gain perspectives in business and in research.

To my family and friends back home, thank you for keeping close contact with me and supporting me materially and emotionally. Despite being away, constant communication has kept me close as if I were there.

To myself, who has came thus far after all the planned and haphazard life decisions, as well as after all the consequences of such. Excellence should always be pursued with sympathy.

Finally, to the One Who has never failed to ultimately provide hope from hopelessness, recovery from bad choices, and existence from nothingness, I would have no expectations left as You have already exceeded them and all possibilities ever thinkable, and otherwise.

Synopsis

Laser ablation is employed in applications such as mass spectrometry. Laser ablation consists of electron, ion, and neutral production, which comprises of three main parameters: incident laser, target material, and background environment. Changing one of such parameters, or a subset of each, would result to a significantly different result due to the complex laser-target interactions. The main mechanisms involved in laser ablation involve electron and ion production, plasma expansion, as well as plume propagation.

A time-of-flight spectrometer is developed to investigate the influence of confining the laser produced plasma in a small region, utilizing the target itself. When the plasma is initiated within the small cavity, the plasma density increases, also increasing the collision probability. Electrons, ions, and neutrals participate in the collisions within the inner cavity wall and is effectively cooled down, resulting to energy losses.

The dissertation is divided into seven chapters. For the first chapter, fundamentals of laser ablation, as well as applications towards sample characterization are discussed. Time-of-flight spectrometry and retarding potential analysis are described. The second chapter discusses the development of the cavity laser ion source, and preliminary time-of-flight experiments as well as those employing the retarding potential analyzer. During these test experiments, ion current distribution was detected, and electron suppression was achieved using 250 G magnets near the Faraday cup collector array. Retarding potential analysis resulted to a 250 eV energy. High speed measurements were also performed for which speeds of 110 m/s were observed for the particles following the time of plasma afterglow.

The third chapter involves the electron production of nanosecond plasmas. Electron production following Keldysh multiphoton ionization is simulated. Near target charge collection experiments are performed, and the electron signal is described as a Maxwellian distribution. Increasing number of pulses showed an electron energy loss of 0.7 eV after 10000 pulses ablation.

The fourth chapter discusses the positive and negative ion production of cavity confined plasmas. In this chapter, the influence of the magnetic field on the time of flight signals is investigated. Trajectory simulations under the influence of a magnetic field are performed, resulting to a mass of C_2^+ under a magnetic flux density of 300 G. Then, a magnetic deflector flange is designed to steer the propagating ions away from the target axis, resulting to a collected ion current of around 20 μA. Simulations on the refocusing of the laser produced ions were performed, which showed focusing at a lens-to-ion energy ratio approximately 0.1. An electrostatic lens is then designed, which showed a significant decrease in ion current for lens bias above 50 V. Retarding potential analysis of the positive ion current are performed, where the energy of the distribution is approximately 250 eV. Increasing number of laser shots contributes to ion energy loss, which is up to 150 eV is observed for increasing laser shots. Experiments for negative ion production are performed for varying extraction plate voltages. Increasing number of laser pulses results to the formation of large negative clusters such as C_{26}^- and C_{35}^-.

The fifth chapter discusses the optical spectroscopy of the confined laser plasmas. Optical emission of the plasma is directed parallel, as well as perpendicular to the target axis on both carbon and aluminum targets. Emission spectra consisted of charges up to C IV and Al IV, and continuum enhancement of carbon continuum after 6000 pulses were observed. Further increasing the number of pulses resulted to decrease in continuum as well as emission line signal. Decrease in emission line signal for both carbon and aluminum are observed for increasing number of laser shots. Fits were performed on the continuum spectra and obtained an apparent temperature of 3000 K.

For the sixth chapter, pulsed laser deposition experiments were performed and discussed. Deposited carbon thin films showed microcone formation and amorphous film, at 4 mm and 8 mm target-to-substrate distances, respectively. Increasing number of pulses produces smaller spherical deposits. Spherical deposits with nm to μm order sizes are also observed at a substrate distance of 100 mm. Chapter seven states the main results, as well as future work.

Contents

List of Figures

List of Tables

Chapter 1

Introduction

1.1 Laser Ablation

1.1.1 Plasma formation via pulsed laser

Laser ablation is described as the evaporation of a material, called a target, with an incident high-powered laser. When a high-powered laser strikes a solid surface which exceeds its vaporization threshold, several mechanisms may occur depending on the incident laser, target, and the background environment. These processes involve material evaporation and plasma formation. Plasma formation via a pulsed laser consists of a transient discharge, thereafter termed as a 'plasma plume'. In the initial stages of plasma formation, electrons are first ejected from the surface due to the ionized target. These electrons were described to be coming from either thermionic emission or photoelectric effect [1]. Laser-target interaction resulting to electron ejection and ion production at this stage highly depends on the laser intensity and photon energy, which is discussed further in Chapter 3. Then, a condensed gas is formed representing the vaporised solid. At this time, a number of mechanisms such as Coulomb explosion (CE) where a charge separation occurs between ions. In CE, electrons are stripped off from the target, producing a charge separation with the surface. The target atoms become positively charged, and when the force due to the repulsion between the positive ions and nuclei exceed the bond energy, the ions explode into a plasma [2].

Within the condensed gas, the electrons ionize the ablated atoms through collisions via electron impact (EI). An ablation spot is formed on the target, from which the plume expands radially outward, with the motion primarily directed perpendicular to the target surface. As the plume expands, a shockwave front also forms due to the abrupt difference in pressure, whose velocities fall well above sound speed [3]. Figure 1.1 shows the various mechanisms involved in laser ablation. The plume expansion is sustained in the order of μs. Along with the plume expansion, the plasma emits radiation due to electron-ion recombination. Moreover, laser ablation also involves the formation of clusters. Processes such as condensation and agglomeration between the ions and neutral atoms occur from the vaporized solid thereby forming larger atomic clusters [4]. These processes which are involved in laser plasma formation, plume production and propagation all occur in less than 1 ms.

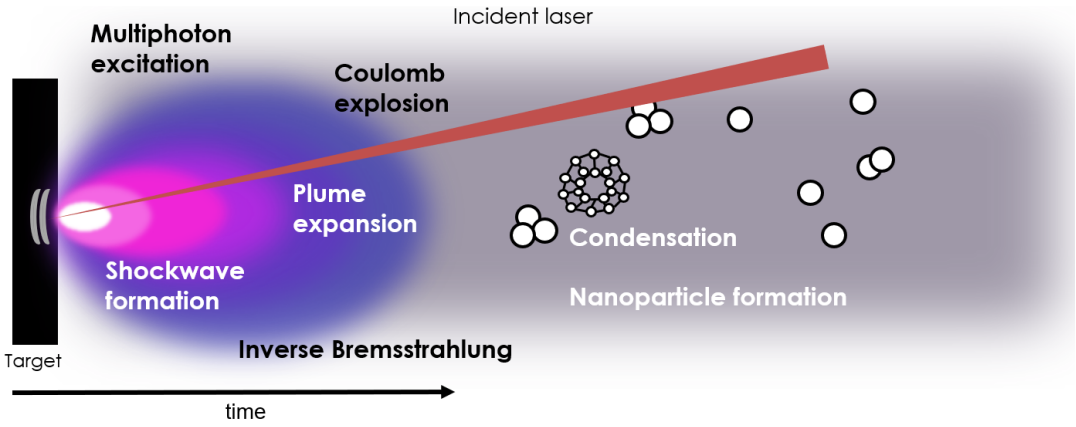

FIGURE 1.1: Mechanisms involved in pulsed laser ablation

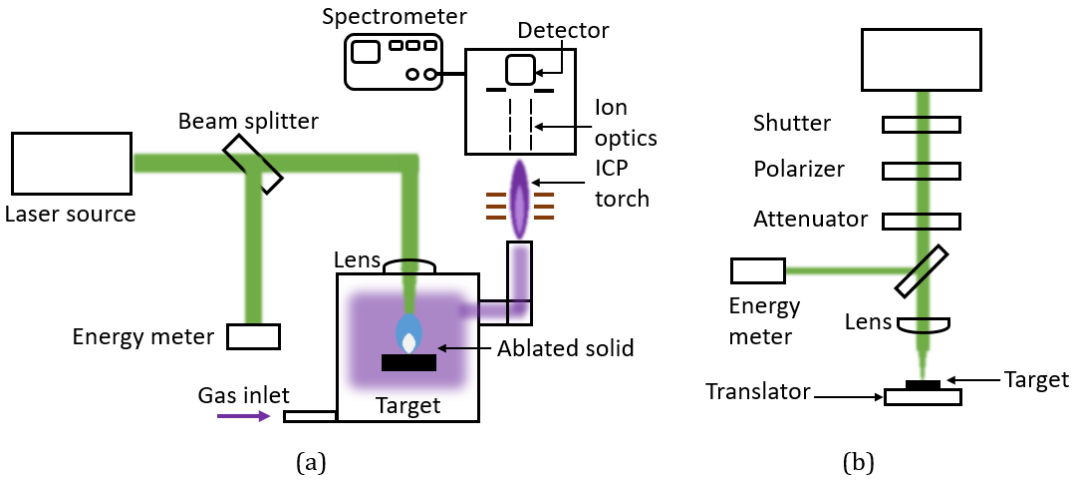

FIGURE 1.2: (a) LA-ICP-MS schematic, and (b) laser ablation schematic for microstructuring

1.1.2 Applications of laser ablation

Laser ablation has been employed in various applications ranging from elemental analysis to nanostructuring [5]. In elemental analyses, the laser plasma plume is characterized by analyzing the light coming from the plume. In the review paper of Russo, the plasma characteristics are determined by directing the optical emission of the laser produced plasma towards a high speed spectrometer through a converging lens [6]. With the collected emission spectra, the characteristics of ions whose emission intensity signifies the ion recombination processes can be identified. As the collection is time-resolved, the evolution of the corresponding ion recombination within the plume can be determined. In particulate analyses, the ablated particles in vacuum are introduced into a separate chamber containing an inductively coupled plasma (ICP) source. This setup is then known as laser ablation inductively coupled plasma mass spectrometer (LA-ICPMS), where the ICP ionizes the produced aerosols for mass analyses. One example is the analyses of uranium isotopes via LA-ICP-MS where highly enriched uranium (HEU) was detected among other particles such as copper

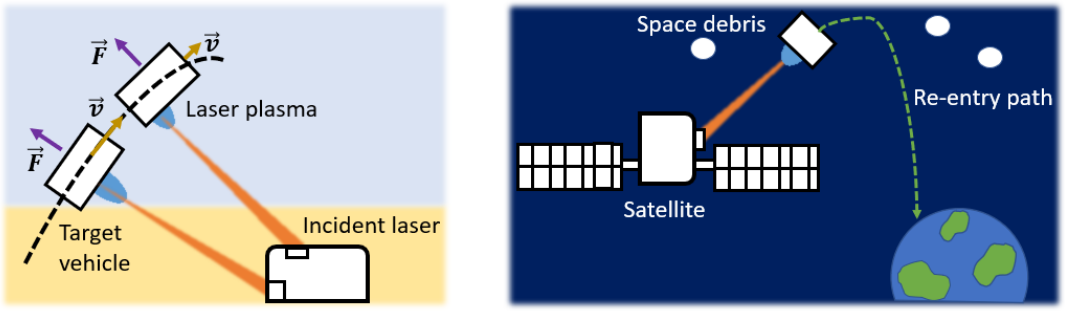

(a) (b)

FIGURE 1.3: Schematic of laser ablation for (a) propulsion, and (b) de-orbiting of space debris

and iron oxides [7]. On the other hand, microstructuring via laser ablation involves modifying the target surface with pulsed, high repetition rate laser sources. The motivation for this structural modification mainly involves the improvement of material mechanical properties such as hydrophilicity [8]. In the study of Yorobyev and Guo, a direct laser ablation source via femtosecond pulse irradiation is employed, which resulted in periodic structures in titanium and tungsten [9]. Figure 1.2 shows the schematic diagrams for LA-ICP-MS and schematics for target microstructuring.

Due to the advantage that laser induced plasma only requires a high power laser source and a target material, laser ablation found other applications in space, including propulsion and clearing of space debris. Some of the potential uses of ablation lasers in these aspects are reported in a paper of Gibbings and others [10]. In terms of propulsion, a gas with an appropriate atmospheric pressure is irradiated with a high-intensity laser, leading to a thrusting force which propels the object towards the incident impulse direction [11]. The target trajectory may be steered depending on the location of the ablation spot. In regards to de-orbiting of space debris, a report by Vasile and Maddock proposed a satellite equipped with concentrators which focuses light which redirects the path of space debris towards the earth [12].

1.2 Factors affecting laser plasma characteristics

As mentioned in the previous section, laser plasma characteristics highly depend on the laser specifications, as well as the background environment in which the plasma is initiated. Moreover, the target material dependence also provides information on the interaction between the laser and solid. Here these dependencies are briefly summarized.

1.2.1 Laser specifications

Factors related to the incident laser include the pulse duration, laser intensity, and wavelength. The ablation laser is classified into long ($\tau_l \approx$

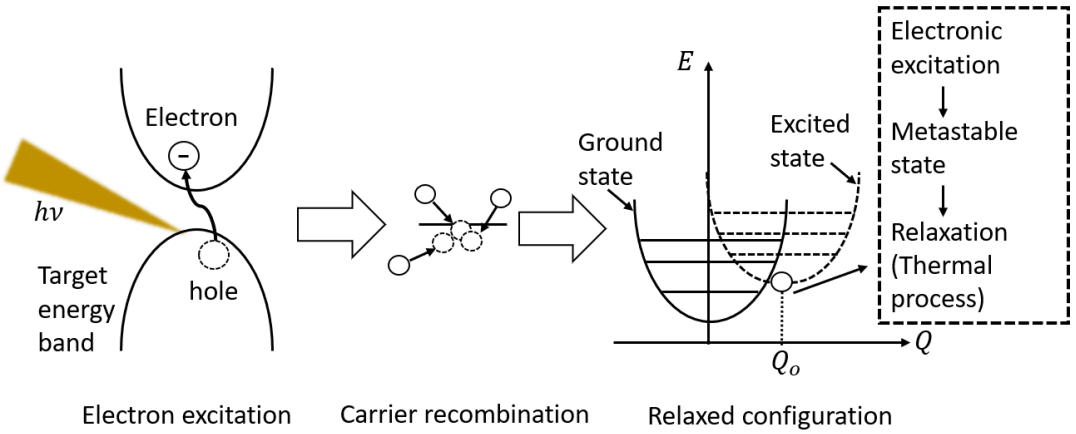

FIGURE 1.4: Excitation and relaxation processes leading to ablation

ns), short ($\tau_l \approx$ ps), and ultrashort ($\tau_l \approx$ fs) laser pulses. Interactions where the pulse width plays a crucial role is stated in terms of electron-phonon processes [14], where a possible mechanism is briefly described in the following. When the laser strikes the surface, the incident energy from the laser is transferred to the conduction band electrons. The valence electrons then are photoexcited and an electron-hole pair forms. The electron hole pair can either radiatively recombine and emit light, or undergo relaxation. The latter involves scattering and localized capture of free carriers towards defect sites. This localized capture, a nonradiative recombination process, involves the energy transfer from the recombining electron to localized modes in the lattice. The transfer to localized lattice modes is a metastable, thermal process and result to particle emission and ablation through an anti-bonding potential energy surface. Figure 1.4 shows the mechanism of excitation leading to excitation and subsequent relaxation. The rightmost figure shows the adiabatic potential energy surface [14] whose minimum is below the ground state band. This process of thermalization due to scattering lasts in the order of ps. This indicates, when the laser pulse is of ns order, heating due to the laser significantly contributes to the target dissociation. While for fs laser pulses, the effect of heating is ignored as the pulse duration is much smaller than the thermlization time. In terms of ablation thresholds, longer pulse duration results to increased ablation thresholds [15].

Higher laser intensity increases the available photons for irradiation and ablation, whereas when the intensity is too low, target vaporization may not even occur. In the regime above the laser vaporization threshold, the electromagnetic energy due to the laser is transferred to the electrons which are propelled in a form of thermal expansion. This is in the case of a nanosecond-pulse laser produced plasmas, where a thermalization time exists. The electron temperature T_e is then related to the intensity by [13]:

$$T_e \propto It/l, \tag{1.1}$$

where I is the laser intensity, t is the laser pulse duration, and l is the

penetration depth on the target. The intensity also influences the material evaporation, wherein the threshold at strong evaporation is given by [13]:

$$I_{th} \propto \frac{\rho\Omega\sqrt{D}}{\sqrt{\tau}}, \tag{1.2}$$

where ρ, Ω, D, τ are the target density, heat of vaporization, diffusion coefficient, and pulse width, respectively.

Apart from the laser pulse duration, the wavelength significantly contributes to the characteristics of the plasma via the photon energy. When the photon energy $h\nu$ is less than the bandgap energy, the laser energy is not efficiently coupled to the target, and the main mechanisms involved are the absorption of the laser energy by the free electrons in the plasma, known as inverse Bremmstrahlung (IB) process, whose coefficient is given by [16]:

$$\alpha_{IB} = \sigma_{IB} N_e \propto \frac{1}{\nu^3}\left(1 - \exp\frac{h\nu}{k_B T_e}\right), \tag{1.3}$$

where N_e is the electron density, ν is the frequency, k_B is the Boltzmann constant, T_e is the electron temperature. For lower wavelengths, IB is not efficient. Rather the main mechanism involved is photoionization (PI). For a photon energy exceeding the work function of the target, electrons are directly generated via PI, given a sufficient intensity. The PI cross section α_{PI} is almost proportional to $(h\nu^3)$. Still, these two processes occur simultaneously, and in order to separate the two mechanisms, a sufficiently short-wavelength laser may be required.

1.2.2 Background environment

The background environment includes ambient pressure in which the laser plasma is initiated. In the study of Zehra et. al, the emission spectra of the laser produced plasma is investigated when inert gases argon, helium, and neon are injected to the vacuum chamber in order to control the ambient pressure [17]. In their report, an initial increase, followed by a subsequent decrease in temperature was observed, which was suggested to be due to the plasma expansion and electron-ion collisions. The pressure increase confines the plasma and increases the collision frequency within the constituents. Pressure variation affects the temperature, where at lower pressure, the plasma contributes to lower absorption of laser light via inverse Bremmstrahlung. The presence of buffer gas also acted as an absorber of laser light, along with the laser-produced vapor. A similar explanation was provided by Bashir and coworkers, where they investigated pressure variation effects on laser ablated cadmium via the plasma emission and morphology of the produced films [18]. At higher pressures, the plasma expansion is confined near the target surface as the expansion is hindered by the ambient. The ambient atmosphere also contributes to inelastic collisions with the laser produced plasma. Harilal and others performed experiments involving fast imaging of ns- and fs- laser ablated plumes at

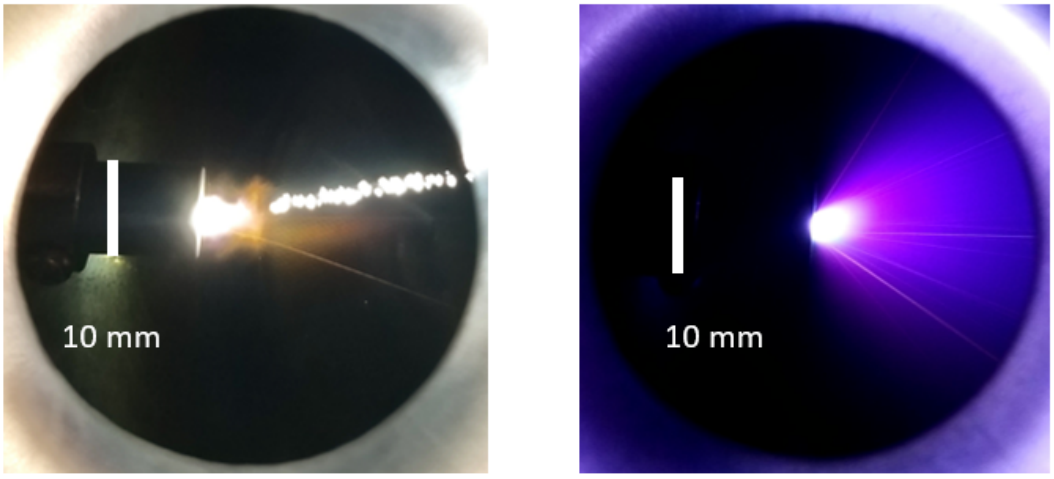

FIGURE 1.5: Comparison of repetitive laser ablation of graphite (a) ambient air (b) vacuum at 1×10^{-5} Pa pressure

various ambient pressures via intensified charge coupled device (ICCD) [19]. In their results, the plume emission produced via ns laser ablation exhibits higher persistence than the fs counterpart due to the increased coupling with the laser and plasma leading to breakdown. Increasing the pressure from high vacuum showed the transition from free expansion towards the plume confinement near the target surface. The ambient gas also played a part in the plasma heating due to inverse Bremmstrahlung, which was to increase melting and vaporization on the target surface.

An experiment is performed in comparing the plasma plume image at ambient and high vacuum conditions. A neodymium:YAG laser at 1064 nm wavelength and 5 ns pulse width is incident on a cylindrical graphite target at 12° incidence from its axis. The laser repetition rate is 10 Hz. The result is shown in Fig. 1.5. For both conditions, a bright plume of approximately 5 mm length is observed near the target. In the ambient air condition, the plume is directed along the laser direction. Small bright spots and a thin plasma plume are also observed along the laser direction in this condition. These bright spots indicate the breakdown of air as the laser is incident on the target. In case of vacuum ablation, a conical plume expansion is observed, indicating the free expansion of the laser-produced plasma.

Another factor affecting the laser produced plasma is the obstacle with which the laser plasma interacts. When an obstacle such as a plate is placed near the surface of the target on which the plasma is initiated, electrons and ions in the plasma collide with each other, as well as that obstacle. This work focuses on the effect of the target cavity acting as an obstacle to the laser produced plasma, which will be discussed in detail in Chapter 2.

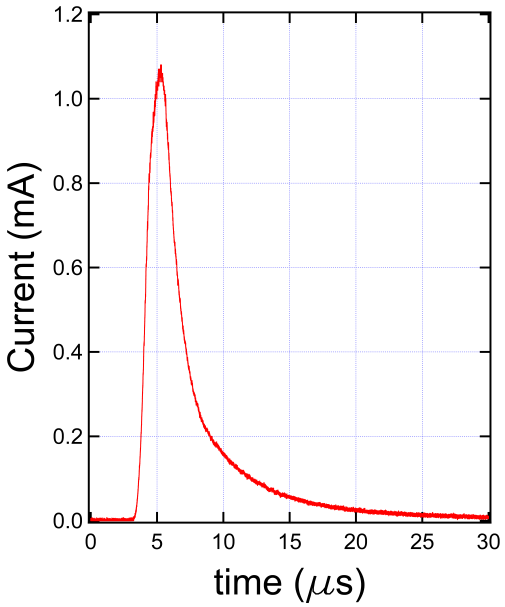

FIGURE 1.6: Time-of-flight spectrum of a laser ablated graphite target, ($\lambda = 1064nm$, pulse width = 5 ns)

1.2.3 Target material

One of the effects of laser ablation is the formation of a small cavity equivalent to the laser spot size. The investigation of the dependence of material properties in plasma formation and surface morphology becomes significant, mainly in laser drilling applications. These material properties include, but not limited to: latent heat of vaporization and fusion, thermal conductivity, absorption coefficient, band gap, specific heat, reflection coefficient, and density. In a study by Marla *et al*, the time evolution of the physical properties of a material with an arbitrary critical temperature and density were modelled, under nanosecond ablation [20]. Beyond a critical temperature after ablation, the material temperature rapidly increased, while absorption coefficient and thermal conductivity decreased. Phase explosion was observed, followed by a constant temperature. In a model by Sinha, where a 5 ns, 532 nm nanosecond pulsed laser is incident on a graphite material, a thermal-based simulation was performed [21]. In this model, the ablation depth is found to increase substantially after approximately 10 ns after the laser pulse is incident on the target, which rapidly cooled within 40 ns. However, this model does not indicate the contributions of electrons and ions in the plasma to the overall temperature, but it showed a convective description of heat transfer from the laser to the target, as well as laser energy absorption. Nevertheless, this model approximated the damage to the target by the laser pulse.

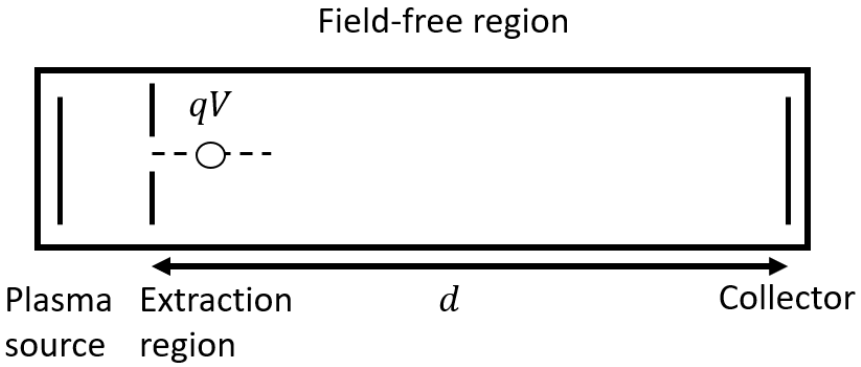

FIGURE 1.7: Schematic of a time-of-flight spectrometer, q is the charge, $V_a is the acceleration voltage$

1.3 Time-of-flight mass spectrometry

One of the challenges in the characterization of laser produced plasmas is that for a single pulse, the target ablation, plasma production, plume expansion, typically lasts for μs order. Therefore, the typical characterization methods such as Langmuir probe in determining the plasma parameters such as electron and ion temperature may not be applied, since such methods require a continuous source of plasma. Therefore, fast collection methods are developed for this purpose. A pulsed mass spectrometer which had been improved for mass dispersion was initially proposed by Stephens in the analyses of hydrocarbon and atmospheric gas species [22]. The method for characterizing these transient ions is called time-of-flight mass spectrometry (TOF). Charged particles from a pulsed source are first accelerated by a high voltage power supply and traverse through a field-free region, which are then collected by the end of the flight tube, as shown in the schematic in Fig. 1.7.

In a pulsed source, given a mass m and charge q, the mass per charge ratio is one of the main parameters measured. For ions travelling at the same energy and momentum with length d and time-of-flight t, and acceleration voltage V, the mass per charge ratio is calculated by [23]

$$t = \frac{d}{(2V_a)^{1/2}}\sqrt{\frac{m}{z}} \tag{1.4}$$

A sample TOF spectrum with 0 V extraction voltage is shown in Figure 1.6. It can be observed that the spectrum here shows a rather broad time distribution, with a peak at 5 μs. This is due to the presence of particles with varying momentum as the laser plasma is produced. Not only momentum, but the plasma constituents also differ by energy and mass. Thus, the need for resolving mass and energy to determine the ion masses arises.

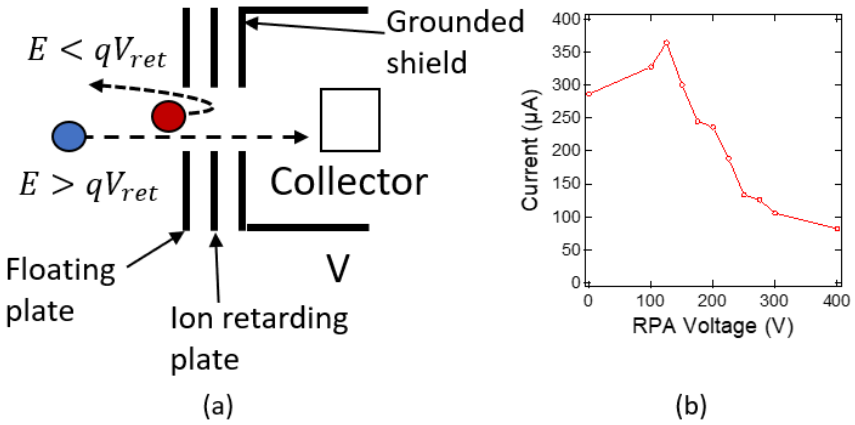

FIGURE 1.8: (a) Schematic of a retarding potential analyzer (b) Ion current versus ion retarding plate voltage of a laser plasma

1.4 Retarding potential analyzer

One of the parameters that enable the understanding of the laser plasma is its ion energy distribution. By identifying the ion energy of the plasma, the energy transfer in which the laser produces ions can be determined. In a laser plasma which consists of electrons and ions, the following must be considered in designing a system to provide an accurate energy distribution: (a) filtering out electrons before they reach the detector (b) filtering out ions of a specific energy below some retardation potential U_{ret}. The retarding potential analyzer is a device which fulfills these two conditions. A schematic of the analyzer is shown in Fig. 1.8(a). As electrons and positive ions propagate towards the detector, electrons and ions with an energy greater than qV, where V is the retarding plate bias, travel towards the collector. On the other hand, with energy less than qV are deflected away from the detector towards the floating plate. The bias plate voltage is swept from ground potential upwards, so the ion current will have a saturation when the bias plate voltage is near the ion energy. Above this energy, the ion current will decrease, as only higher energy ions can propagate towards the detector. A typical characterization curve utilizing a retarding potential analyzer of a laser plasma at 5 GW/cm laser intensity is shown in Fig. 1.8(b). At an ion retarding plate voltage of approximately 120 V, the ion current reaches its peak, which subsequently decreases the bias is further increased.

1.5 Organization of the work

In this work, a laser ion source is developed in characterizing electrons and ions produced in the plasma. Chapter 2 discusses the development of a laser ion source. Chapter 3 discusses the electron production mechanisms via the laser. Chapter 4 discusses the ion production using the laser ion source. Chapter 5 discusses optical emission characterization of confined plasmas.

Chapter 6 focuses on the film formation via pulsed laser deposition. Chapter 7 consists of the dissertation summary and future work.

1.6 Summary

Some fundamental principles and applications involved in laser ablation are discussed. Applications of laser ablation include mass spectrometry and elemental analysis. Factors affecting the laser plasma are listed, where laser intensity, background environment, and target material are the parameters which most significantly affect the produced plasma. Characterization methods such as time-of-flight spectroscopy are described.

References

[1] S. S. Mao, X. Mao, R. Greif, and R. E. Russo, Appl. Phys. Lett. **77**, 2464 (2000).

[2] M. Lenner, A. Kaplan, and R. E. Palmer, Appl. Phys. Lett. **90**, 153119 (2007).

[3] M. Hauer, D. J. Funk, T. Lippert, and A. Wokaun, Thin Solid Films **453-454**, 584-588 (2004).

[4] K. Shibagaki, T. Kawashima, K. Sasaki and K. Kadota, Jpn. J. Appl. Phys. **39** 4959-4963 (2000).

[5] C. Phipps, ed. *Laser Ablation and its Applications* (Springer Science+Business Media, New York, 2007) p. 375-549.

[6] R. E. Russo, X. Mao, J. J. Gonzalez, V. Zorba, and J. Yoo, Anal. Chem. **85**, 6162-6177 (2013).

[7] F. Pointurier, A. Pottin, and A. Hubert, Anal. Chem. **83**, 7841–7848 (2011).

[8] E. L. Papadopoulou, M. Barberoglou, V. Zorba, A. Manousaki, A. Pagkozidis, E. Stratakis, and C. Fotakis, J. Phys. Chem. C **113**, 2891–2895 (2009).

[9] A. Y. Vorobyev and C. Guo, Laser Photonics Rev., **7**, (3) 1–23 (2012).

[10] A. Gibbings, M. Vasile, J. Hopkins, D. Burns, I. Watson, Space Policy **28**, 149-153 (2012).

[11] C. Phipps, M. Birkan, W. Bohn, H. A. Eckel, H. Horisawa, T. Lippert, *et al*. Review: laser-ablation propulsion. J. of Prop. Power **26(4)** 710-22 (2010).

[12] M. Vasile and C. Maddock, Orbital Debris Removal with Solar Concentrators IAC 10eA6.4. 61st International Astronautical Congress, Prague, Czech Republic October 2010.

[13] C. Momma, B. N. Chichkov, S. Nolte, F. von Alvensleben, A. Tiinnermann, H. Welling, B. Wellegehausen, Opt. Comm. **129** 134-142 (1996).

[14] J. C. Miller, ed. *Laser Ablation Principles and Applications* (Springer-verlag, Berlin, 1994) p. 19-26.

[15] T. Takahashi, S. Tani, R. Kuroda, and Y. Kobayashi, Appl. Phys. A **126** 582 (2020).

[16] S. Amoruso, R. Bruzzese, N. Spinelli, and R. Velotta, J. Phys. B: At. Mol. Opt. Phys. **32** R131–R172 (1999).

[17] K. Zehra, S. Bashir, S.A. Hassan, Q.S. Ahmed, M. Akram, and A. Hayat, Laser and Particle Beams, **35**, 492–504 (2017).

[18] S. Bashir, N. Farid, K. Mahmood, M. Shahid Rafique, Appl. Phys. A **107** 203–212 (2012).

[19] S. S. Harilal, N. Farid, J. R. Freeman, P. K. Diwakar, N. L. LaHaye, and A. Hassanein, Appl. Phys. A **117** 319–326 (2014).

[20] D. Marla, U. V. Bhandarkar, and S. S. Joshi, Manuf. Lett. **2** 13-16 (2014).

[21] S. Sinha, J. Laser Appl., **30**, 1, (2018).

[22] M. M. Wolff AND W. E. Stephens, Rev. Sci. Inst. **24** (8) 616-617 (1953).

[23] R. J. Cotter, ed. *Time-of-Flight Mass Spectrometry*, (American Chemical Society, Washington DC) 1994, p. 16.

[24] S. T. Lai and C. Miller, AIP Adv. **10**, 095324 (2020).

Chapter 2

Cavity laser ion source

2.1 Introduction

2.1.1 Plasma expansion

Following plasma production, plume expansion indicates the constituent electron, ion, and neutral motions in the plasma. Since these two processes are consecutive, plasma expansion also depends on the laser parameters, background environment, and target material. The understanding of plasma expansion leads to that of the laser-target interaction, as well as the interactions between the produced electrons and ions. Laser plasma expansion has been investigated numerically, as well as analytically. In a paper of Kelly and Dreyfus, the ion velocity distribution from the expansion of a pulsed heat (or laser) source on the target in vacuum is described in two cases: collisionless expansion and Knudsen layer formation [1]. In collisionless expansion, the motion of the ions are assumed to be moving only in a single direction, *i.e.* ions propagate only in the direction away from the target surface. This is interpreted as a half-range Maxwellian, with only positive values. In the case of higher vapor density plasma, collisions are present and the entire Maxwellian distribution becomes an entirely non-equilibrium process. In this condition, a *Knudsen layer* is formed. The Knudsen layer is described as the region within a few mean free paths from the target surface in which a change from a collisionless to a non-equilibrium velocity distribution occurs [1]. For a velocity v_x along the x axis, the velocity distributions are described by [1, 2]:

$$f(v_x) \propto e^{-\frac{mv_x^2}{2k_B T_s}}, v_x \geq 0 \tag{2.1}$$

$$f(v_x) \propto e^{-\frac{m(v_x - u_K)^2}{2k_B T_K}}, -\infty < v_x < 0, \tag{2.2}$$

where u_K is the center-of-mass velocity of the Knudsen layer, m is the particle mass, k is the Boltzmann constant, and T_s, T_K are the target surface and Knudsen layer temperature respectively. As the number density of the plume further increases, collisions further increase, and the expanding plume is assumed to follow an adiabatic expansion, along with the formation of the near-surface Knudsen layer [3]. Figure 2.1 shows a schematic of the target surface with the formed Knudsen layer. The Knudsen layer is

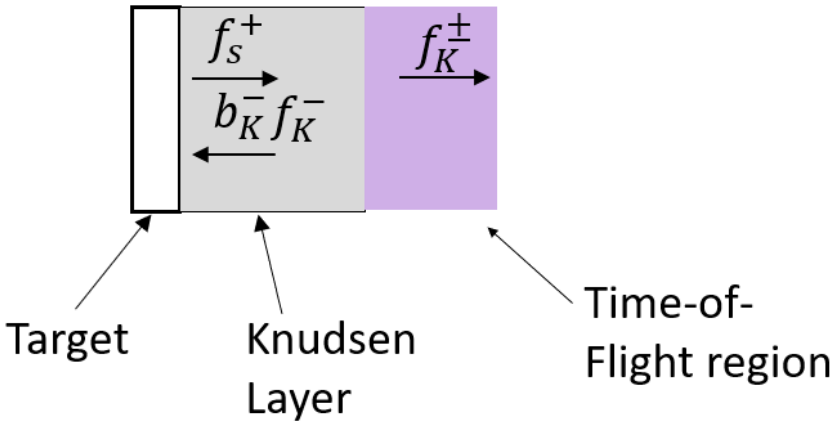

FIGURE 2.1: Schematic of the expansion of a collision-free vaporized plume, as adopted from [1], where f_s^+, f_s^- represent the distribution functions of the particles flowing out, or recondensing towards the target surface, respectively, b_K is a proportionality constant

significantly thicker than the time-of-flight region. Since the time-of-flight region comes after the Knudsen layer, the former, then, represents the non-equilibrium expansion of the plasma plume.

These fundamental mechanisms enable the understanding of the particle expansion of the laser plasmas. However, all of these processes occur in a single laser shot, *i.e.* the target is not significantly modified due to the damage induced by the laser. In these processes, collision interactions occur within the plasma plume itself. In the following subsection, the rationale of the developed laser ion source is described.

2.1.2 Rationale of the ion source

As described in Chapter 1, the factors affecting the laser produced plasma involve target and background environment. The collision frequency increases with the background pressure, while differing the target material would modify the entire plume produced. In this work, a laser ablation ion source is designed to investigate the effect of the target in confining the plasma itself, thereby contributing to collisions.

When the laser is incident on the target, a small crater is formed on its surface. Repeated ablation of the target at the same spot drills a cavity from which the laser plasma is initiated. The expanding plasma is inhibited by the cavity walls. Therefore, the target contributes to the change in the background environment of the plasma. Figure 2.2 shows the schematic of target cavity formation leading to the plasma confinement.

Repeated drilling can be performed by an incident laser perpendicular to the target surface. However, a disadvantage is the inability in characterizing the plasma propagating along this direction. Thus the developed ion source consists of a laser at an angular incidence, so that when the target is axially rotated, a charge collector can be installed perpendicular to the target

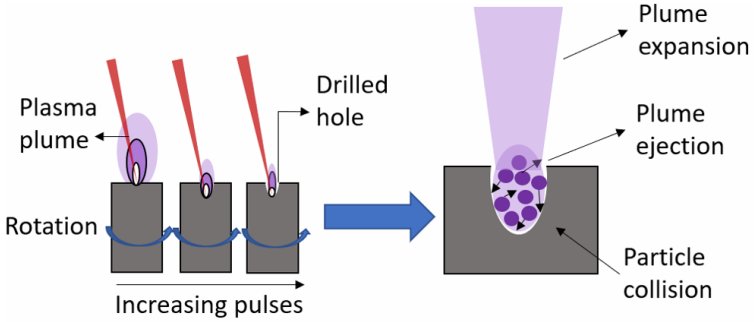

FIGURE 2.2: Schematic of target cavity formation via repeated laser ablation

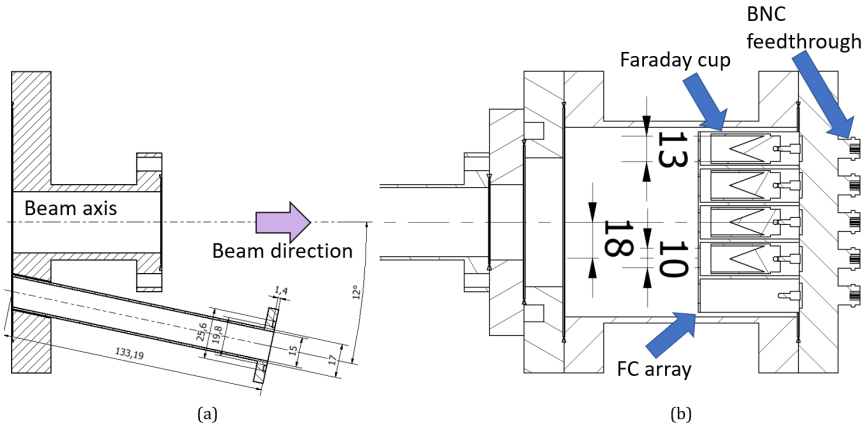

FIGURE 2.3: (a) Schematic of the laser flange (b) schematic of the Faraday cup array

surface. When the laser is incident at a large angle from the target axis, the cavity formed from the cavity may form an incorrect hole, resulting to a conical shape on the cavity. Therefore, the laser incident at small angles is necessary to form the proper cavity. The developed laser flange is shown in Fig. 2.3a. The angle of 12° is due to the limitation of the ICF 152 flange in creating the port allowing for the beam propagation to the ICF 70 port. The propagating plume is directed towards a Faraday cup array, whose schematic is shown in Fig. 2.3b. The Faraday cup array consists of five conical stainless steel cups with a diameter of 13 mm whose axes are placed 18 mm apart. The Faraday cup array is enclosed inside a grounded stainless steel shield with an aperture of 10 mm to prevent interference from the other cup electric induction. The Faraday cup array is labelled as left, center, and right, where the positions correspond to -18 mm, 0 mm and 18 mm from the axis, respectively, and the negative sign indicates the position away from the laser port direction.

2.2 Experimental schematic

2.2.1 Time-of-flight spectrometer

The schematic for the cavity laser ion source is shown in Fig. 2.4. An Nd:YAG laser at 1064 nm is incident 12° from the target axis. The target is fastened to a stainless steel target holder which is attached to an ICF 34 vacuum rotational feedthrough. The laser is aligned towards the center of a cylindrical target by firing a burst shot at 5 GW/cm^2 laser intensity to a reticule attached to the surface of a graphite target. The feedthrough is manually rotated by firing single burst laser shots to ensure the same spot is ablated on the target. After alignment, a DC motor is attached to the feedthrough and is rotated at a rate of 30 rev/min. The propagating plume is directed towards the Faraday cup array. Each of the array terminals is connected to a 500 MHz oscilloscope with a 50 Ω BNC termination resistor. Experiments are performed inside an ICF-class stainless steel vacuum chamber, under 10^{-5} Pa vacuum pressure. In adjusting the laser intensity, the amplifier delay is adjusted via the GUI. The oscillator, Q-switch delays are kept constant at 150 and 140 μs for laser stability. Figure 2.4c shows the laser intensity dependence on the amplifier delay. This graph shows an exponential trend fitted at the equation $I(x) = y_0 + A\exp(-(x - x_0)/\tau)$. where increasing the delay decreases the laser intensity.

2.2.2 Retarding potential analyzer

The schematic of the retarding potential analyzer is shown in Fig. 2.5a. A floating plate is attached 2 mm in front of the 4 mm aperture bias plate. The bias plate is attached to the grounded Faraday cup shield. The potential distribution of the analyzer without the permanent magnets is simulated in AmaZe software, and is shown in Fig. 2.5b. The potential at the center of the bias plate V_{center} is obtained from the potential distribution. For varying bias plate aperture diameters and plate thickness at $V_{bias} = 1kV$, the ratio V_{center}/V_{bias} is shown in Fig. 2.5c. The potential decrease is more significant by increasing the hole diameter than decreasing the plate thickness. A hole diameter that is too small may decrease the signal intensity. Therefore a 4 mm diameter and a 4 mm thickness are chosen for the plate dimensions.

2.2.3 High speed imaging

Figure 2.6 shows the schematic of high speed measurement of the expanding plasma plume. The high speed camera is positioned perpendicular to the target and the plume is imaged through a glass viewport. The camera has a frame rate of 30000 fps, and the image capture is triggered by the initial glow of the plasma plume, after the laser is incident on the center of a graphite target. The emitted glow is focused towards the CCD detector of the camera.

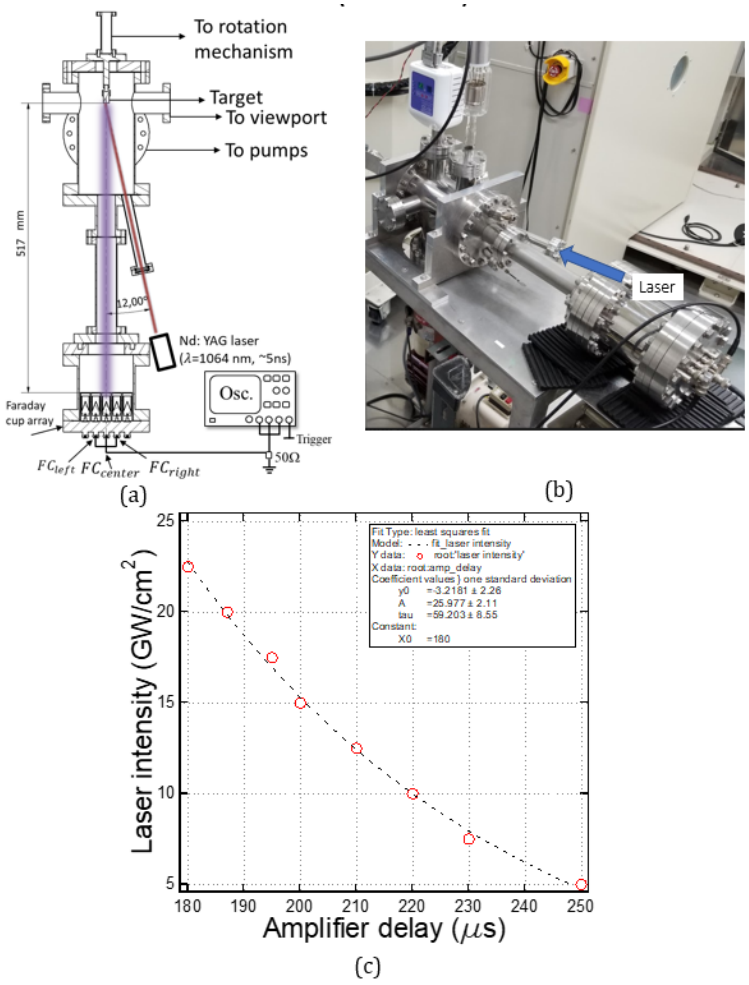

FIGURE 2.4: (a) Schematic of the time-of-flight spectrometer (b) Image of the time-of-flight spectrometer assembly (c) laser intensity versus amplifier delay

2.3 Results

2.3.1 Ion time-of-flight signals

Figure 2.7 shows the ion signals collected by the Faraday cup (FC) using the schematic in Fig. 2.4, where the Faraday cup array has no magnets installed. In all signals, a negative peak at around 6 μs followed by a positive signal peaking at 8 μs are observed. Following this signal, a negative signal is observed, persisting until 40 μs. Ion signals detected by the left, center, and right FCs in Fig. 2.7a shows the ion signal distribution of the beam, where the highest signal is detected at the center FC, followed by the left FC. Figure 2.7b shows the ion signals at the center FC for varying laser intensities. For increasing laser intensities, the initial negative peak, positive peak, and the broad negative distribution are shifted towards earlier times, corresponding to 0.06, 0.6, and 1.01 μs shift for the electrons relative to the 5 GW/cm^2, respectively. Figure 2.8 shows the ion signals after multiple pulses at 5 GW/cm^2 laser power density. Decrease in the electron current at

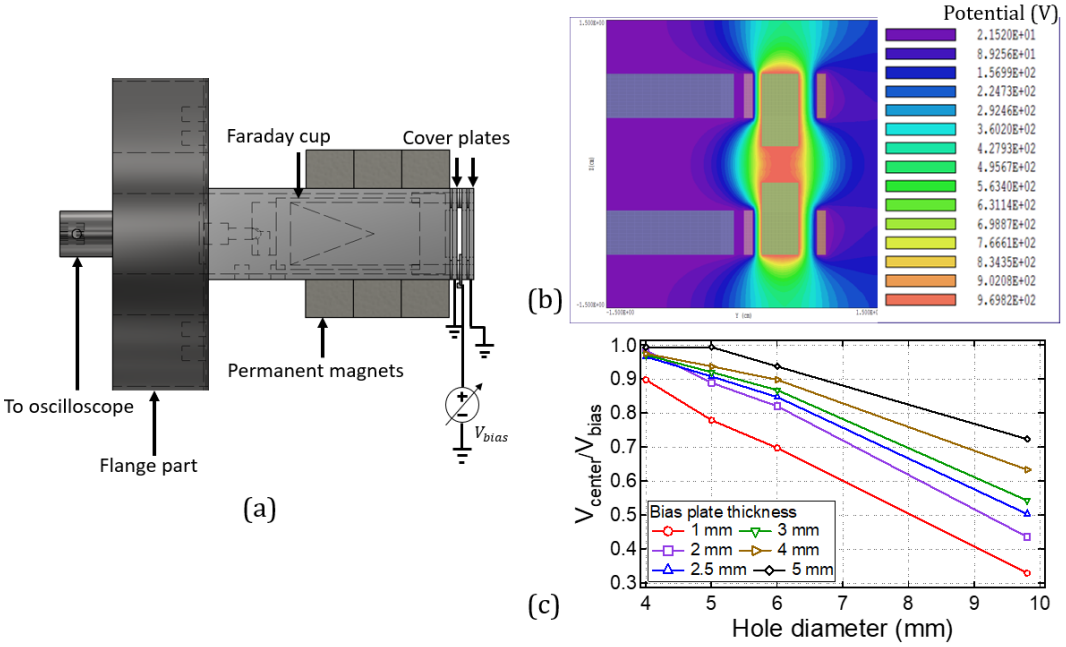

FIGURE 2.5: (a) Retarding potential analyzer (b) Potential distribution of the analyzer, $V_{bias} = 1kV$ (c) Normalized potential ratio V_{center}/V_{bias} for varying analyzer hole diameters and plate thicknesses

3 μs as well as decrease in ion peak current at 5 μs are observed. From after 1000 pulses, the broad distribution from 10 to 30 μs changed from a positive towards a negative signal.

The graphs in Fig. 2.7 and Fig. 2.8 show the time of flight signals representing both electrons and ions. However, in order to obtain the ion energy distribution, the electrons must be suppressed. One method for electron suppression is magnetic field induction near the detection region, such that the magnetic field is strong enough to deflect electrons. The parameter in measuring electron deflection is the Larmor radius traversed by a particle under the influence of a magnetic field, defined as:

$$r_g = \frac{mv_\perp}{qB}, \tag{2.3}$$

where $m, v_\perp, q, B$ are the mass, ion velocity, electronic charge, and magnetic flux density, respectively. Given a TOF distance of 517 mm, flight time 6 μs, and 250 G magnetic flux density, r_g results to approximately 2 nm. This means that the electrons follow a circular path of 2 nm radius along the magnetic field lines. The radius is also approximately 6 orders of magnitude smaller than the Faraday cup dimensions, therefore the electrons are sufficiently suppressed at this flux density. Another disadvantage of the absence of electron suppression is that the negative signal may overlap with the positive ion signal, which results to lowering of the ion current. Figure 2.9a shows the ion signals for varying laser intensities with the installation of permanent magnets near the Faraday cup, as in Fig. 2.5a. Sharper ion peaks were observed for all plots, and negative peaks before

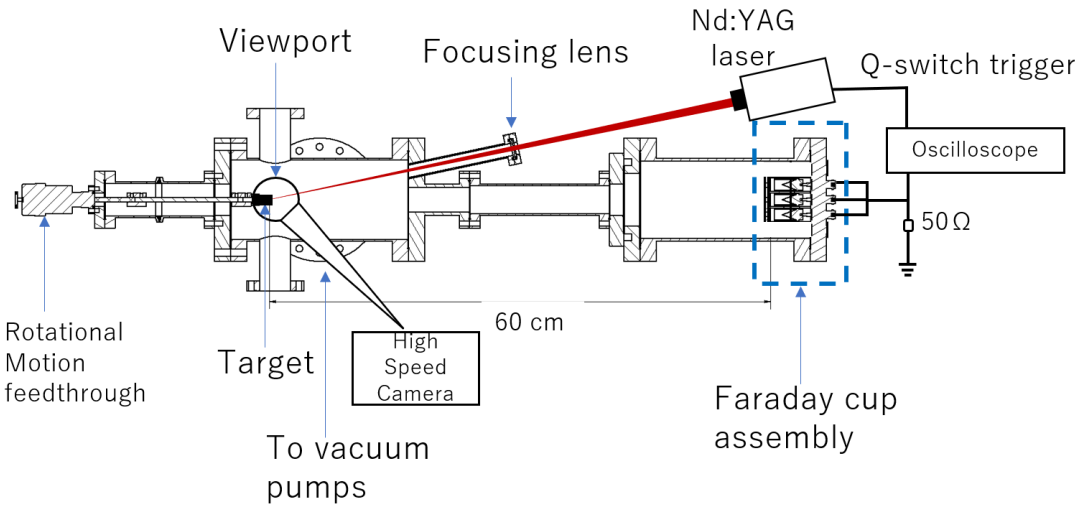

FIGURE 2.6: High speed measurement schematic

the ion peaks were not detected, indicative of the electron suppression. The negative broad distribution was also not detected, which indicates that this distribution represents electrons now deflected by the field. Increasing the laser intensity also increases the ion signal intensity and shifts towards earlier times. Increasing the number of pulses shifts the current signal towards later times, as shown in the 0.9 μs shift after 4000 pulses.

2.3.2 Retarding potential analysis

Figure 2.10 shows the ion signals for varying retarding potential analyzer bias for a fresh target and after 2000 pulses ablation. For the fresh target, the peak ion current increases to 2 mA and subsequently decreased as the retarding potential bias is further increased. After 2000 pulses, the similar behavior of initial current increase followed by decrease is observed. After around 400 V, almost no ion signal was detected.

From the peak ion current, the ion energy distribution can be determined by taking the derivative of the ion peak current versus the retarding potential voltage. Figure 2.11 shows the peak current (fits represented by the solid lines) of the ion signals, along with the ion energy distribution functions for varying number of pulses. Overall, the ion peak current decreases as the retarding potential bias increases. Increasing the number of pulses decreases the ion peak energy. Taking the energy differences between the distributions, the energy difference between the one after 500 pulses and the fresh target is larger (40 eV) than the one after 20000 pulses and 3000 pulses (10 eV).

2.3.3 High speed images

Figure 2.12 shows the high speed images after a single shot at the graphite target at 5 GW/cm^2 laser intensity. An initial glow where the angle is measured approximately 80 degrees from the target axis. This angle decreases with time. Following the initial burst, the plume evaporates in

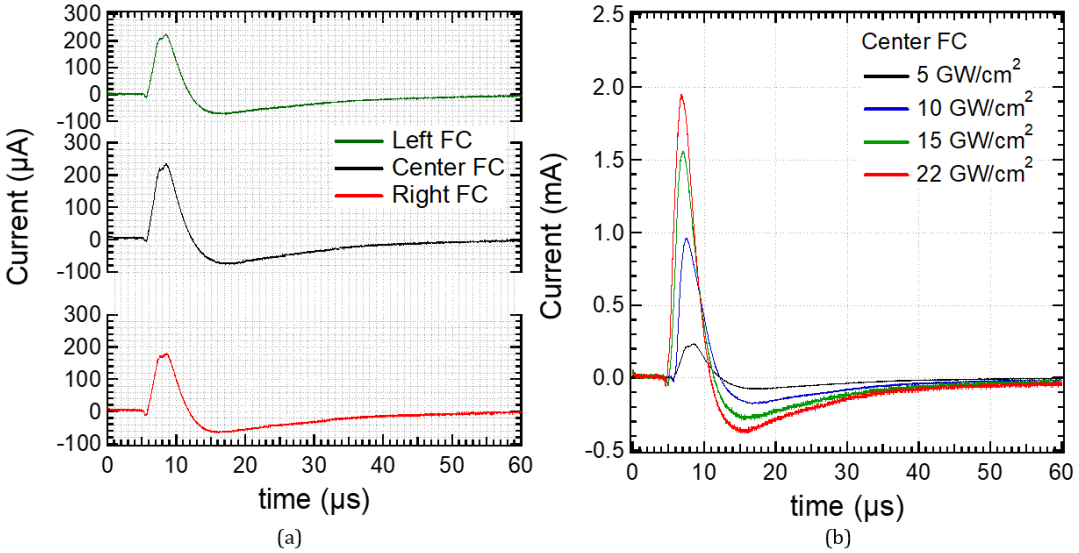

FIGURE 2.7: (a) Faraday cup ion signals under 5 GW/cm^2 laser intensity ablation without installation of RPA (b) Ion signals at center Faraday cup for varying laser intensities

a spray-like behaviour, where the glow sustains until approximately 340 μs. From 99 μs, vaporized particles were observed to propagate away from the target. The speed of these particles are roughly estimated using ImageJ software by choosing two frames from the sequence and forming ten lines from the same spot towards a particle and measuring the velocity given the frame interval of 33 μs. The estimated velocity of the ablated particles is then around 110 m/s. Figure 2.14 shows the high speed images at varying laser intensities. Increasing the laser intensity shows a larger area of bright regions corresponding to increased amount of vaporized material. Figure 2.15 shows the high speed images of the target for varying number of pulses at 5 GW/cm^2 drilling laser pulse intensity.

2.3.4 Target cavity condition

Figure 2.16 shows target micrographs for increasing number of pulses. As the number of pulses is increased, a rim is formed on the periphery of the center region. The incident laser distribution then shows a Gaussian beam shape, since the beam significantly decreases with distance from the center.

2.4 Discussion

The time-of-flight spectra shows the initial arrival of electrons followed by ions towards the detector. When the plasma is formed, fast electrons are ejected from the target surface, which creates a charge separation with the ions. This charge separation accelerates the ions perpendicular to the target surface. Figure 2.7a shows that the center Faraday cup consists of the highest signal, which shows the preferential motion of the beam along the target axis.

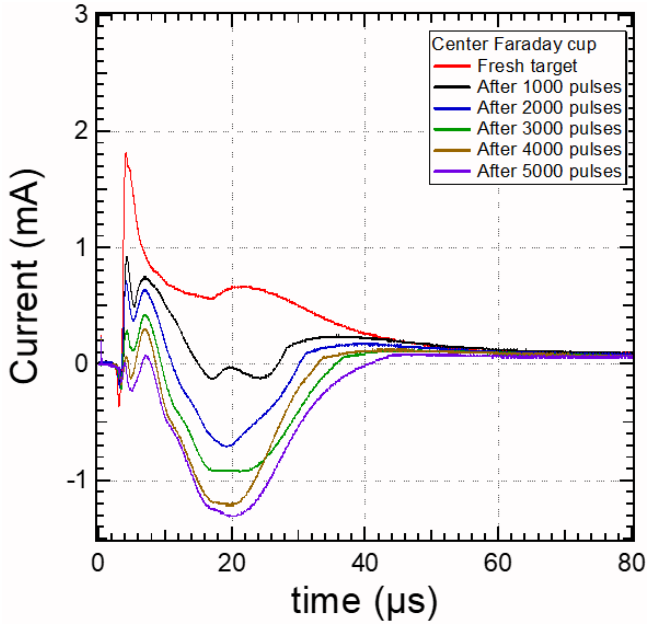

FIGURE 2.8: Ion signals for increasing number of pulses

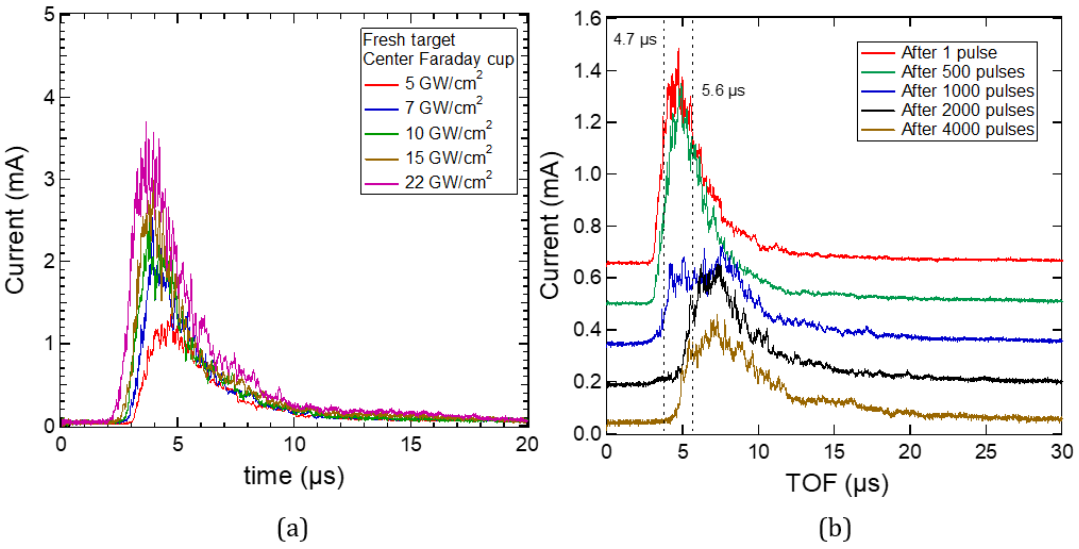

(a) (b)

FIGURE 2.9: Ion current with the installation of permanent magnets near the Faraday cups (a) Ion signals for increasing laser intensities (b) Ion signals for increasing number of pulses

However, the difference between the ion currents fall under 50 μs, which shows that the ion beam has a diameter larger than 38 mm and occupies the entire collector region. The results of Fig. 2.7b shows the increase of ion current, as well as the broad electron peak with the increase of laser intensity. This indicates the increase in ions and electron produced due to the increase in the laser energy converted to higher target ablation. From the signals in Figure 2.8, the decrease of ion signal at 5 μs represents the decrease of the ions formed as the cavity is increased, which is due to the ablation rate decrease. On the other hand, the increase in broad negative signal after the positive signal represents the electrons produced from collisions in the cavity, since

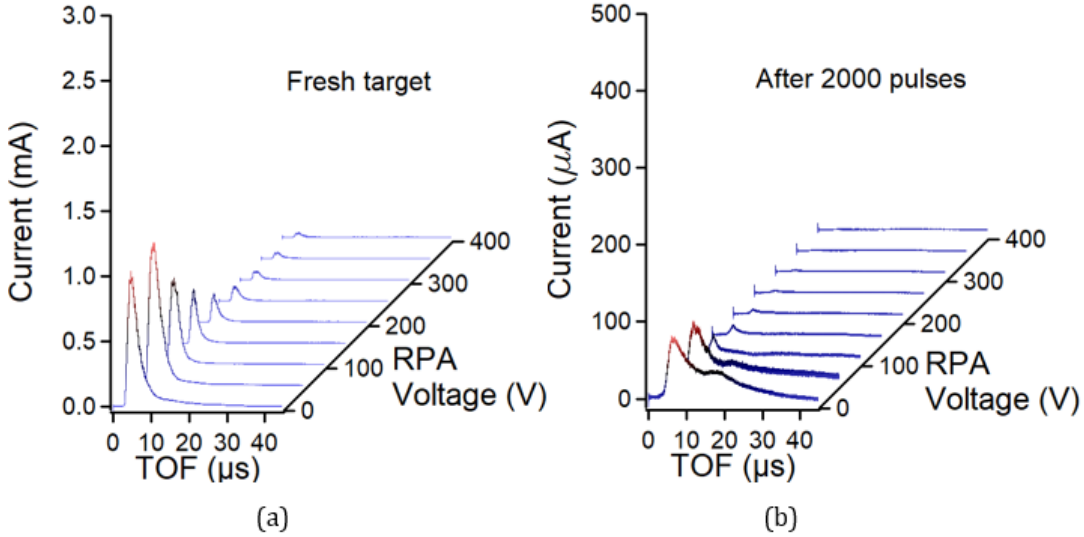

FIGURE 2.10: Ion signals of the center Faraday cup for increasing retarding potential analyzer bias voltage at 5 GW/cm^2 laser intensity for (a) fresh target (b) after 2000 pulses ablation

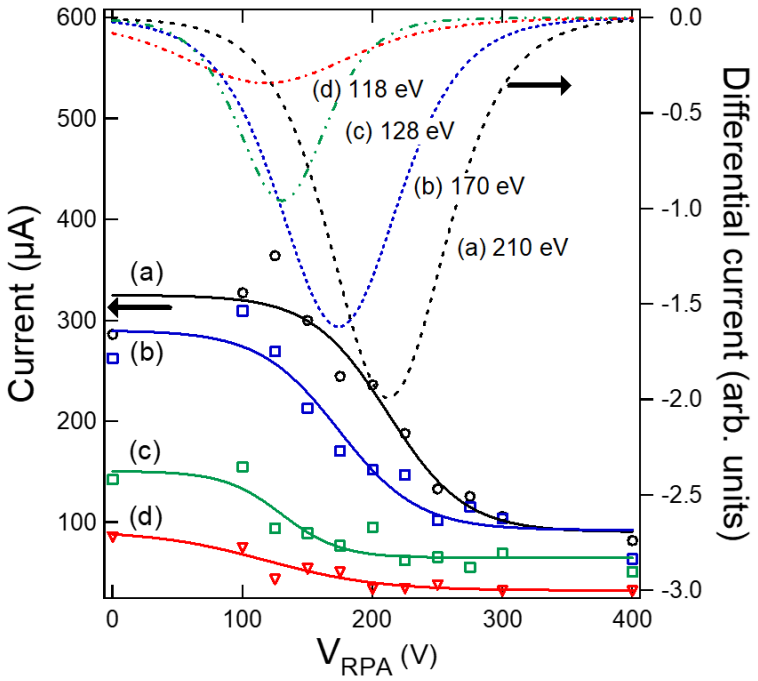

FIGURE 2.11: Peak ion current and ion energy distribution functions at 3 GW/cm^2 laser intensity for varying number of pulses; (a) one pulse (b) 500 pulses (c) 3000 pulses (d) 20000 pulses

the negative signals were deflected once permanent magnets are installed in front of the detector. Peak shifts of the positive ion signals toward later times shows the velocity reduction of the ions. The velocity reduction originates from the energy losses due to inelastic collisions with the cavity. As the cavity depth further increases, collision probability increases, therefore increasing

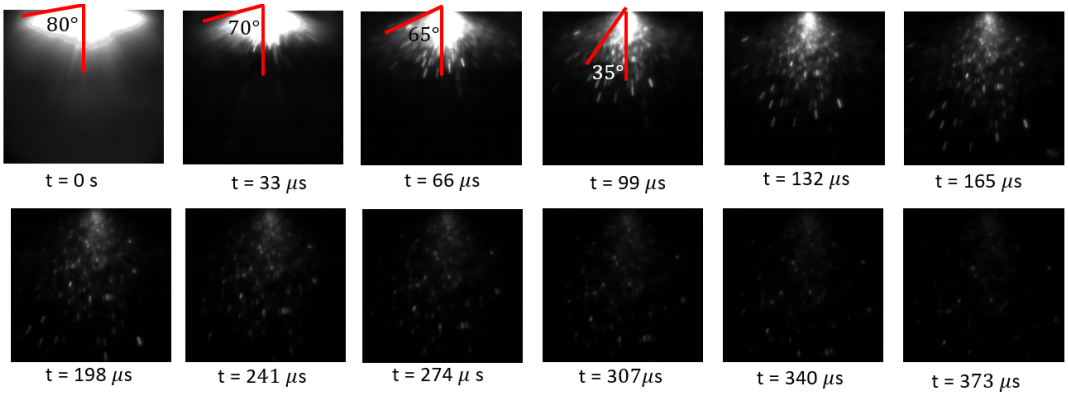

FIGURE 2.12: High speed images after a single pulse at 5 GW/cm^2 laser intensity

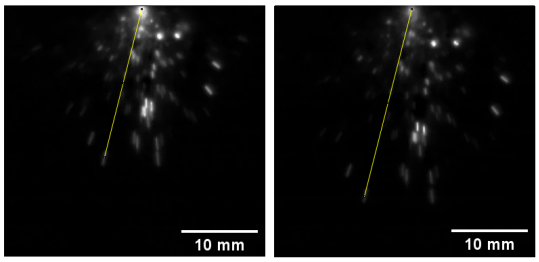

FIGURE 2.13: High speed images of the ablated target at t = 132 μs (left) and t = 165 μs

the energy loss. This energy loss can also be observed from the retarding potential analysis results. Fig. 2.11 show that the positive ion energy falls around 200 V, which decreases with increasing number of pulses. This energy decrease indicates that the ions and electrons from the constricted plasma suffer energy losses when they collide with the cavity walls.

The time of flight signals detected here consists of a broad distribution of energies and masses. In the next sections, design modifications are performed with the aim of resolving the ion masses.

2.5 Summary

A laser ion source is developed in order to investigate the ions of a laser produced plasma from a graphite target. A time-of-flight spectrometer is developed in order to detect ions produced from the plasma. Ion signal intensities increase with the input laser intensities. Increasing the number of pulses decreases the ion signals and shifting them towards later times, indicative of the energy losses occurring within the cavity.

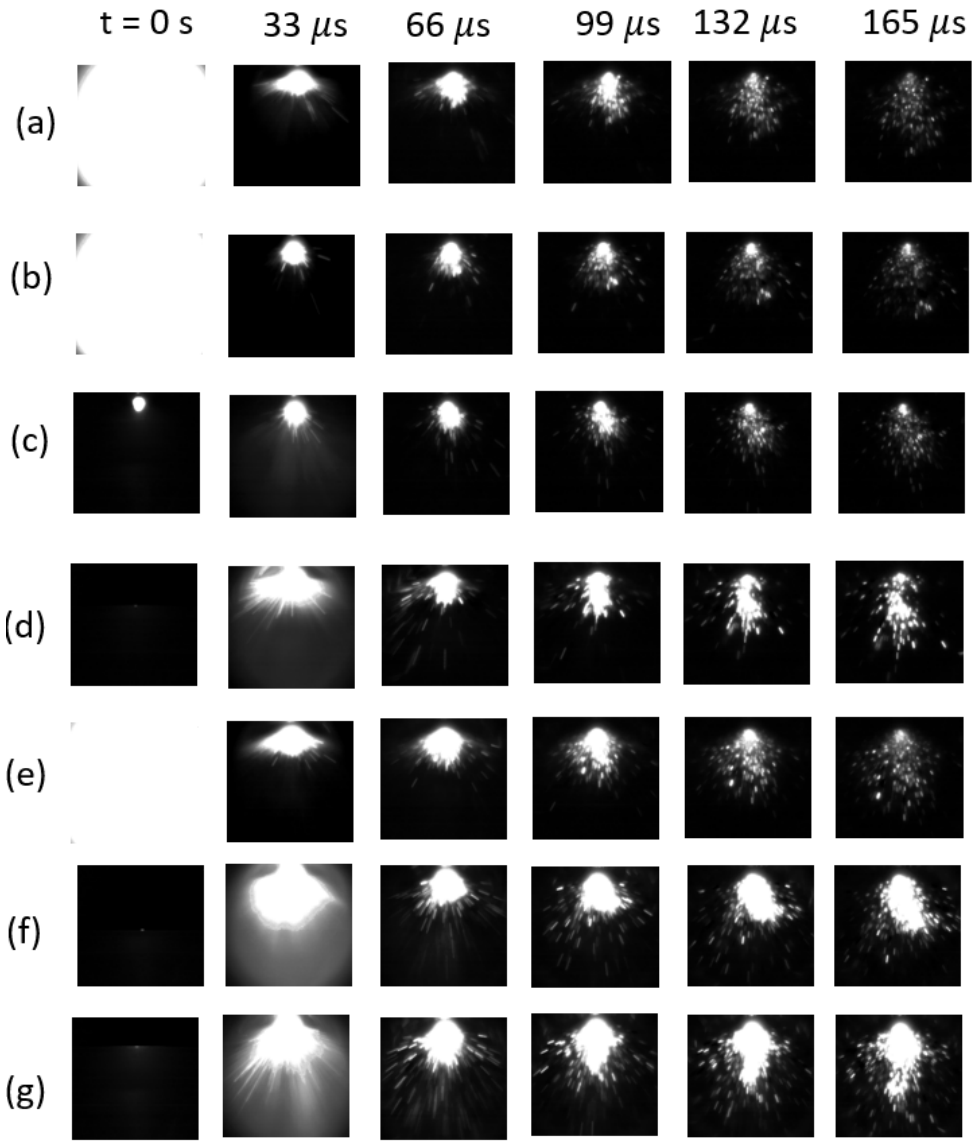

FIGURE 2.14: Single shot high speed images of the fresh target for (a) 5 (b) 7.5 (c) 10 (d) 12.5 (e) 15 (f) 17.5 (g) 22 GW/cm^2 laser intensities

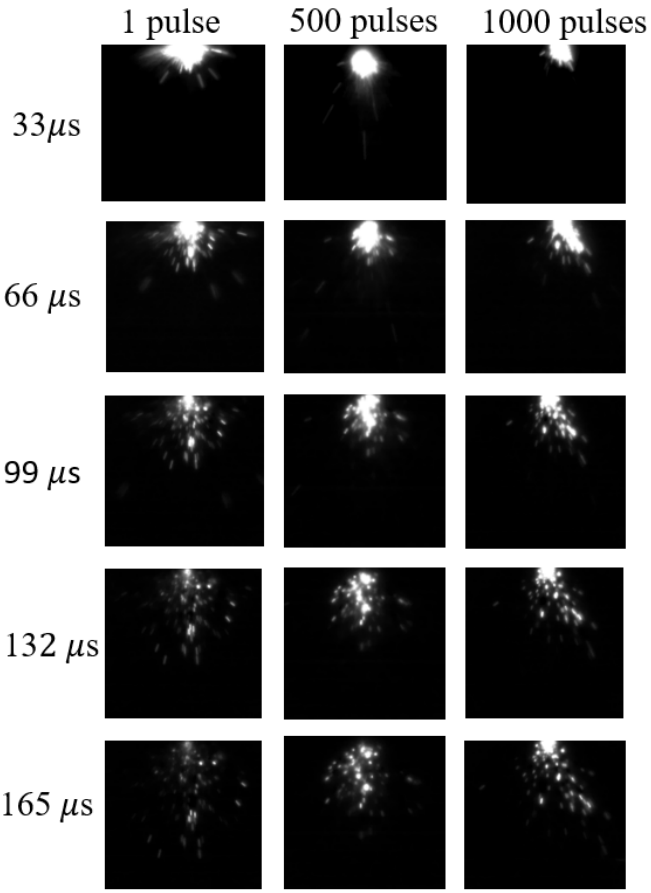

FIGURE 2.15: High speed images of a graphite target at 5 GW/cm^2 laser intensity for increasing laser pulses

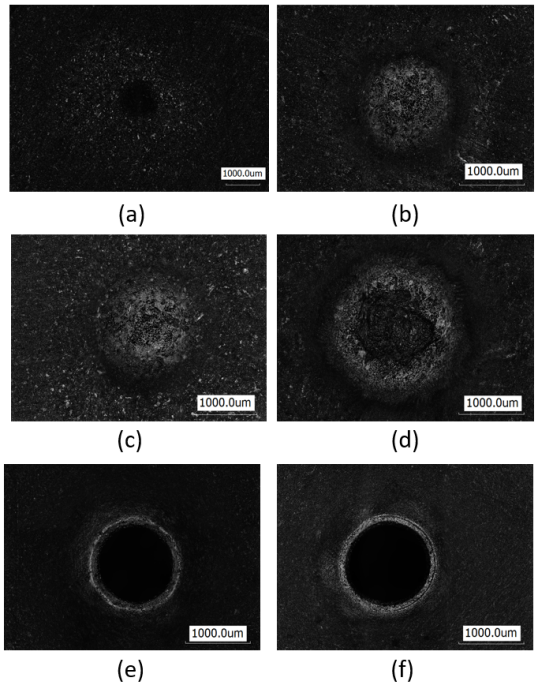

FIGURE 2.16: Target cavity micrographs after (a) one pulse (b) 100 pulses (c) 200 pulses (d) 500 pulses (e) 1000 pulses (f) 10000 pulses

References

[1] R. Kelly and R. W. Dreyfus: Surf. Sci. **198** 263-276 (1988).

[2] S.I. Anisimov, Soviet Phys. JETP **27** 182 (1968).

[3] Q. Zhu, J. Yamada, N. Kishi, T. Hosokai, M. Watanabe, A. Okino, K. Horioka, and E. Hotta, Jpn. J. Appl. Phys. **49** 056201 (2010).

Chapter 3

Electron production in a laser produced plasma

3.1 Introduction

In the process of laser ablation, the primary mechanism involves the interaction between the laser and target leading to electron production and target ionization. The wavelength of laser light, its intensity, pulse duration, and the target material all influence the probability at which electrons and ions are produced via the laser. The mechanisms involving electron and ion production is made more complex by the production of plasma with the ejection of ablated material. Two of the main mechanisms involved in the ionization of solids via the laser are multiphoton ionization, or MPI, and electron impact ionization, or EI. In this chapter, the mechanisms of MPI as well as EI are briefly discussed. Experiments involving charge collection near the target surface are also presented.

Two parameters typically obtained in modelling laser ablation plasmas is the target surface temperature, and electron density. For example, obtaining the target surface temperature involves solving the heat equation. The identification of target surface temperature results to the understanding of mainly the ejected plume and its interaction with the substrate for thin film deposition applications [4]. In the work of Sinha, as well as Bulgakova and Bulgakov, a thermal model based simulation is performed to caclulate the surface temperature, wherein, considering propagation along the x direction, the laser is expressed as a source term $S(x,t)$, and the intensity $I_S(x,t)$ on the optically thick plasma are expressed as [5, 6]:

$$S(x,t) = I_o exp(-x^2) exp(-t) I_S(x,t) = S(x,t)\exp[-\Lambda(x,t)], \tag{3.1}$$

where Λ is the optical thickness of the ablation plume. The thermal based simulation solely considers the thermal evolution from the radiative transfer from the laser, as well as conductive heat transfer within the target. Typical applications of obtaining surface temperature is to understand different ablation rates and material removal of a target, as well as plume expansion and shielding [7].

On the other hand, the electron density is obtained by solving a rate equation in a simplified form, assuming an ionization of a single molecular

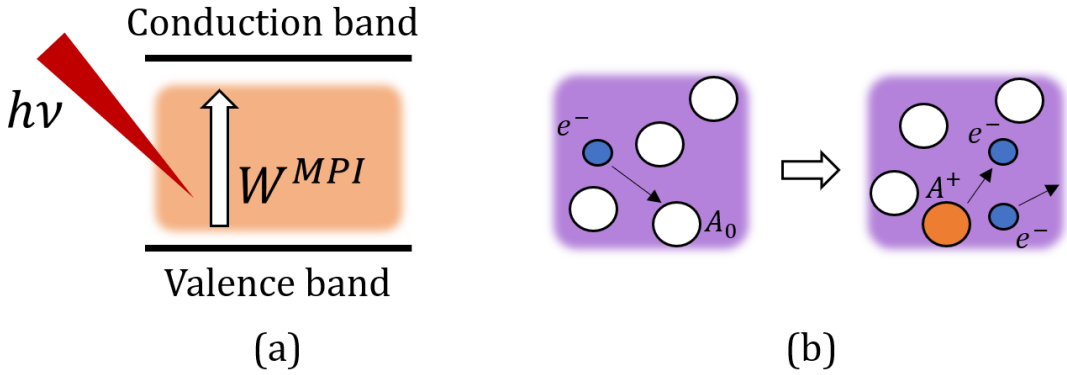

FIGURE 3.1: Schematic of (a) multiphoton ionization and (b) electron impact ionization processes

species of initial energy ϵ_o and arbitrary energy ϵ [12]:

$$\frac{d\rho(\epsilon)}{dt} = \nu_{EI}\rho(\epsilon) + \delta(\epsilon - \epsilon_o)\int_0^\infty d\epsilon'\nu(\epsilon')\rho(\epsilon') + \delta(\epsilon)W^{MPI}(E)P_m \tag{3.2}$$

where $\rho(\epsilon)$ represents the energy-dependent electron density, ν_{EI} is the electron impact ionization rate, W_{MPI} is the multiphoton ionization rate, both of which will be described in the following subsections.

3.1.1 Multiphoton ionization (MPI)

Multiphoton ionization, or MPI, is the excitation of a neutral atom towards its ionized state when a strong electric field is applied. In this condition, the photons occupy the same state in the atom in the valence band and oscillates in the direction of the electric field [8]. In an intense electric field, such as a high power laser, given a sufficient intensity, the produced electron obtains an oscillation energy [9]

$$E_{osc} = \frac{e^2E^2}{4m\omega^2}, \tag{3.3}$$

where E, m, ω are the electric field intensity, mass, and frequency of light respectively. The laser incident on the electron consists of energy transfer, and if the laser energy exceeds the ionization energy E_i of the atom, the energy becomes $E_i + E_{osc}$ [9]. In the case of long laser pulses, the electron is still exposed to the laser energy which accelerates the electron. As E_{osc} is maximum at the focal point of the laser pulse, when the electron leaves the target, the energy transferred to the electron is lowered.

In the multiphoton ionization of multielectron atoms, the intense laser pulse subjects the removal of several electrons in the outer shell of the atom. The simultaneous removal of electrons results to the production of multiply charged atoms, as shown in Fig. 3.1.

The mechanism of MPI is suggested by Keldysh, where the light is treated as an oscillating electromagnetic wave that induces a simultaneous transition of the electron from a ground state towards a free state [10]. In the laser-target interaction, when the laser photon frequency is less than the target

work function, it does not necessarily mean that the ionization probability is zero. The MPI probability is expressed as [11]

$$
\begin{aligned}
W^{MPI} &= \omega \left(\frac{B}{E_\omega}\right) \left(\frac{\gamma}{\sqrt{(1+\gamma^2)}}\right)^{5/2} S\left(\gamma, \frac{B+\Phi_p}{E_\omega}\right) \exp\left[-\frac{2(B+\Phi_p)}{E_\omega}\right] \\
&\quad \exp\left(-\frac{2(B+\Phi_p)}{E_\omega}\right) \left[\sinh^{-1}\gamma - \gamma\frac{\sqrt{1+\gamma^2}}{1+2\gamma^2}\right], \\
S(\gamma, x) &= \sum_{n=0}^{\infty} \exp\left[-2[\langle x+1\rangle - x + n]\right] \\
&\quad \times \left(\sinh^{-1}\gamma - \frac{\gamma}{\sqrt{1+\gamma^2}}\right) \Phi\left(\left[\frac{2\gamma}{\sqrt{1+\gamma^2}}(\langle x+1\rangle - x + n)\right]^{1/2}\right), \\
\Phi(z) &= \int_0^z e^{y^2-z^2}\, dy
\end{aligned}
\tag{3.4}
$$

where $E_\omega = \hbar\omega$ is the photon energy, γ is the Keldysh parameter, given as

$$
\gamma = \omega\frac{\sqrt{2mB}}{eE_0}\left(\sqrt{\frac{B}{2\Phi_p}}\right) \tag{3.5}
$$

where B is the ionization potential energy, E_0 is the laser electric field intensity, $\Phi_p = e^2E^2/4m\omega^2$ is the gravitational potential. In MPI, the Keldysh parameter γ is » 1. The angle brackets take the integer values. The integral $\Phi(z)$ is the Dawson integral and can be solved numeraically. In the above equations, it can be observed that the ionization probability W^{MP} is also proportional to the laser intensity. Figure 3.2 shows the dependence of the Keldysh parameter and MPI ionization probability W^{MPI} on the laser intensity of argon and carbon atoms for varying laser wavelengths. Both argon and carbon exhibit the same behavior of the Keldysh parameter at the same wavelength. The Keldysh parameter is higher for lower wavelengths. Ionization probability via MPI is also high at lower wavelengths. From around 10^{14} W/cm^2 laser intensity, the probability at 800 nm wavelength exceeds that of the lower wavelength in carbon. However, in all wavelengths, the Keldysh parameter as well as the ionization probability decreases when the laser intensity is further decreased below 10^{17} GW/cm^2 laser intensity.

The increase of ionization probability for increased intensity indicates the increased available photons for ionizing the multielectron atoms. Similarly, the increased MPI probability for decreased wavelength indicates the increased photon energy to exceed the energy band of the neutral state. Further increasing the intensity indicates that the energy is too high for multiphoton ionization.

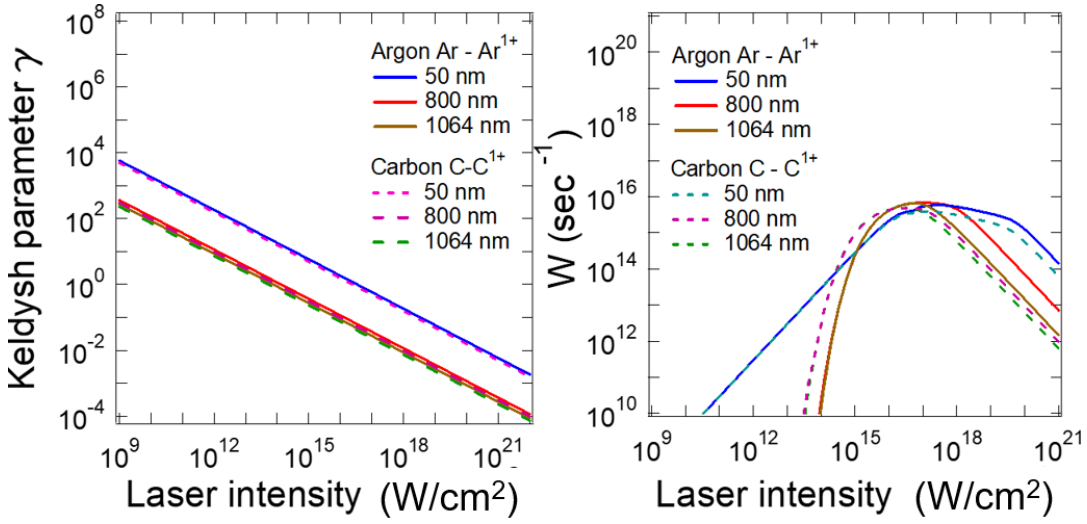

FIGURE 3.2: (Left) Keldysh parameter and (Right) MPI probability versus laser intensity for the ionization of argon

3.1.2 Electron impact ionization (EI)

electron impact ionization, or EI, is devised by Bleakney and Nier [1, 2]. The process involves the ionization of neutral atoms when an electron with kinetic energy exceeding the ionization energy of a neutral atom, which expels an electron from the atom. The electron corresponds to a wavelength of $\lambda = h/mv$, where high energy electrons that are near the transition state of the atom would ionize the atom. The process of expulsion does not involve an 'impact' of molecules, therefore the term electron impact ionization is sufficient [3]. In electron impact ionization, the mechanism involved for a neutral particle M is

$$M + e^- \rightarrow M^+ + 2e^- \tag{3.6}$$

In laser ablation plasmas, a large number of electrons are produced in the onset of the laser pulse, followed by heavier ions. In EI, this large source of electrons is necessary to initiate collisions with neutrals to form ions.

The processes of MPI and EI are typically described in a type of rate equation model, where each term is represented by its own probability of occurrence. However, this is assuming that the electron energy distribution is Maxwellian. In other words, the model assumes plasma thermal equilibrium with a velocity $v = \sqrt{kT/m}$. An expression utilized for EI is expressed as [12]

$$\nu_{EI}(\epsilon) = P_{EI}\sigma_{EI}(\epsilon)v(\epsilon), \tag{3.7}$$

where ϵ is the electron energy, P_{EI} is the neutral molecule population, σ_{EI} is the collision cross-section, $v(\epsilon)$ is the thermal velocity of the electrons.

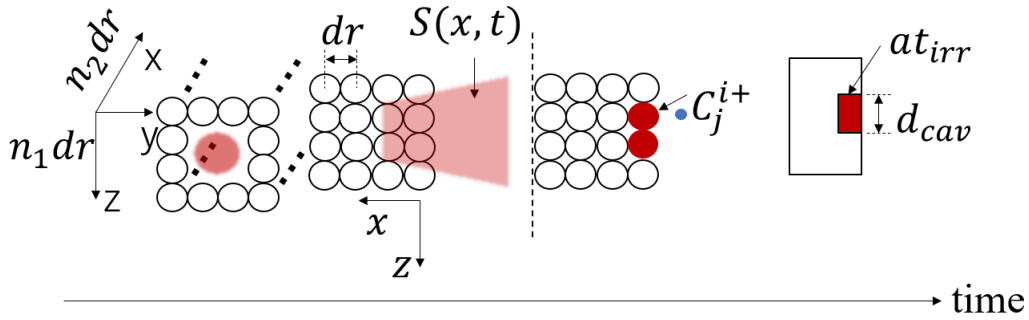

FIGURE 3.3: Simulation schematic of laser ablation on a graphite target

3.2 Electron production

3.2.1 Ionization via MPI

In electron production of laser ablation plasmas, the initial mechanism involves ionization via MPI. A simulation is performed in FORTRAN 90 via GNU Fortran in counting the electrons produced by an ablation laser. The simulation is set up in 3D coordinates with x is specified along the target surface normal. A 1064 nm wavelength laser with full width half maximum (FWHM) of 5 ns and 5 GW/cm^2 laser intensity is incident on a graphite target at the origin $x = 0, y = 0, z = 0$, and assumed to have a Gaussian form of

$$S(x,y,z,t) = I_o e^{-x/\lambda_D} e^{-\frac{(t-t_{peak})^2}{2\sigma_t^2}} e^{-\frac{(y-y_c)^2}{2\sigma_y^2}} e^{-\frac{(z-z_c)^2}{2\sigma_z^2}} \tag{3.8}$$

where I_o is the peak laser intensity, $\lambda_D = 1.5dr$ is the decay rate of the laser intensity along the target surface normal.

The pulse peak is located at t = 30 ns. The timestep employed in the simulation is 1 ps. Atoms are placed in 3D coordinates each with spacing dr = 0.2 nm to simulate distance between carbon atoms, with $n2$ atoms placed in the x-plane and n1 by n1 atoms in the y-z plane. Here $n2$ = 10, $n1$ = 20 is employed. The atoms are located on the target surface are arranged in the y-z plane labelled from 1-100, and 101-200 for $x = dr$, and so on. These numbers serve as the atom label. Figure 3.3 shows the simulation schematic of laser ablation on the graphite target.

The purpose of the simulation is to demonstrate electron and ion production by laser ablation via MPI. In order to generate electrons via MPI, a Monte Carlo simulation is adopted. When the laser strikes the target, the atoms are ionized according to the rate W^{MPI}, that is, for an m^{th} atom from an initial state i to a final state f [13]

$$R_{if}(m)\Delta t > N_R(m), \tag{3.9}$$

where R_{if} is the transition rate from i to f, in this case, W^{MPI}, Δt is the timestep, and N_R is a random number assigned to an atom. When an electron

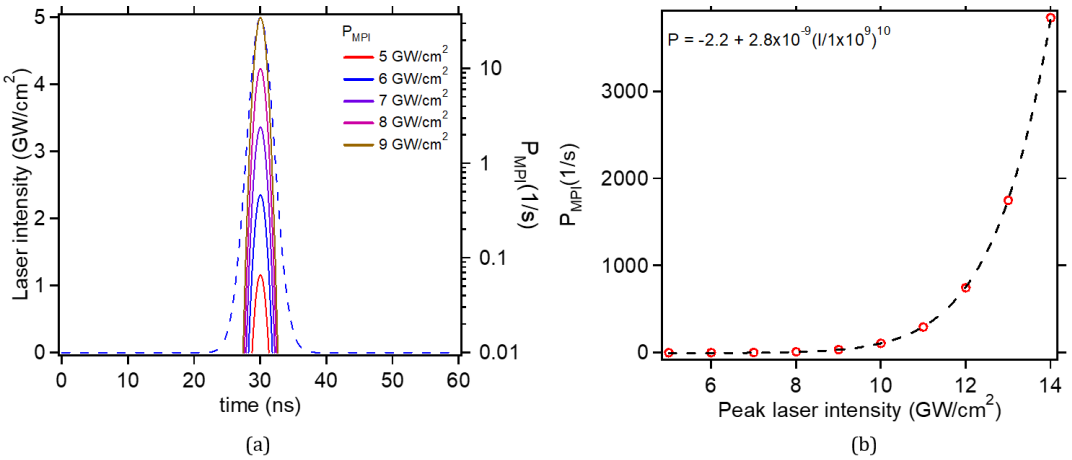

FIGURE 3.4: (a) Laser intensity and MPI probability versus time (b) MPI probability versus peak laser intensity

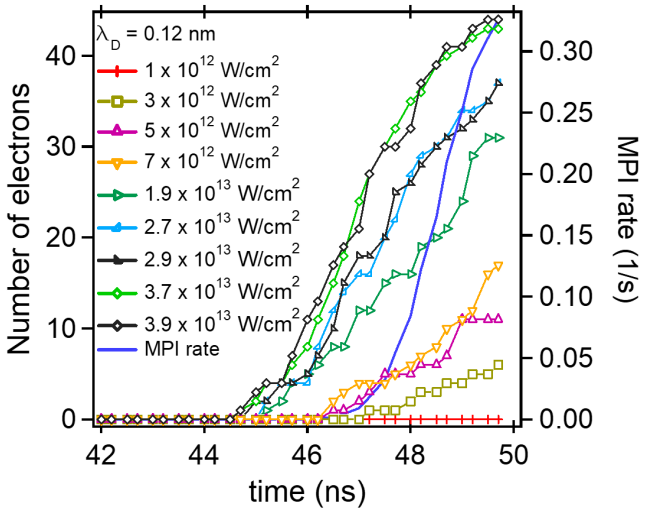

FIGURE 3.5: Number of electrons generated by MPI vs time for varying laser intensities, the MPI rate shown in blue line is for the laser pulse at 1 GW/cm2 laser intensity

and an ion are generated simultaneously, and the location of the ionized atom is recorded.

3.3 Simulation results

3.3.1 Electron production via MPI

Figure 3.4a shows the probability of MPI versus time of the laser pulse. The laser intensity is shown as dashed lines. The MPI probability is highest above the FWHM of the laser pulse. Taking the peak laser intensity, the right side of Figure 3.4b shows the dependence of MPI probability on the peak laser intensity. The MPI probability has a power law dependence with the laser intensity.

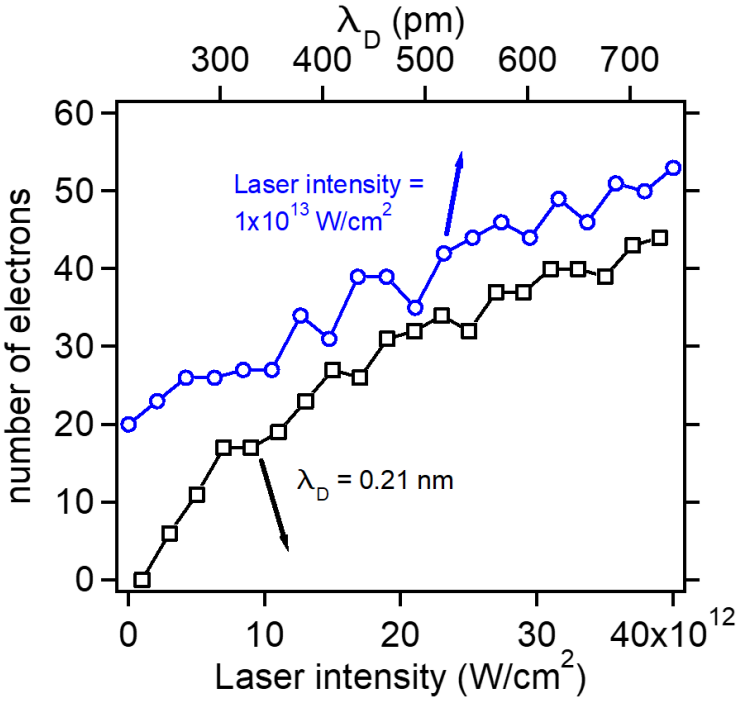

FIGURE 3.6: Maximum number of electrons versus laser penetration depth λ_D and laser intensity

Figure 3.5 shows the number of electrons generated by MPI for varying laser intensities. Here the laser pulse peak is shifted to 50 ns. It is observed that the number of electrons increases with increasing the laser intensity. No electrons are produced at $1 \times 10^{12}\ W/cm^2$ laser intensity, which is indicative of the threshold intensity at which MPI could hold. At $3.7 \times 10^{13}\ W/cm^2$ and $3.9 \times 10^{13}\ W/cm^2$ laser intensity, the rate of increase of number of electrons slows down. This is due to the decrease in the number of atoms ionized as the laser penetrates further on the target. Figure 3.6 shows the maximum number of electrons versus the laser penetration depth and laser intensity. It can be observed that as the laser intensity increases at a fixed penetration depth, the rate of increase of the number of electrons become slower above $1 \times 10^{13}\ W/cm^2$, while increasing the laser penetration depth at a fixed density does not significantly affect the rate of increase of number of electrons. The change in laser penetration depth can be related to the variation of target material, rather than the change in laser intensity. In order to visualize the ionized electrons in the target, the labelled ions are shown in Fig. 3.7, where the incident laser is perpendicular to the target surface.

At later times, the positions of the ionized atoms are located deeper within the target (indicated by the negative values). Both plots show that the highest number of produced electrons are located at the surface. As the depth increases, the number of ionized atoms decreases, as is expected due to the attenuation of the laser light with increasing depth. Moreover, a Gaussian shape of the laser pulse shows non-uniformity in the entire area of the laser incidence.

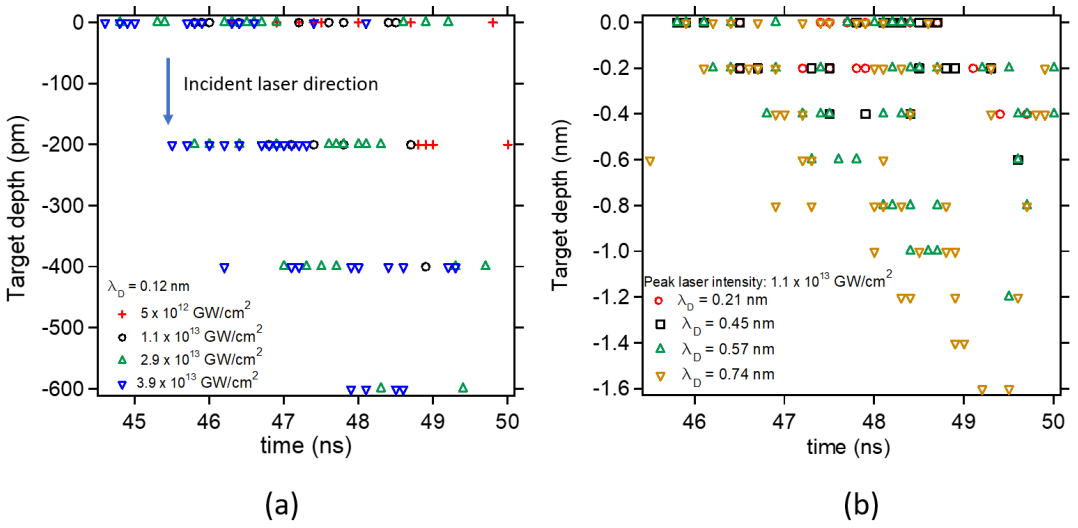

FIGURE 3.7: Positions of ionized electrons for (a) fixed penetration depth and varying laser intensity (b) fixed laser intensity and varying laser penetration depth

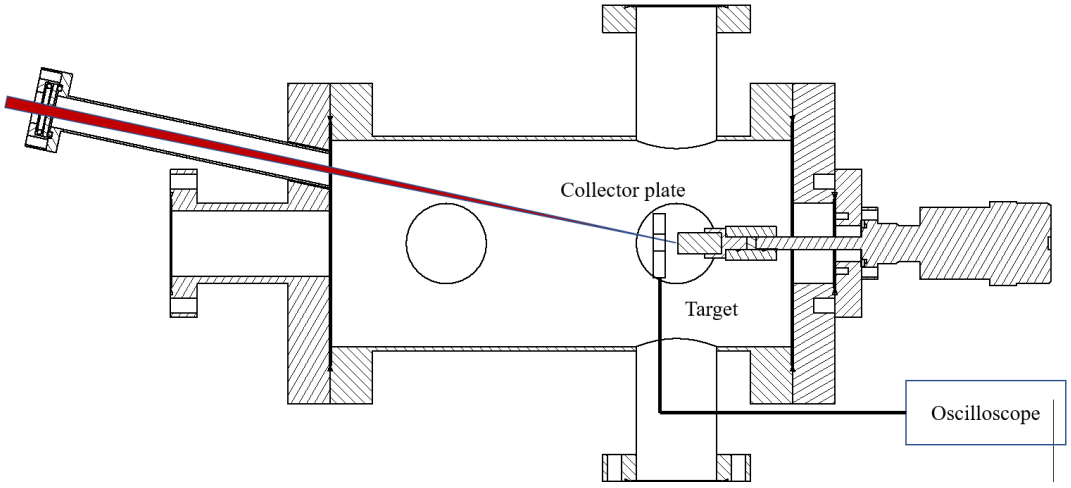

FIGURE 3.8: Experimental schematic for charge collection

3.4 Experiment schematic

With the production of the plasma plume, electrons and atoms collide to form ions. Electron production is investigated in the present setup by assembling a charge collector near the target surface. Fig. 3.8 shows the schematic of the charge collection experiment. The laser is incident on the center of the graphite target surface, where an aluminum plate is placed 5 mm from the target surface. The plate is connected to an oscilloscope terminated by a 50 Ω resistor. In order to determine the effects of increasing laser pulses, the target is repeatedly ablated while the laser is fired on the target at 10 Hz repetition rate. Experiments are performed inside a vacuum chamber with a base pressure of 5×10^{-6} Pa.

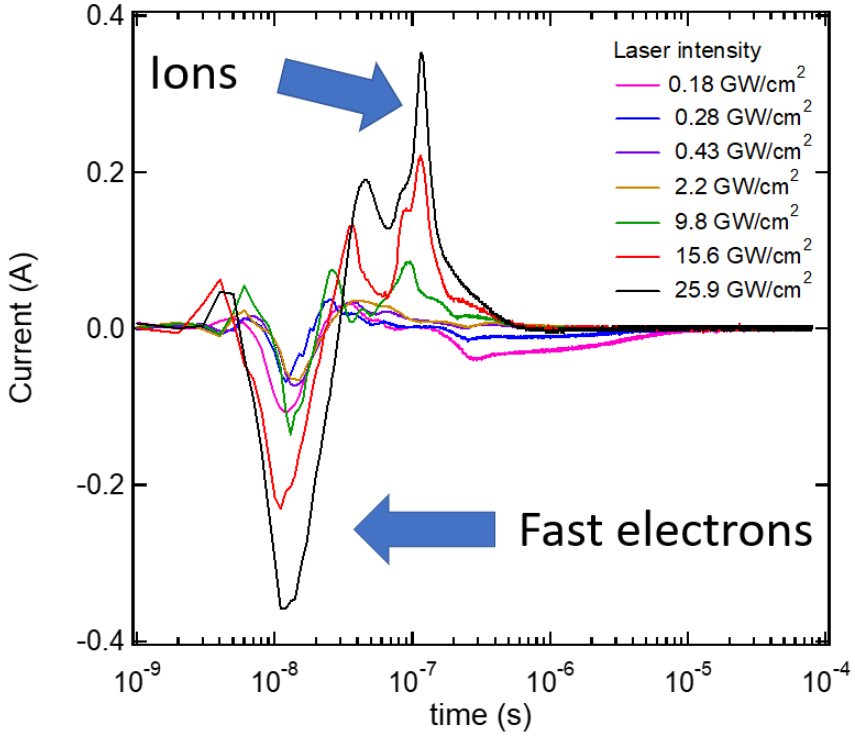

FIGURE 3.9: Experimental schematic for near-target charge collection

3.5 Charge collection results

Figure 3.9 shows the time-of-flight signals collected by the charge collector near the target. Electron signals are first detected at approximately 10 ns, followed by positive ion signals at approximately 100 ns. At 0.18 GW/cm^2 laser intensity, negative signals follow and persist until 10 μs. For increasing laser intensities. Higher signal amplitude for both positive and negative signals are observed, signifying the increase in laser energy available for ablating the target. As the laser intensity is increased, the width of the electron peak is also broadened. This indicates that energy width produced by the laser increases. One of the reasons for this increase in width is related to the laser and its penetration to the target. Increase in laser intensity results to the increase in ablation depth of the material. When the laser is incident on the target, the energy which is transferred to the target decreases as the depth increases. Thus lower available energy leads to lower ablation rate, and lower energy transfer from the laser to the electrons, leading to longer times of flight. However, the similar argument may not be applied to the ions, since only amplitude increases for increasing laser intensity. The TOF signals are integrated to obtain the charge. Figure 3.10 shows the charge obtained with increasing laser intensity. Increasing the laser intensity leads to the charge with a negative value, which indicates that the signals produce more electrons than ions near the surface as the laser energy increases. The phrase 'near the surface' is added since some electrons may not propagate in the direction of the plume due to collisions with the expanding plasma,

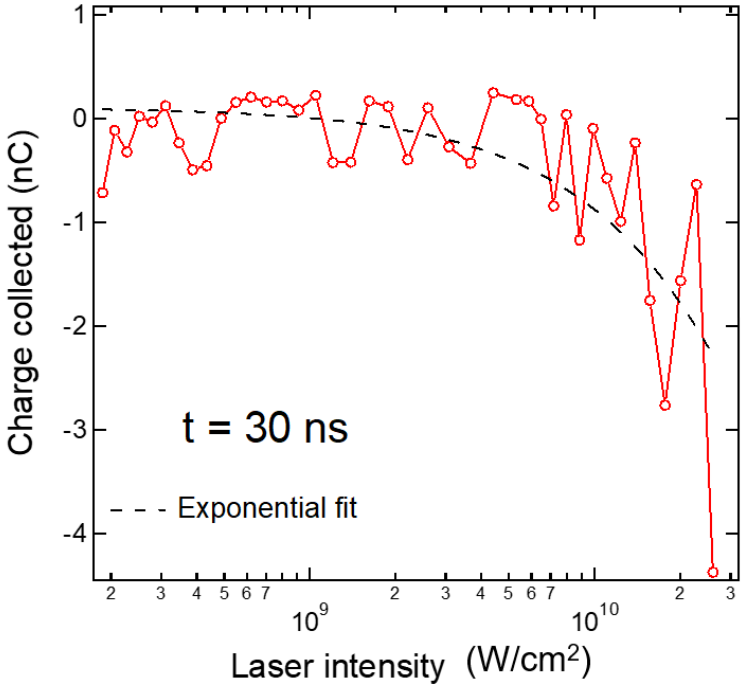

FIGURE 3.10: Charge collected from the TOF signals at t = 30 ns at varying laser intensities

leading to lower electron current intensity in the time of flight signals collected 570 mm from the target.

An attempt to fit the electron signals towards a description of ionization via electron impact ionization and recombination is performed. The electron signals from the collected time of flight spectra are fitted with a rate equation model given by

$$\frac{dn_e(\epsilon)}{dt} = n_e(\epsilon)\nu_{EI} - n_e(\epsilon)\nu_{recom}, \tag{3.10}$$

where n_e is the number of electrons (specified here as the collected current), ν_{EI} is the electron impact ionization coefficient and ν_{recom} is the recombination coefficient. Assuming an initial Maxwellian distribution

$$n_e(\epsilon) = 2\sqrt{\frac{\epsilon - \epsilon_{thresh}}{\pi}} \left(\frac{1}{kT}\right)^{3/2} e^{-(\epsilon-\epsilon_{thresh})/kT} \tag{3.11}$$

The electron impact ionization and electron recombination is assumed to occur simultaneously in each timestep. Also, the energies for EI are assumed to be sufficient. During electron impact ionization, the energy of the initial distribution is subtracted by kT, and the number of electrons corresponding to the *previous* initial distribution decreases, while the number of electrons having the *new* energy increases. However, when the energy is lower than a certain threshold ϵ_{thresh}, recombination would occur, in turn losing electrons in the process.

Figure 3.11 shows the electron time of flight signal at 25.9 GW/cm^2 laser intensity obtained from the negative peak in Fig. 3.9, and the fitted current

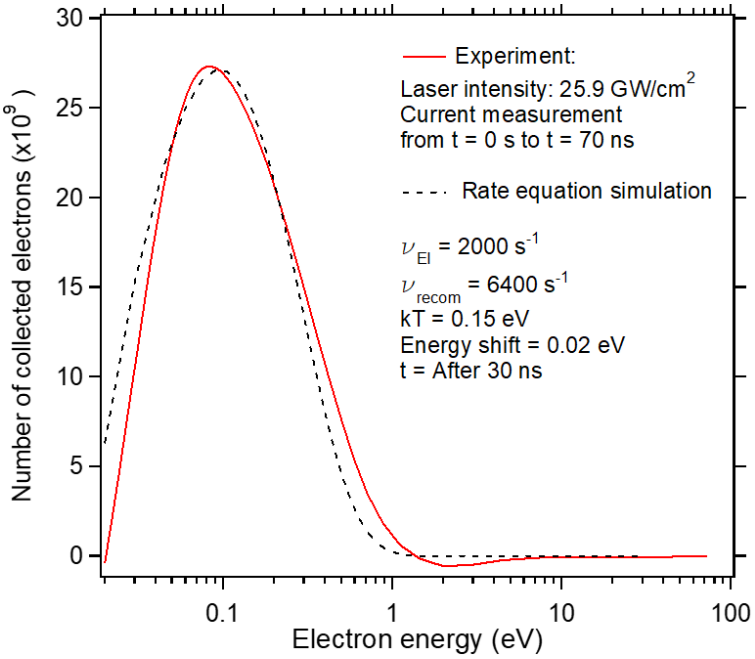

FIGURE 3.11: Electron energy distribution obtained from the current obtained from electron time of flight signals (red line) and fit from the rate equation model (black dashed line)

in the time frame from t = 0 to t = 70 ns. The pulse peak is set to be 1064 nm wavelength, 5 ns pulse width, at 30 ns peak time. The EI coefficients as well as the recombination coefficients are incorporated. Although there is a good fit with the experiment, the following assumptions should be considered: The EI and recombination coefficients, as well as any other mechanism involved in the electron production and plasma formation, are not constant, since the electron energy varies in time. The assumption of an initial Maxwellian form of the electron energy distribution implies that the plasma is assumed to achieve thermal equilibrium. Therefore, there the model may be further improved considering these assumptions.

Figure 3.12 shows the effect of increasing number of pulses on the electron and ion signals collected 4 mm from the target surface. At 10000 pulses, the peak shift towards later times shows reduction in electron energy as inelastic collisions occur within the plume before propagating towards the detectors. For an electron with mass m, flight path d and energies ϵ_1 and ϵ_2 corresponding to times-of-flight t_1 and t_2 after the fresh and after 10000 pulse ablation respectively, the energy loss can be estimated by

$$\epsilon_2 - \epsilon_1 = \frac{1}{2} m d^2 \left(\frac{1}{t_2^2} - \frac{1}{t_1^2} \right). \tag{3.12}$$

From the charge collection results, the electron kinetic energy can be estimated for a fresh target, that is, without a cavity, to be 0.87 eV. From Eq. 3.12, the energy loss corresponds to 0.73 eV, after 10000 pulses ablation. This indicates the energy losses exhibited by the electrons as they underwent

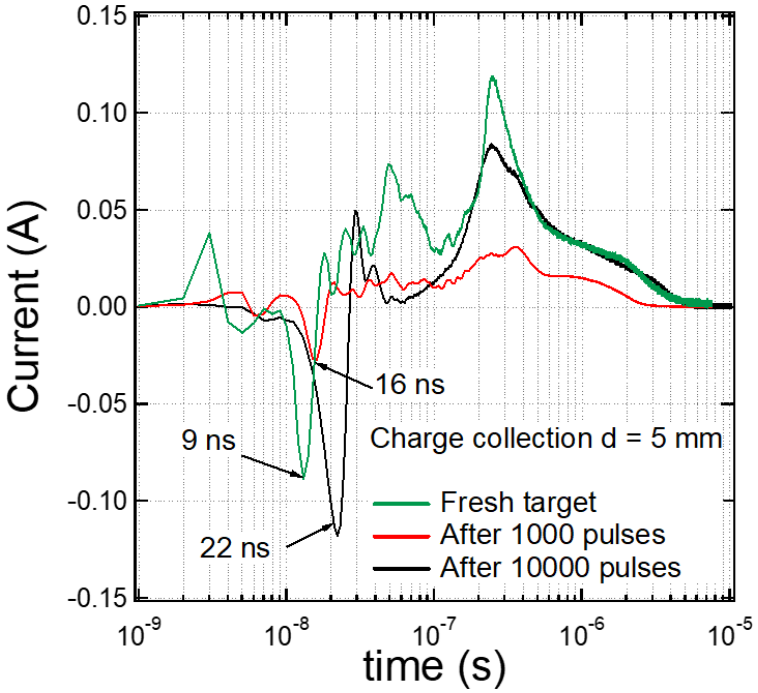

FIGURE 3.12: Effect of number of pulses at 5 GW/cm^2 laser intensity on the charge collected ion signals

inelastic collisions with the target cavity.

3.6 Summary

The electron production mechanism of nanosecond pulsed laser is described. Simulations involving multiphoton ionization and electron impact ionization via a rate equation model are performed to describe electron production via the laser. The models showed increase number of produced electrons with increasing laser intensity. The fit of the electron distributions from collected electron signal to the rate equation model showed agreement, however significant improvement towards the evolution of the rate coefficients must be performed. A charge collection near the target is performed to investigate electron signals near the surface. Increasing laser intensities increase electron signal amplitude and decreases their flight time. Increasing the number of laser pulses increases the flight time, which is attributed to electron energy losses as a cavity is formed on the target.

References

[1] W. Bleakney, Phys. Rev., **34**, 157 (1929).

[2] Nier, A.O. Rev. Sci. Instrum., **18**, 415 (1947).

[3] E. de Hoffmann, V. Stroobant, *Mass Spectrometry Principles and Applications* West Sussex: John Wiley & Sons (2007), p. 16.

[4] H. Niakan, Q. Yang, and J. A. Szpunar, Surf. Coat. Technol. **223**, 11–16 (2013).

[5] S. Sinha, J. Laser Appl. **30** 012008 (2018).

[6] N.M. Bulgakova and A.V. Bulgakov, Appl. Phys. A **73**, 199–208 (2001).

[7] Y. Zhang, D. Zhang, J. Wu, Z. He, and X. Deng, AIP Adv. **7**, 075010 (2017).

[8] R. Stoian, Appl. Phys. A **126** 438 (2020).

[9] G. Mainfray and C. Manus, Rep. Prog. Phys. **54** 1333-1372 (1991).

[10] L. V. Keldysh, Sov. Phys. JETP. **20** 1307 (1965).

[11] Y. Kishimoto and S. Kato, J. Plasma Fusion Res. 90, **7** 412-418 (2014).

[12] J. K. Koga *et al* J. Phys. D: Appl. Phys. **43** 025204 (2010).

[13] K. Moribayashi, J. Phys. B: At. Mol. Opt. Phys., **43**, 165602 (2010).

Chapter 4

Ion extraction of target cavity confined plasmas

4.1 Positive and negative ion formation

In the formation of laser plasmas, ion production follows fast electron generation. Nanosecond laser ablation was observed to produce singly and multiply charged ions. One example of ions produced by nanosecond laser ablation is the C^{6+} produced by direct laser injection to the target surface using a 1.4 J energy, at 1064 nm wavelength, 10 ns pulse duration laser [1]. Although the spectrum within the laser produced plasma consist of singly and multiply charged ions, in the case of graphite ablation, the dominant constituent is the C_2 and C_3 cluster ions [2, 15]. In terms of cluster production via laser ablation, synthesis of carbon clusters has been performed by Creasy and Brenna, where masses > 100 have been observed [3]. Ablation of graphite under N_2 environment was found to have a carbon mass spectra up to 500 carbon atoms [4, 5]. Varying laser parameters by employing femtosecond pulsed lasers also produce large carbon clusters [6]. Clusters produced were also investigated in the accompaniment of molecular beams and magnetic fields, providing enhancement of the detected ion signal [7, 8]. Laser ablation, then, has been a promising method for the production of these heavy clusters.

The cluster ion formation mechanism consists of several pathways in which collisions play an active role. In the formation of laser plasmas, the initial energy in the expansion is high, followed by the cooling of the plume via collisions [9, 10]. The cooling within the plume enables condensation leading to cluster formation.

Aside from positive ions, laser ablation also results to negative ion production. Negative ion production involves several mechanisms mainly due to electronic, ionic, and atomic collisions. Some of these mechanisms including high intensity lasers involve thermionic emission and surface ionization. When an electron collides with an atom, instead of electron ionization (which results to positive ions), *electron attachment* occurs, which translates the overall ionic charge to negative. The mechanism is described as [11]:

$$A^0 + e^- + e^- \rightarrow A^- + e^- \tag{4.1}$$

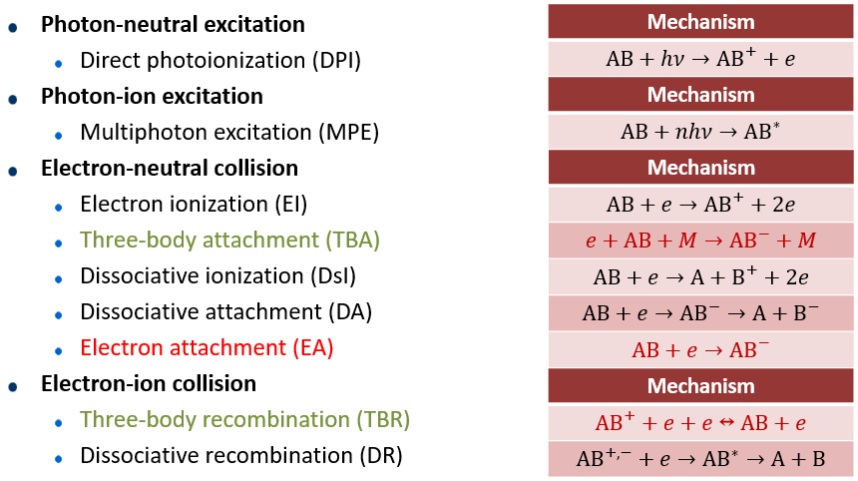

FIGURE 4.1: Positive and negative ion production mechanisms

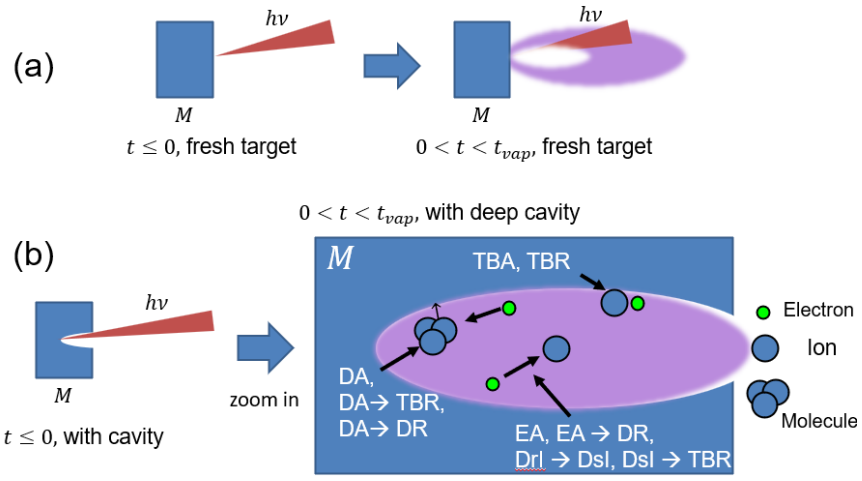

FIGURE 4.2: Mechanisms for a (a) fresh target, (b) cavity-induced target

Figure 4.1 shows the various mechanisms in ion formation. Under electron neutral collisions, there are several mechanisms involved in laser ablation, which is summarized in Fig. 4.2. In the negative ion formation via a laser with a cavity, the possible mechanisms involve three body attachment since the target can facilitate collisions. In particular, for a three-body attachment mechanism, the target is represented by a neutrally charged atom where electrons can form ions after losing kinetic energy through colliding with the cavity walls. On another note, three body recombination is also involved in the destruction of the negative (or positive) ion, since the cavity acts as a confining region to increase collisions between electrons and ions. These mechanisms occur simultaneously upon laser ablation.

Ions formed by laser ablation, regardless of which mechanism they are formed, exhibit broad energy and mass distributions that is described by shifted Maxwell-Boltzmann distribution functions [14, 15]. In this description, the plasma is assumed to have underwent thermal equilibrium. However, there are no previous reports, as far as this work is conceived, that

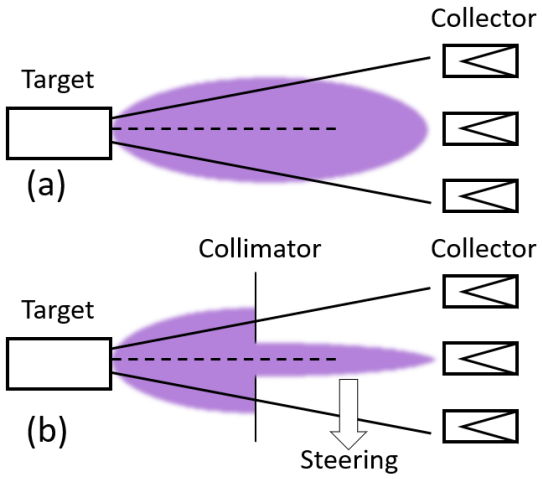

FIGURE 4.3: Schematic of ion beam propagation (a) without (b) with the installation of a downstream collimator

assumes an equilibrium state from a target cavity confined plasma. It is then more appropriate to forego the assumption of equilibrium in this type of plasma.

Thus far, the plasmas are described by a convolution of broad mass and energy ion distributions. In this chapter, designs and experiments towards resolving the masses and energies of target cavity confined plasmas are described. In the design of mass and energy-resolving experimental setups, the einzel lens and magnetic deflector analyzer are described in the following subsections.

4.1.1 Ion optics: the einzel lens

Electrons and ions in a laser plasma propagate in the direction perpendicular to the target surface and is divergent along the flight tube, as shown in Fig. 4.3a. Thus, the beam diameter of the laser plasma increases downstream. The charges are collected from the Faraday cups, therefore, results to a broad beam energy distribution.

In order to mitigate these broad ion energy distributions, beam collimation is necessary. This is achieved by realizing the fact that electron and ion trajectories can be manipulated by electromagnetic fields similar to that of an optical lens, such as shown in Fig. 4.3b. In a typical optical system, there exists an object and an image point, which serves as the source and destination of light, respectively. The focal point of light is dictated by the lens equation and is dependent on the focal lengths of the object and image. In electron and ion optics, the motion is governed by Lorentz force induced by external electromagnetic fields. In focusing the electron and ion beams, ion lenses consisting of axially symmetric geometry and circular apertures. The Einzel lens, or a unipotential lens, is one such type of electron and ion lens for which the potential is the same for the image and object side [16]. In practice, the einzel lens is a biased plate between two regions with equal potential [17]. For simplicity, these two regions are kept grounded. Figure

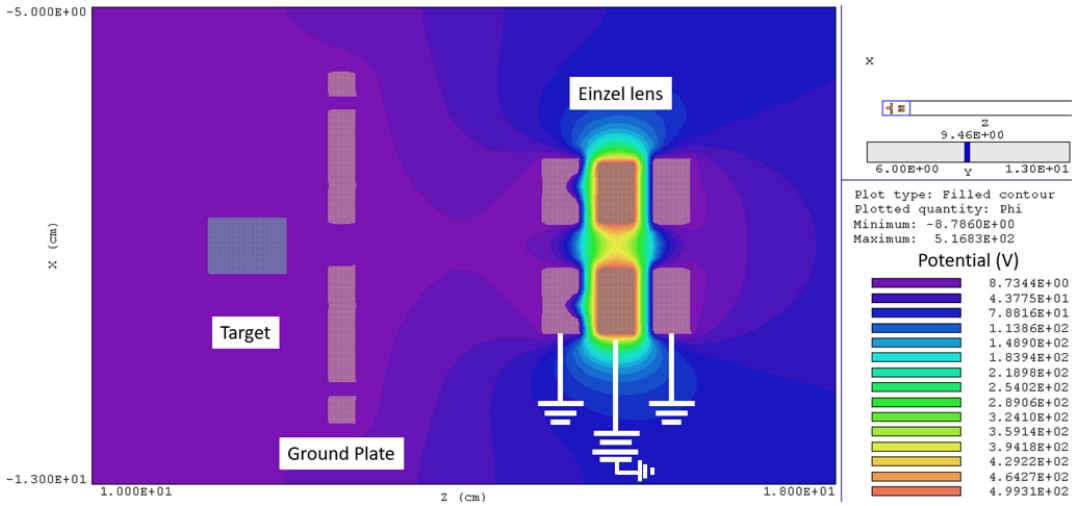

FIGURE 4.4: Schematic and potential distribution of an Einzel lens

4.4 shows the schematic and potential distribution of the einzel lens with 2 mm spacing and 4 mm thickness. The potential between the plates along the aperture axis is within 20 percent of the bias.

Depending on the application, the beam energy can be changed depending on the lens structure. Since the objective of this study involves the determination of ion beam energy, the utilization of a symmetric lens is sought. The symmetric lens provides ion beam focusing while conserving the beam energy. Experimentally, providing beam focusing, the ion beam energy is swept through various potential values while the time of flight is measured by the Faraday cup array. When the width of the ion current from the time-of-flight spectrum is at its smallest during the sweep, or when the peak current collected by the Faraday cup is highest, beam focusing is achieved. With beam collimation, steering of ion beam trajectories may be performed downstream via installation of electromagnetic deflectors.

Figure 4.5a shows the trajectory simulation of carbon ions for varying lens bias for an ion energy of $V_{ion} = 1$ kV and $V_{lens} = 500$ V. A lens-to-energy ratio V_{lens}/V_{ion} is defined to generalize the dependence of the focal length electrostatic lens bias and the ion energy. The focal length dependence on the lens-to-energy ratio is shown in Fig. 4.5b. For a high lens to energy ratio, the focal length significantly decreases up to a point where almost no ions are able to travel at the 60 cm mark. If a longer focal length is necessary, the lens sensitivity increases since sweeping the electrostatic lens bias becomes significant at lower voltage.

An electrostatic lens is designed, fabricated, and assembled to investigate the focusing of the laser plasma, as shown in Fig. 4.6. The assembly consists of aluminum plates with 4 mm thickness each with 8 mm aperture. The electrostatic plates are held by a grounded aluminum plate on an SUS 152-70 adapter flange.

The performance of the lens is investigated by measuring the time of flight signals using the Faraday cup assembly as shown in Fig. 4.7. Laser

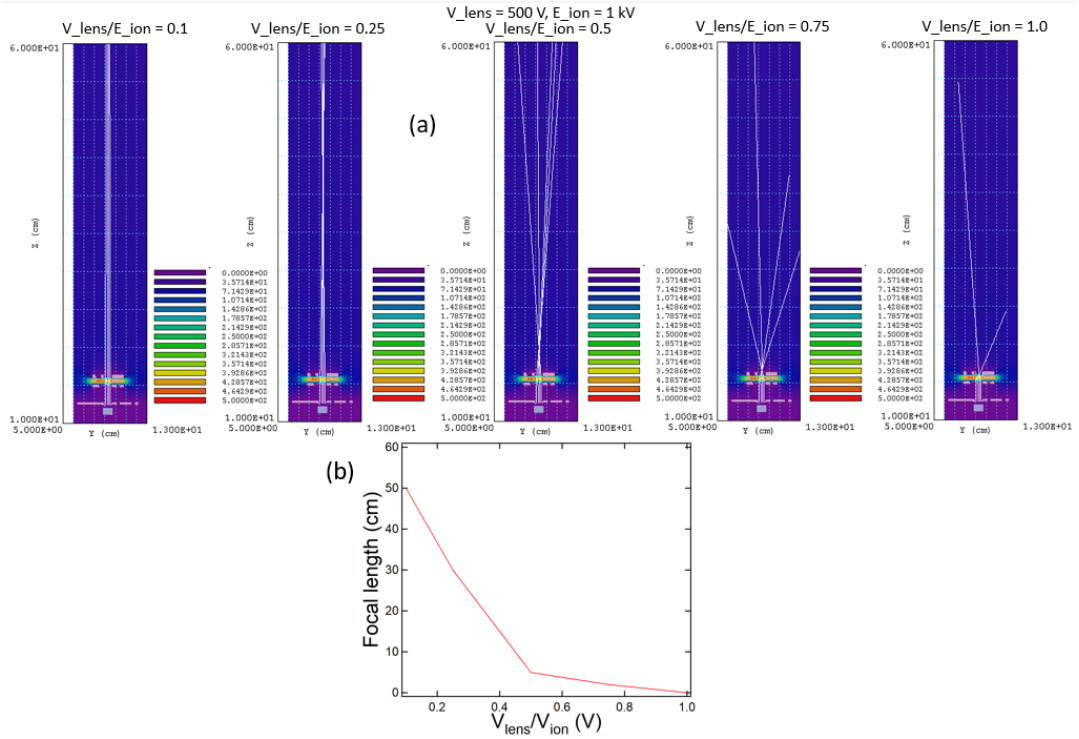

FIGURE 4.5: (a) Carbon ion trajectories for increasing electrostatic lens bias V_{lens}, ion energies are represented by V_{ion} (b) Ion focal length for varying lens to energy ratio

parameters are as follows: 5GW/cm^2 laser intensity, 1064 nm wavelength, and 1 mm spot size. Four Faraday cups are labelled from FC 1 to FC 4. Here the main focus is FC 2, or the middle Faraday cup, since the area of interest is the ion focusing in this direction. Figure 4.8a shows the time-of-flight signals for varying electrostatic lens bias. Increasing the lens bias towards 600 V results to the narrowing of the peak width of the signal. Further increase of the lens voltage results to the decrease in the ion signal where at 800 V the signal is observed to have approximately 10 μs peak current. Decrease in ion signals with the increase of electrostatic lens voltage shows the ion defocusing where only higher energy ions can pass through. The significant ion current decrease with the lens bias increase from 700 to 800 V shows that the electron ion distribution fall within this range. In order to further show the comparison between these ion signals, the signals are integrated with respect to the time of flight using trapezoidal rule, as shown in Fig. 4.8b. After 10 μs, which was the point when the peak signal has receded, the highest amount of charge is exhibited by that of the 400 V lens bias, followed by 300 V and 0 V.

4.1.2 Magnetic field deflection of charged particles

Magnetic field deflection

In the attempt to investigate the effect of magnetic field on the ions propagating from a confined laser plasma, a magnetic deflection flange is

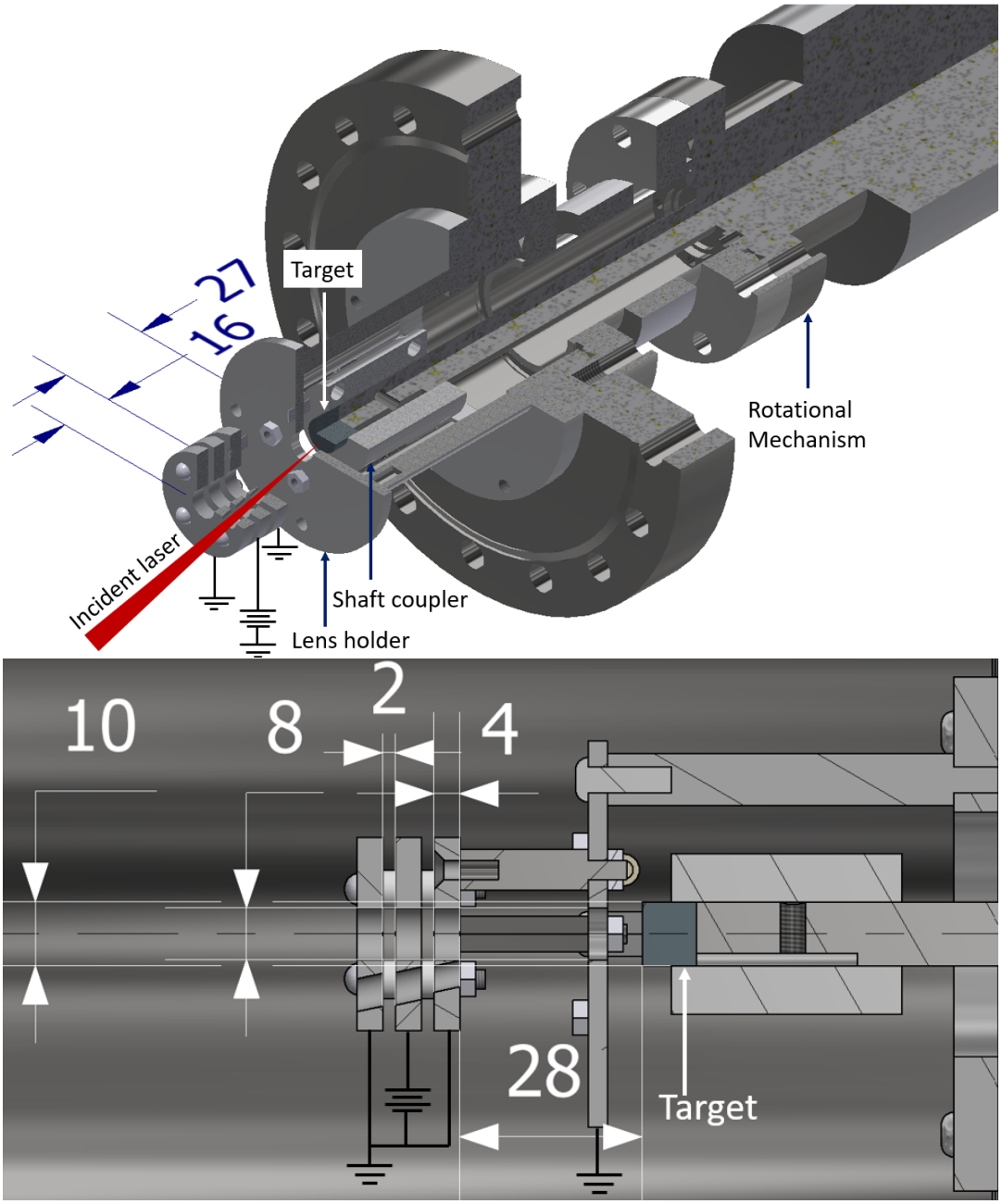

FIGURE 4.6: (a) Schematic of the Einzel lens assembly mounted on the target flange (units in mm) (b) Close-up image of the electrostatic lens assembly

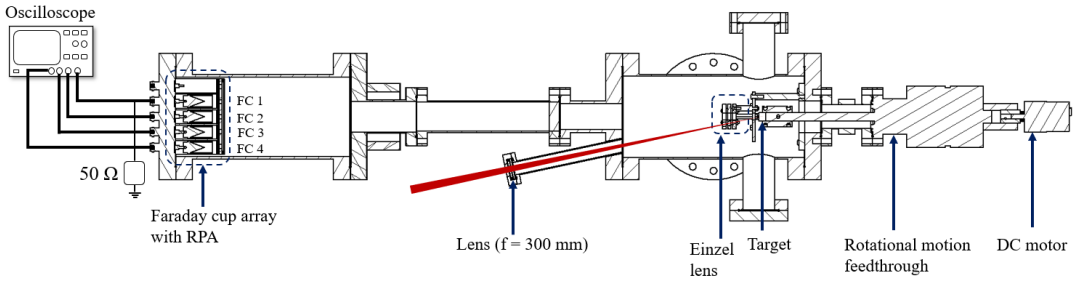

FIGURE 4.7: Experimental setup for ion diagnostics using electrostatic lens

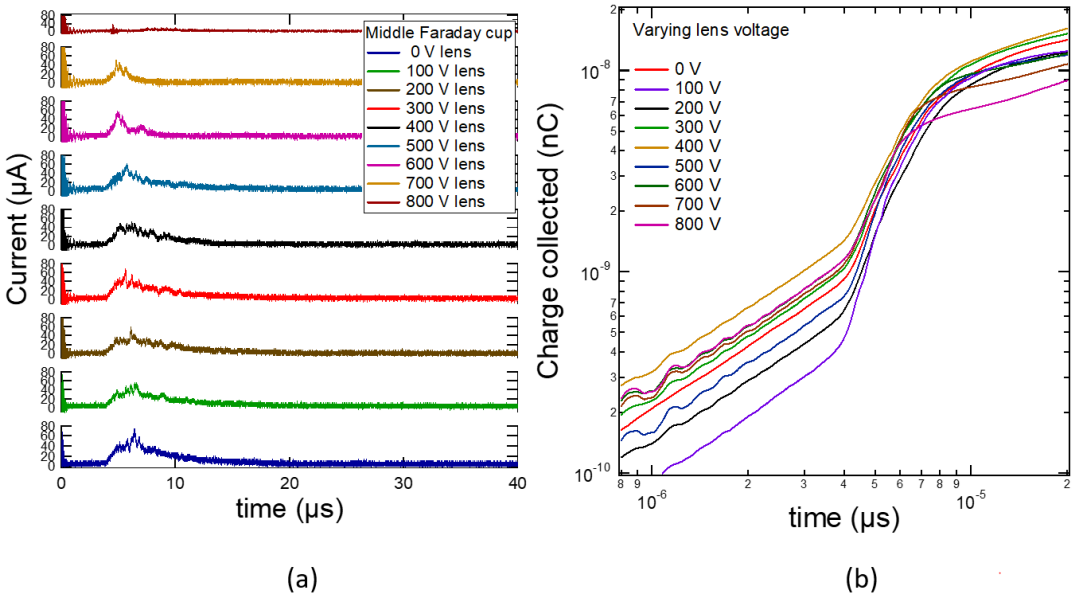

FIGURE 4.8: (a) Ion time of flight signals collected by the FC 2 (Faraday cup along the target axis) for varying electrostatic lens bias (b) Total charge collected for increasing electrostatic lens bias

designed and fabricated. The time-of-flight spectrometer with the installed deflection flange is shown in Fig. 4.9a, where an energy filter region is installed 4 mm from the target surface. The energy filter region consists of a 8 mm bias plate between two plates, labelled near and far plates. The deflection flange consists of a rectangular aperture with 37 mm height and 6 mm width, as shown in Fig. 4.9b. Neodymium permanent magnets are placed at 48 mm from the aperture with the magnetic field directed towards the side of laser incidence. The magnetic flux density results to a maximum of 80 Gauss. The Faraday cup configuration used in this experiment is shown in Fig. 4.9c. The target is rotated at a rate of 18 revolutions per minute using a DC motor during repeated laser ablation at 5 GW/cm^2 laser intensity. The signals collected were averaged over 16 shots. Experiments were performed inside a vacuum chamber at 6 $\times 10^{-6}$ Pa base pressure.

Figure 4.10 shows the time-of-flight spectra without and with the installation of permanent magnets. With the magnetic field as shown in

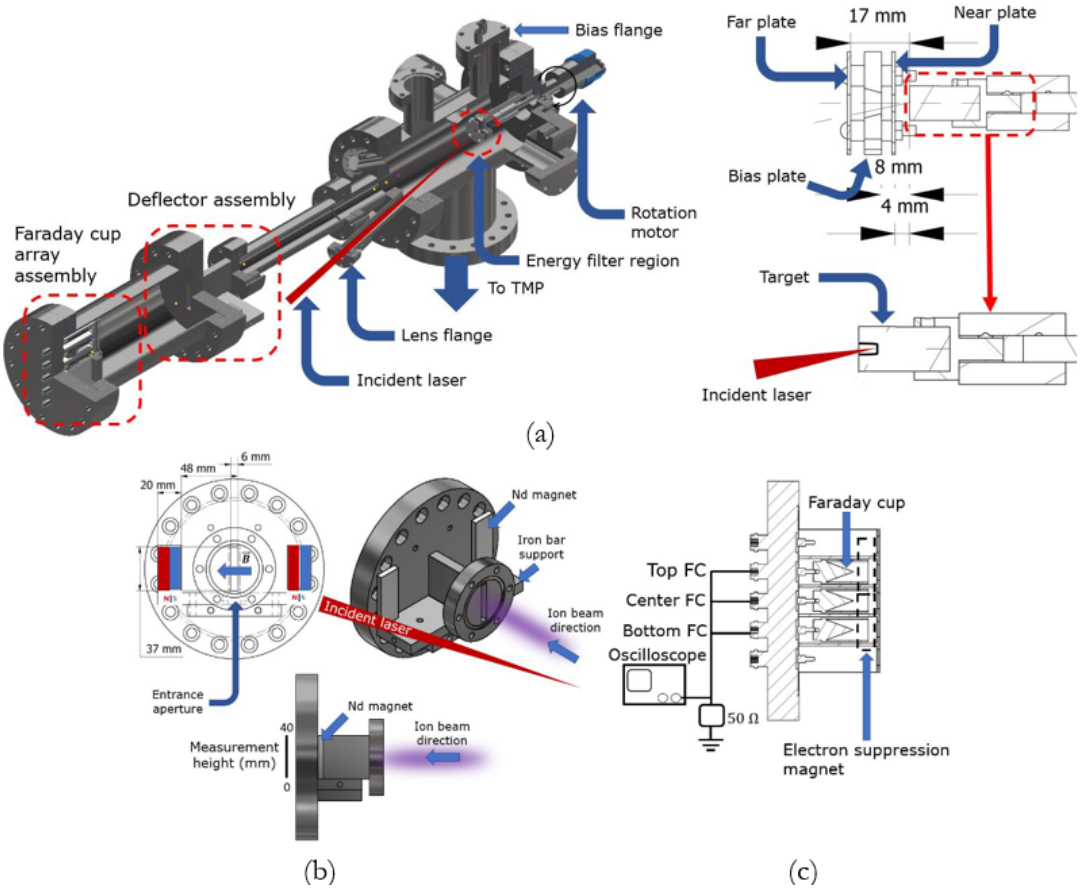

FIGURE 4.9: (a) Experimental schematic of the time-of-flight spectrometer with an energy filter near the target (b) Deflector assembly schematic (c) Structure of the Faraday cup array

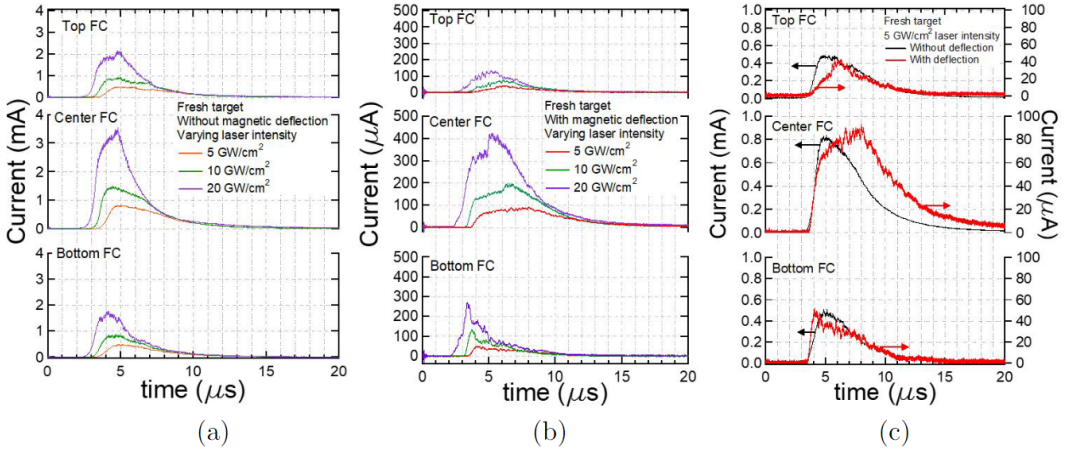

FIGURE 4.10: Ion time-of-flight signals for fresh target condition (a) Faraday cup array signals for varying laser intensity (b) Array signals with magnetic deflection assembly for varying intensities (c) Overlap of current signals for 5 GW/cm^2 laser intensity

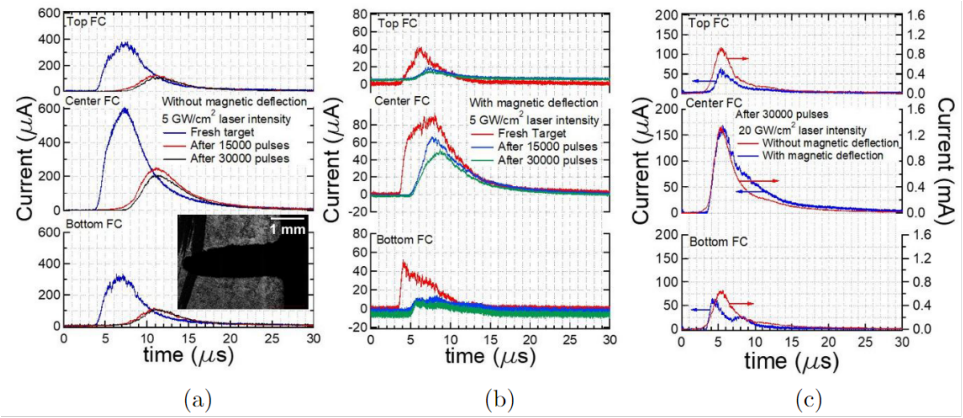

FIGURE 4.11: Ion signals due to fresh target ablation and after 5 GW/cm^2 drilling intensity ablation (a) Ion current signals for varying number of pulses, inset shows the cavity shape after 30000 pulses (b) Array signals under magnetic deflection for varying number of pulses (c) Comparison of ion signals with and without magnetic deflection at 20 GW/cm^2 laser intensity after 30000 pulses

Fig. 4.10b, the ion signal significantly decreased, with the center Faraday cup (labelled in the figures as FC) ion current decreased to almost one tenth of the signal without the magnets. This is due to the steering of higher mass and lower energy ions toward the direction of the bottom Faraday cup. However, the bottom Faraday cup does not collect more ions, but instead the current also lowered. In the comparison between without and with magnetic deflection in Fig. 4.10c at 5 GW/cm^2, the influence of the installation of permanent magnets slightly improved the resolution of the time of flight signals due to the emergence of narrow peaks within the broad distribution for all Faraday cup signals, which were not present without the field. In all the plots with and without magnetic field, the center Faraday cup collects the highest ion signal. Figure 4.11 shows the effect of number of pulses without and with the installation of permanent magnets. Increasing the number of pulses results to the shift of the signals toward later times while decreasing the ion current signal.

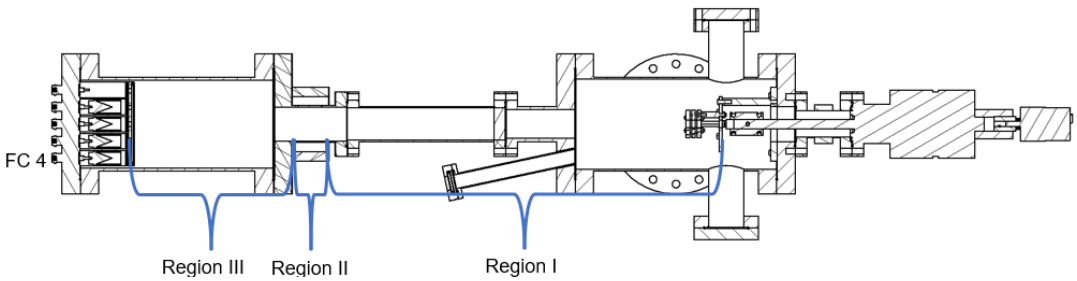

FIGURE 4.12: Schematic for calculating the trajectory due to magnetic deflection

Magnetic momentum analyzer

The previous subsection showed results of the ion deflection via a magnetic field. However, in order to determine ion deflection trajectories, the shape of the magnetic field distribution needs to be defined. Since the time of flight of the laser plasma consists of various mass and energy distributions, the masses should be resolved with a defined distribution of the magnetic field. In order to achieve mass resolution, a magnetic momentum analyzer is constructed. In a magnetic deflection system, ion trajectories are deflected perpendicular to the magnetic field direction. The trajectories can be estimated by assuming an extracted beam towards a deflection magnet. In the following, the trajectory of a carbon plasma is calculated with a schematic from Fig. 4.12. Ions propagate from the target, through the flight tube and towards the deflector magnet and towards the bottommost Faraday cup.

Given the ion TOF with a charge q, extraction voltage V, and mass m, let x be direction of plasma expansion, y be the direction of deflection (towards bottom FC). So z is parallel to the magnetic field lines (direction from north to south pole).

For an ion with mass m, charge q, and a velocity v,

$$v = \sqrt{\frac{2qV}{m}} \tag{4.2}$$

We have three regions: free field (Region I), deflection (Region II) (starting from the yoke), towards the FC (Region III)

For **region I** we have the equations of motion, in the first approximation

$$\begin{aligned} x_o &= v_o(t_o) \\ y_o &= 0 \\ v_{ox} &= x_o/t_o \\ v_{oy} &= 0, \end{aligned}$$

where the motion from the target to the deflection region is along the x-direction only. To obtain v we first assume a straight path. $v = 0.65m/4.74\mu s = 1.37 \times 10^5 m/s$. At time $t = t'$, the ion is exposed to deflection field with a function $B(x, y)$ (in Tesla). Since the B-field is space dependent, it is also time-dependent. The rate of change of $B(x, y)$ is:

$$\frac{dB}{dt} = \frac{dB}{dx}\frac{dx}{dt} + \frac{dB}{dy}\frac{dy}{dt} \tag{4.3}$$

For **region II** we have the equations of motion, in the zeroth order approximation, and $y = 0$:

$$m\frac{dv_x}{dt} = m\frac{d^2x}{dt^2} \tag{4.4}$$
$$= qv_yB_z = qv_yB \tag{4.5}$$
$$m\frac{dv_y}{dt} = m\frac{d^2y}{dt^2} \tag{4.6}$$
$$= -qv_xB_z \tag{4.7}$$
$$x(t) = x_o + v_{ox}(t - t_o) \tag{4.8}$$
$$y(t) = y_o + v_{oy}(t - t_o) + \frac{1}{2}\frac{qv_{ox}B(x,y)}{m}(t - t_o)^2 \tag{4.9}$$
$$= \frac{1}{2}\frac{qv_{ox}B(x,y)}{m}(t - t_o)^2, \tag{4.10}$$

where t_o is the time at which the ions enter the region II. At the boundary after deflection at $t = t''$, the ion has a velocity

$$v'_x = \frac{dx}{dt}_{t=t'} = v_{ox} \tag{4.11}$$
$$v'_y = \frac{dy}{dt}_{t=t'} = \frac{qv_{ox}B(x,y)}{m}_{t=t'}(t' - t_o) + \frac{1}{2}\frac{qv_o}{m}(t' - t_o)^2\frac{dB}{dt}_{t=t'} \tag{4.12}$$

where from Eqs. 4.3,4.9 we have

$$\frac{dB}{dt}_{t'} = \frac{dB}{dx}_{x(t')}v_{ox} + \frac{dB}{dy}_{y(t')}\frac{qv_{ox}B(x(t'),y(t'))}{m}(t' - t_o)$$

For **region III** we have the equations of motion

$$x(t) = x(t') + v'_x(t - t') \tag{4.13}$$
$$y(t) = y(t') + v'_y(t - t') \tag{4.14}$$

From Eq.4.12 and 4.14 we have

$$y(t'') = y(t') + \frac{dy}{dt}_{t=t'} \tag{4.15}$$
$$= y(t') + \left(\frac{qv_{ox}B(x,y)}{m}_{t=t'}(t' - t_o) + \frac{1}{2}\frac{qv_o}{m}(t' - t_o)^2\frac{dB}{dt}_{t=t'}\right)(t'' - t') \tag{4.16}$$

Expanding the term involving dB/dt, we have

$$\left(\frac{1}{2}\frac{qv_o}{m}(t' - t_o)^2\left[\frac{dB}{dx}_{x(t')}v_{ox} + \frac{dB}{dy}_{y(t')}\frac{qv_{ox}B(x(t'),y(t'))}{m}(t' - t_o)\right]\right)(t'' - t')$$

Plugging in the above expression and rearranging, we have

$$\frac{y(t'')-y(t')}{t''-t'}m^2 - \left[qvB(x(t'),y(t'))(t'-t_o) + \frac{1}{2}qv(t'-t_o)^2\frac{dB}{dx}\frac{dx}{dt}\right]m - \frac{1}{2}(qv)(qvB(t'))(t'-t_o)^2\frac{dB}{dy} = 0$$

Using the quadratic equation assuiming $dB/dy = 0$, we can solve for the mass. At $t = t''$, we have the TOF. We also have $v = v_{ox} = dx/dt = 138297m/s$. Also the time it takes to drift the deflection region is, $t' = (x(t') - x_o)/v_{ox} + t_o$. So, $t_o = 3.47\mu s$. The distances are:

- $x_o = 432.6mm$ `(from target to deflection region)`
- $x(t') - x_o = 40mm$ `(deflection region length)`
- $y(t'') = 18.5mm$ `(distance from FC center axis to FC bottom axis)`

For a TOF = 4.74 μs, we have

- $t' - t_o = 0.28\mu s$
- $t'' - t' = 1.34\mu s$

Using the graph from dB/dy at $x = 40mm$(at time $t = t'$) and at $y = 0mm$ (between the magnet), we have $dB/dy = 0$.

Using the graph from dB/dx at $y = 0mm$ and $x = 40mm$, we have $dB/dx = 3.675T/m$, $B(t') = 250G$. Also, assuming $y(t') = 0$ we have the AMU mass of carbon:

$$\begin{aligned} m(AMU_C) &= qvB(x(t'),y(t'))(t'-t_o) && (4.17)\\ &+ \frac{1}{2}qv^2(t'-t_o)^2\frac{dB}{dx}\times\frac{t''-t'}{(y(t'')-y(t'))}\times\frac{1}{(\mu)} && (4.18)\\ &= (1.602\times10^{-19}C)(138297m/s)(0.025T)(0.28\times10^{-6}) && (4.19)\\ &+ \frac{1}{2}(1.602\times10^{-19}C)(138297m/s)^2(0.28\times10^{-6})(3.675T/m)) && (4.20)\\ &\times\frac{1.34\times10^{-6}s}{0.0185m}\times\frac{1}{(12)(1.67\times10^{-27}kg)} && (4.21)\\ &= 2.15 && (4.22) \end{aligned}$$

which corresponds to the C_2^+ cluster ions. A way to check the validity of the assumption $y(t') = 0$ is to calculate the trajectory of the ion. The ion motion begins at $(x(t_o), y(t_o)) = (x_o, y_o)$ and is under the influence of magnetic field $B(x, y)$. The ion, then changes cyclotron radius for each time. From Figure 4.13, the following expressions can be obtained:

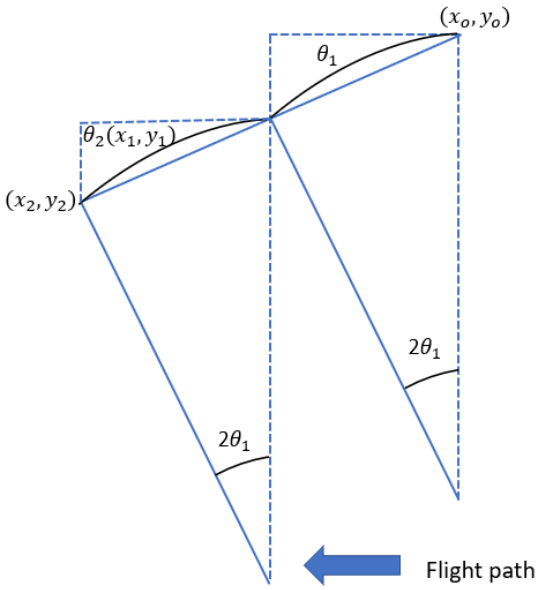

FIGURE 4.13: Simulation of ion trajectory within the deflection region

$$\sqrt{(x-x_o)^2+(y-y_o)^2} = 2r_1 \tan\theta\cos\theta \tag{4.23}$$

$$r_1(x,y) = \frac{(x-x_o)^2+(y-y_o)^2}{2(y-y_o)} \tag{4.24}$$

where the variable x, y and x_o, y_0 represent the initial and final positions in time. The path length is then the arc length given by the radius.

$$d = r(2\theta) \tag{4.25}$$

To determine the trajectory, we have from Eq.4.4:

$$x(t) = x_o + v_{ox}(t-t_o) \tag{4.26}$$

$$y(t) = y_o + v_{oy}(t-t_o) + \frac{1}{2}\frac{qv_{ox}B(x,y)}{m}(t-t_o)^2 \tag{4.27}$$

$$= \frac{1}{2}\frac{qv_{ox}B(x,y)}{m}(t-t_o)^2 \tag{4.28}$$

The velocities at an arbitrary position x, y and at an arbitrary time t_1' are then

$$v_x = v_{ox} \tag{4.29}$$

$$v_y = v_{oy} + (v^3B/V)(t_1' - t_o) \tag{4.30}$$

$$v = \sqrt{(v_x^2)+(v_y^2)} \tag{4.31}$$

where the last term in v_y is from $(1/2)mv^2 = qV$ and $(mv^2/R) = qvB$. The velocity v, and magnetic flux density B change as the ion propagates through

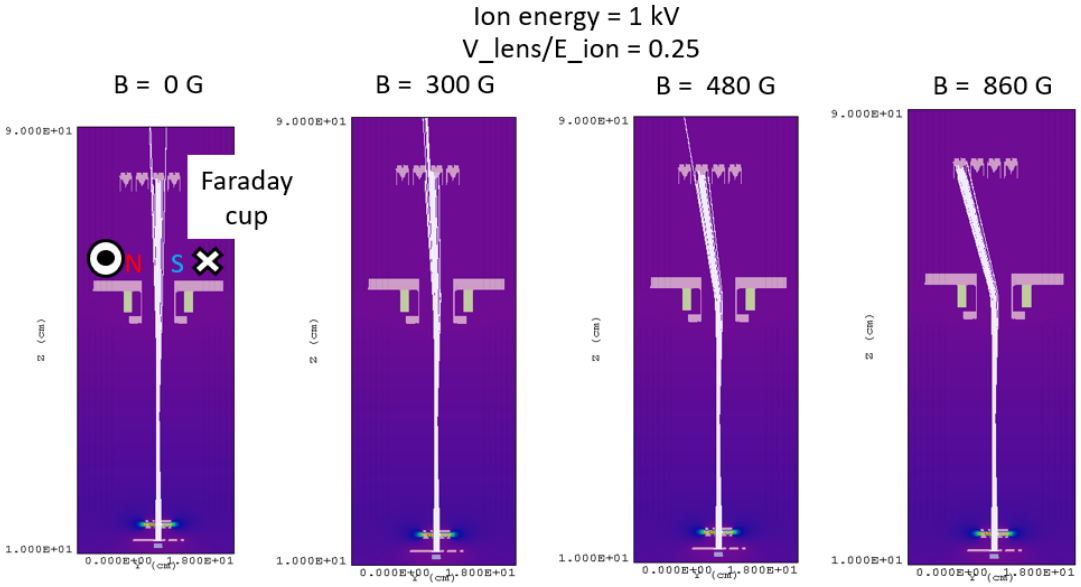

FIGURE 4.14: Carbon ion trajectory simulation for varying deflection magnetic flux densities

the deflection region. Since we have measured $B(x)$ and $B(y)$, the trajectory of the ions are described.

The magnetic field distribution of the assembly is dependent on the permanent magnets installed. Ion current will not be detected when the deflection field is too strong. Similarly, mass would not be resolved with too weak a magnetic field. This is demonstrated by simulating motion from an ion source towards a magnetic deflector region using AmaZe software. For illustration purposes, the magnetic field directions for the north magnetic pole and south magnetic pole are directed outside and inside the page respectively. Figure 4.14 shows the effect of magnetic flux density on the carbon ion trajectory with a $V_{lens}/V_{ion} = 0.25$, with an average ion energy of 1 kV whose Maxwellian distribution is generated using the GenDist Module of AmaZe software. It can be observed that the ions a minimum deflector flux density of approximately 30 mT (300 G) is required to deflect ions from the axis. At approximately 90 mT, most of the ions are deflected towards the direction of the leftmost Faraday cup. For a constant 300 G magnetic flux densities, the ion trajectories are shown in Fig. 4.15. As the ion energy is lowered down, the ion trajectory is further deflected towards the leftmost Faraday cup. This indicates that, at higher energies directed perpendicular to the target surface, ions have a preferential direction to be collected by the Faraday cup along the target axis. Since the current design assembly consists of the Faraday cups arranged in this particular fashion, it is desired to collect current signals from the leftmost (as for the 3D design, the bottommost Faraday cup, with 'bottommost' meaning that with the lowest gravitational potential) Faraday cup to demonstrate the performance of magnetic deflection. Moreover, the simulation results indicate that the lens voltage plays a smaller role for low energy ions, since 10 V bias led to the collection to Faraday cups. This may be seen as a disadvantage, since

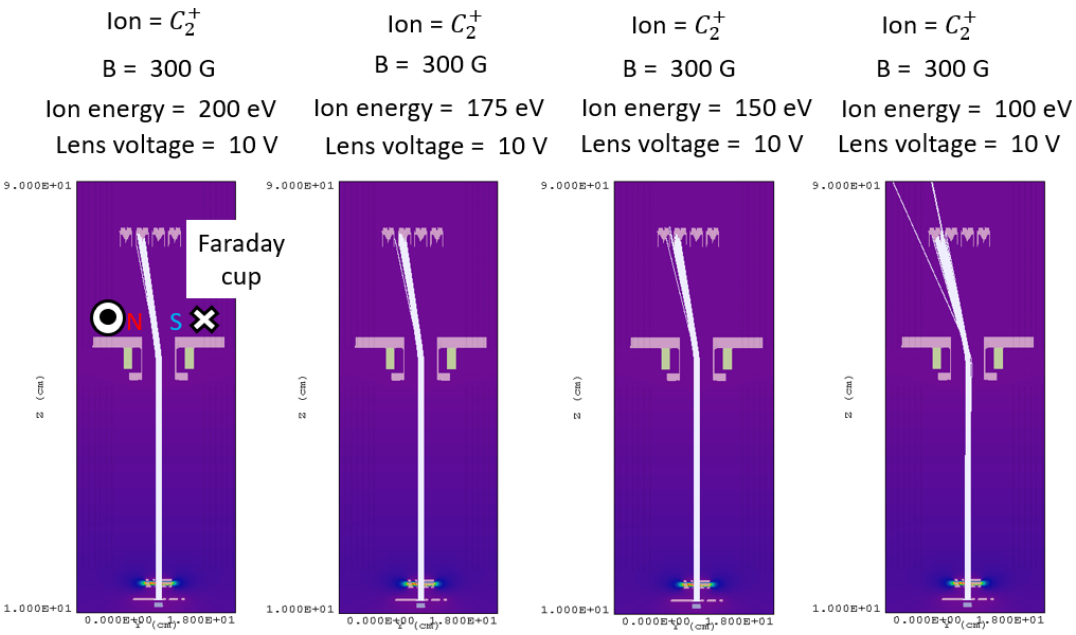

FIGURE 4.15: C_2^+ ion trajectory simulation for varying ion energy at 300 G magnetic flux density

low lens bias may significantly affect the ion focusing, therefore increasing the sensitivity of the ion optics.

A magnetic deflector analyzer is designed for resolving the ion masses by steering the ion beam laterally towards the off-axis charge collectors. The analyzer consists of cylindrical shaped neodymium permanent magnets with 30 mm diameter, 1 mm thickness and attached to an iron yoke as shown in Figure 4.16a. The analyzer aperture has a width of 6 mm and height of 37 mm. The bending magnet assembly is attached outside of the vacuum chamber. An image of the magnetic analyzer assembly is shown in Fig. 4.16c.

In order to demonstrate the effect of deflection on the ion signals, permanent magnets are installed on the deflector flange with the magnetic field configuration in 4.16a, with an effective magnetic flux density of 560 G at the aperture. The experimental schematic is shown in Fig. 4.17. Ion signals considered here are those collected by FC 4 (bottommost Faraday cup). Ion current increase from 1 μA to 10 μA, 8 μA to 56 μA, and 22.8 μA to 50 μA were observed with the installation of deflection magnets. For the 10 and 20 GW/cm^2 laser intensity in the case without deflection shows two distinct peaks at 6 μs time-of-flight, which disappeared when the deflection magnets are installed. The emergence of the peaks may be indicative of light negative ions formed downstream the deflector flange which have been captured by the collector. These are not due to electron signals since the magnetic field of the suppression magnets located 5 mm from the Faraday cup is 250 G, which results to a Larmor radius of approximately 0.1 μm. The ion current corresponding to 10 GW/cm^2 is comparable to that of 20 GW/cm^2 indicating that, when the laser intensity is too high, the deflected ions would not be able to pass through the entrance aperture. At 10 and 20 GW/cm^2 laser intensities, there are detected signals even without deflection,

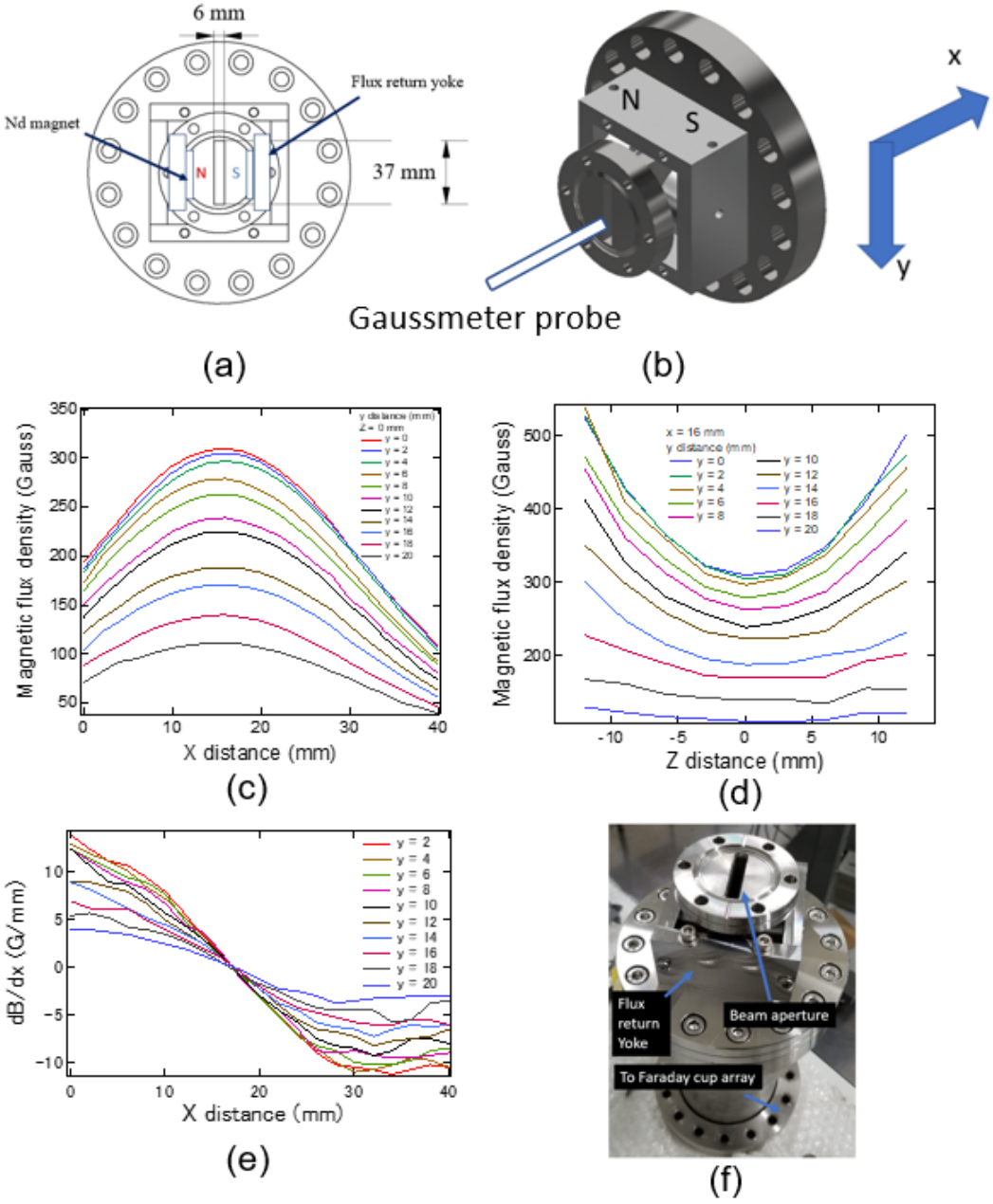

FIGURE 4.16: (a) Schematic of the magnetic momentum analyzer flange (b) Schematic for measuring magnetic field distribution (c) B-field distribution along the x and y directions (d) B-field distribution along the y-z directions (e) Derivative of the magnetic field dB/dx for each y direction (f) Image of the deflection flange

the beam divergence may be higher due to the higher laser input energy, in addition to the higher amount of ablated ions. Therefore, the deflector assembly may be utilized at a relatively low intensities, such as that of 5 GW/cm^2 when, under no deflection, small signal (up to approximately 5 μA) is desired.

4.2 Positive ion extraction

In this subsection, the ion energy as well as the effect of cavity formation on the ion signals are investigated. Figure 4.17 shows the schematic of the deflection experiment. A Q-switched Nd:YAG laser ($\lambda = 1064$ nm, pulse width = 5 nm) is incident towards the axis of a cylindrical graphite target (diameter = 10 mm, length = 7.5 mm) via a converging lens of 300 mm focal length as shown in Fig. 4.17. The laser is incident at 12° from the target axis. The laser forms a spot size of approximately 1 mm at the center of the target surface. The target is attached to a stainless steel shaft which is connected to a rotational motion feedthrough rotated by a DC motor. A grounded aluminum plate with 4 mm thickness and 8 mm aperture is placed 6 mm from the target surface. The produced laser plasma passes through an electrostatic lens, whose schematic is shown in Fig. 4.6. The lens system consists of three aluminum plates with 4 mm thickness and 8 mm aperture diameter along the axis. The plate distance is 2 mm apart with the center plate biased, while the other two are kept grounded. The deflected ion beam then passes towards a Faraday cup (FC) array equipped with a retarding potential analyzer (RPA). The Faraday cup array is located 560 mm from the target axis and consists of four Faraday cup labelled FC 1 to 4, where FC 1 is located at +19 mm, 0 mm, -19 mm, and -38 mm from the target axis, respectively. FC 1 collects the ions that are deflected against the magnetic field direction. Signals collected by FC 2 represent the current along the target axis. The positive and negative signs indicate directions against and towards that of the gravitational force, respectively. The Faraday cup array is enclosed in a grounded, stainless steel shield and neodymium permanent magnets are attached to the shield with approximately 250 G field intensity measured 5 mm from the array. The RPA consists of a 3 mm thick retardation plate and a 1 mm thick grounded plate with a separation distance of 2 mm between the plates. The aperture diameter of the bias plate is 5 mm to ensure homogeneous field at the entrance. Ion time-of-flight signals are collected from the Faraday cup terminals using a 500 MHz oscilloscope terminated by 50 Ω resistors. The Faraday cup FC 4 located at the bottommost part, whose aperture is not directed at the flight tube port. During repeated ablation, the laser is incident on the same spot at 5 GW/cm^2 laser intensity at 10 Hz repetition rate while the target is rotated at 30 revolutions per minute. Experiments are performed inside a stainless steel vacuum chamber at 5×10^{-6} Pa base pressure.

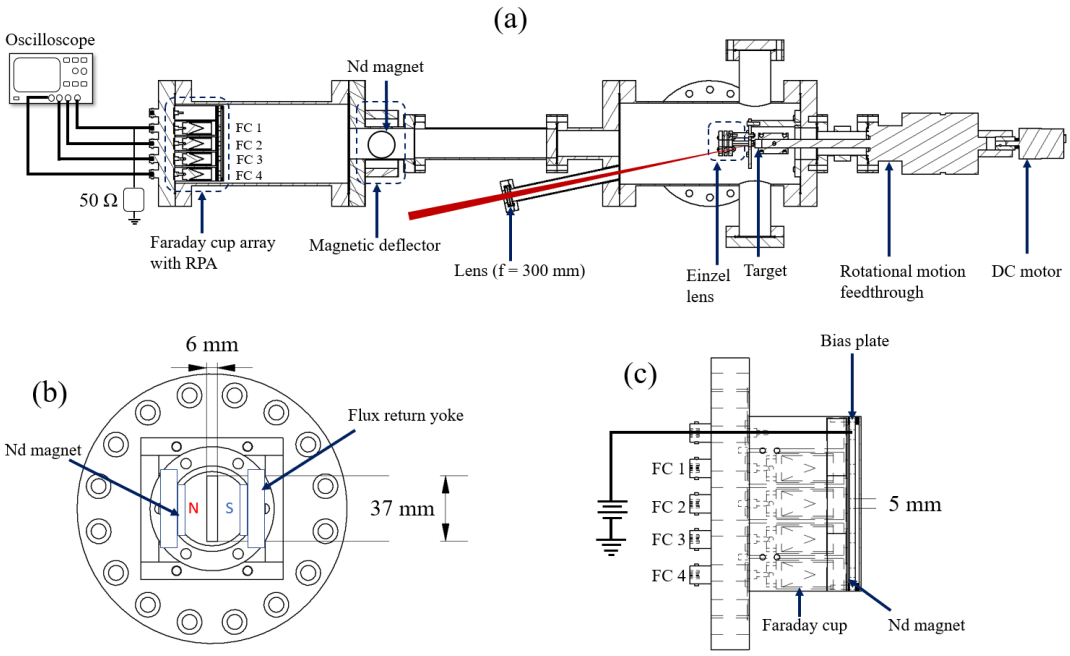

FIGURE 4.17: (a) Experimental setup for positive ion diagnostics using electrostatic lens, ion deflector flange, and retarding potential analyzer, (b) schematic of the deflection flange (c) schematic of the retarding potential analyzer

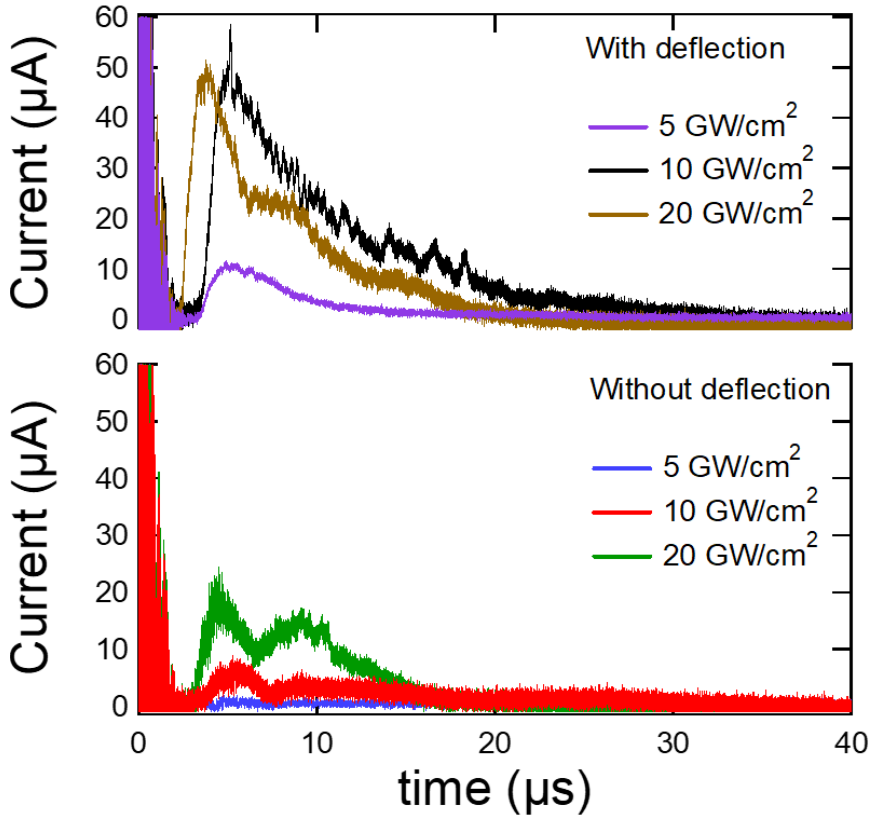

FIGURE 4.18: Ion time of flight signals collected by FC 4 for 5, 10, and 20 GW/cm^2 laser intensities with 560 G deflection, lens, extraction voltage = 0 V

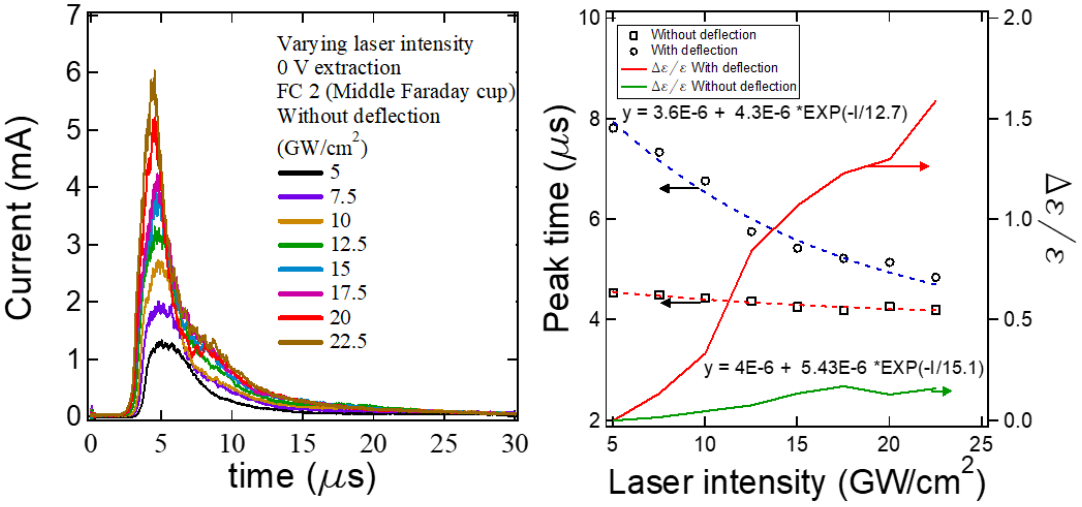

FIGURE 4.19: (a) Ion time of flight signals collected by FC2 (Middle Faraday cup) for increasing laser intensity (b) Peak time and energy change factor $\Delta\epsilon/\epsilon$ for varying laser intensity with and without 300 G magnetic deflection, dashed lines show exponential fits

Effect of laser intensity

Figure 4.19a shows the ion signals collected by the middle Faraday cup (FC 2) for varying laser intensity, where ion current increase as well as decrease in time-of-flight is observed. The energy gain due to the laser intensity can be estimated from the ion time of flight spectrum. Given initial and final kinetic energies ϵ and ϵ' corresponding to initial and final times-of-flight t and t', we have

$$\epsilon = \frac{1}{2}m\left(\frac{d}{t}\right)^2$$
$$\epsilon' = \frac{1}{2}m\left(\frac{d}{t'}\right)^2.$$

Let $\Delta\epsilon = \epsilon' - \epsilon$ be the kinetic energy change of the ion distribution. Given the same distance, we have

$$\Delta\epsilon = \epsilon\left(\frac{t^2}{t'^2} - 1\right). \tag{4.32}$$

Using the ion signal at 5 GW/cm^2 as the reference peak, the energy change can be calculated. The term $\Delta\epsilon/\epsilon$ determines the factor of energy change in the ions relative to the initial energy.

Figure 4.19b shows the peak time and energy change factor $\Delta\epsilon/\epsilon$ as functions of laser intensity, taken from the current signals collected by the middle Faraday cup. Increase in laser intensity lowers down ion time of

flight, where the rate of peak time decrease with magnetic deflection is higher than that However, increasing the intensity follows an exponential trend approaching 4μs. For the case without deflection, a slower decrease is observed, however, the peak time also approaches 4 μs. The increase in the rate of change of peak time versus laser intensity can be explained in the following. The force on an circularly accelerating ion with mass m due to the magnetic field is given by:

$$\frac{mv^2}{R} = q\mathbf{v} \times \mathbf{B}$$

Solving for v, and equating $v = d/t$ we have

$$\frac{d}{t} = \frac{qBR}{m} \tag{4.33}$$

Since $v = d/t = \sqrt{2\epsilon/m}$, we substitute this to v in Eq. 4.33. Solving for m,

$$m = \frac{qBRt}{d} \tag{4.34}$$

Plugging the above equation back to Eq. 4.33, and solving for $t = t(\epsilon)$ we have

$$t(\epsilon) = \frac{qBRd}{2\epsilon} \tag{4.35}$$

Taking $dt/d\epsilon$, we have

$$\frac{dt}{d\epsilon} = \frac{-qBRd}{(\epsilon^2)}. \tag{4.36}$$

Since if $dt = t' - t < 0$, then $d\epsilon = \epsilon' - \epsilon > 0$ and vice versa, the negative sign in the above equation vanishes. Therefore, the change in peak time increases with the application of the magnetic field. Ions encounter a force due to the magnetic field, for which changes in velocity due to the input energy would significantly affect the rate of energy increase during ion propagation.

Effect of extraction voltage

Figure 4.20 shows the ion signals for increasing extraction voltage. Increasing the extraction voltage decreases the ion current from 6.4 μs above 200 V extraction bias. From 400 V to 600 V extraction voltage, the ion signals from 7 μs and later times have decreased, resulting to a sharp ion peak at 5 μs. Above 600 V, the peak current decreased down to 5 μA at 800 V extraction voltage.

The decrease in ion current corresponding to lower energy ions (with TOF $\geq$ 8 μs) may be explained by the following. Since the method of extraction by biasing the target, electrons produced from the laser ablation plasma may return to the positively charged target and undergo collisions with the propagating positive ions. These collisions may result to recombination and slowing down of the ions which result to decrease in ion signal. Positive ions

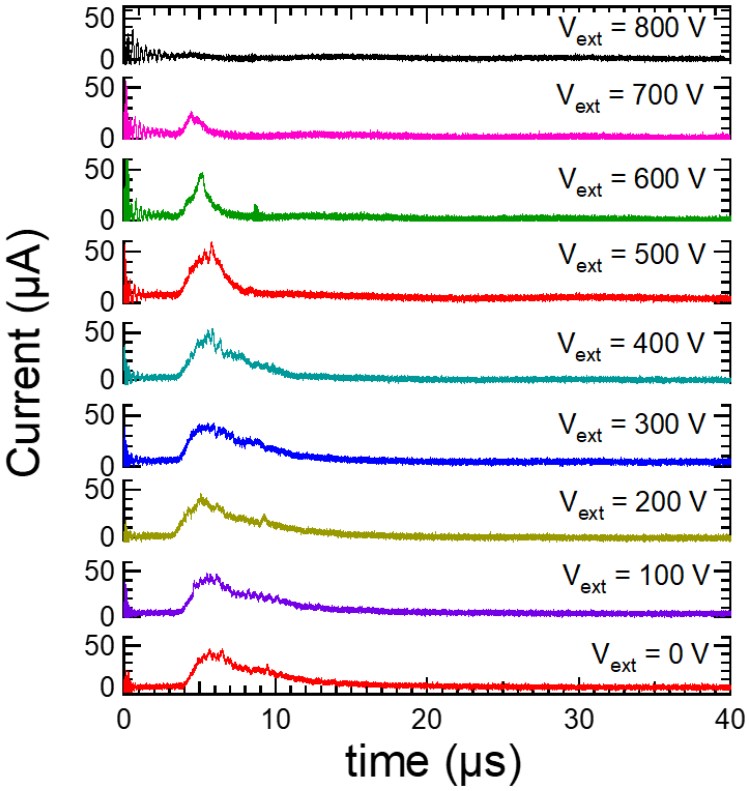

FIGURE 4.20: Time of flight signals collected by FC 4 for increasing extraction voltage

with a certain energy ϵ are able to travel through the flight tube. The width reduction of the velocity distribution may be explained by the reduction of the slower ions when they undergo collisions with the returning electrons.

Effect of lens voltage

Figure 4.21a shows the time-of-flight signals collected by FC 4, or the bottommost Faraday cup for varying lens bias voltage. When the lens bias is increased, the ion current decreased. Sharp peaks were also observed to vanish starting from 120 V lens voltage. Figure 4.21b shows the peak current intensity for increasing lens voltage. Up to 60 V lens bias, the peak current is around 40 to 53 μA. Increasing lens voltage results to significant decrease of the peak current at 80 V. Further increasing the lens voltage results to the slower ion current decrease down to between 10 and 20 μA.

Increasing the lens bias decreases the focal length of the ion beam, as shown in Fig. 4.5b. Further increasing the voltage indicates that the focal length is too short in which some of the ions diverge and thus fewer ions are collected. Those ions correspond to higher energies which underwent focusing at that voltage.

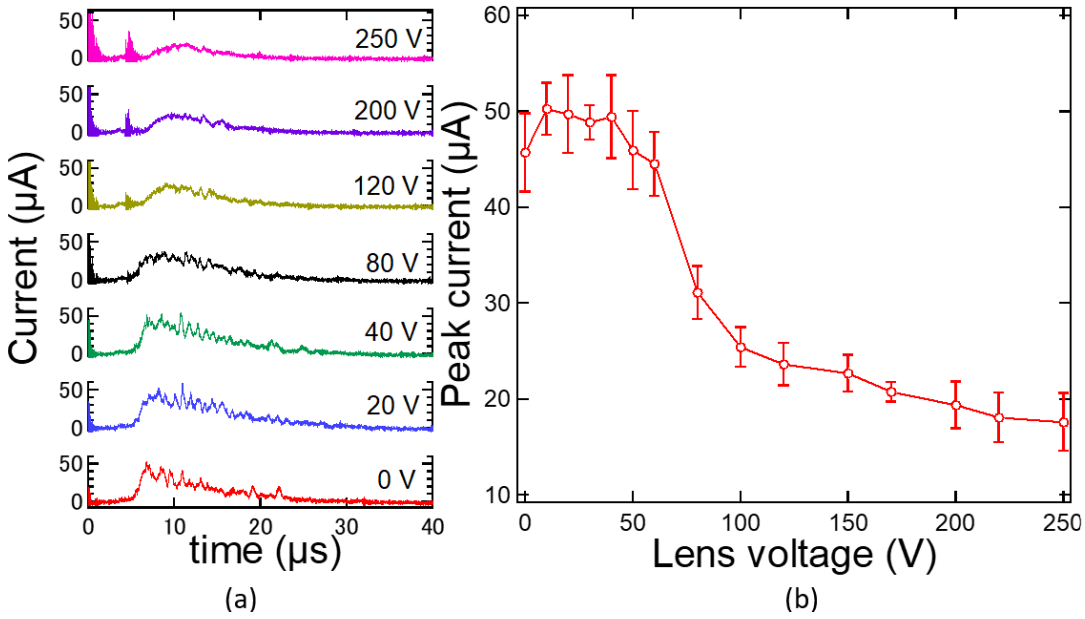

FIGURE 4.21: (a) Ion time of flight signals collected by FC 4 (bottommost Faraday cup) for varying lens voltage (b) Peak current for increasing lens voltage, laser intensity: 5 GW/cm^2

4.2.1 Retarding potential analysis of ion signals of a fresh target

In order to quantify the ion beam energy of the deflected plasma, retarding potential analysis is performed. Figure 4.22a shows the time-of-flight signals for varying RPA bias collected by FC 4. Ion current consists of a peak starting from 8 μs at 1 mA intensity. At 160 V bias, the 8 μs peak, representing the C_3^+ cluster ion peak is highest at 800 μA. Detectable signals lasted until 320 V bias. The charge collected from the TOF spectra is obtained by integrating the TOF current with respect to time. Figure 4.22b shows the charge obtained for increasing RPA voltage. Above 160 V RPA voltage, the charge obtained significantly decreased by around one order of magnitude at 30 μs.

Increasing the retarding potential bias results to the increase in the energy threshold in which ions are permitted to be collected. From Fig 4.22a, high energy ions remain when the RPA bias is increased from 160 to 240 V. The ion distribution then should have an average energy between these values. Moreover, the width of the ion signal at 160 V is observed to become sharper compared to that corresponding to lower voltages. One reason is the separation between high and low energy ion distributions consisting the ion signal. When the ion current of the lower energy ion decreases, only the higher energy ion current distribution remains. Further increasing the voltage above 160 V only decreases the current amplitude without further decreasing the width, which may be due to the maximum energy of the ions being reached at these voltages. This is observed in the TOF at 240 V RPA bias, as there is approximately 20 μA current detected, but the width did not decrease significantly.

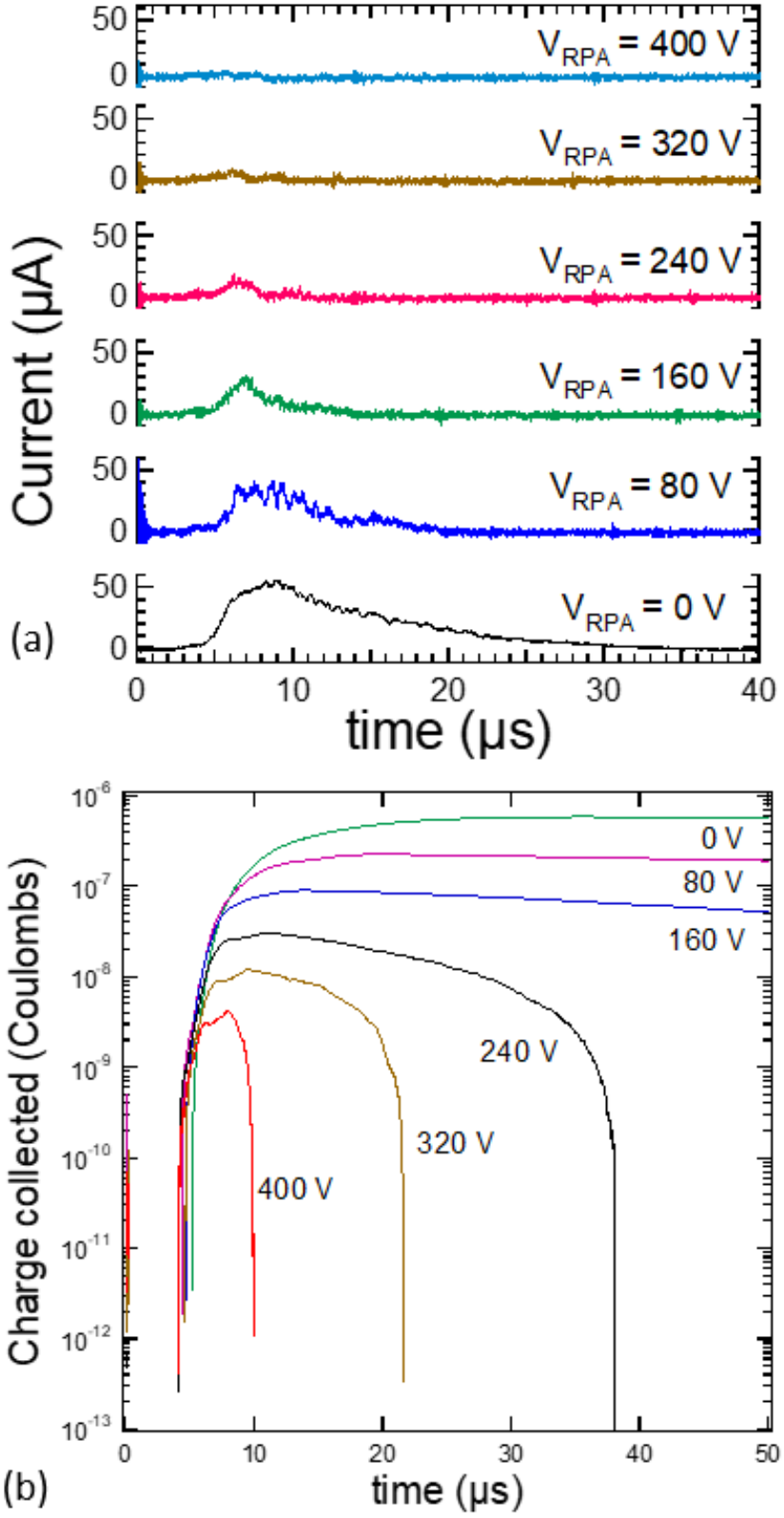

FIGURE 4.22: (a) Ion time of flight signals collected by CH 4 (bottommost Faraday cup) for varying retarding potential bias (b) Charge collected for increasing retarding potential bias, laser intensity: 5 GW/cm^2

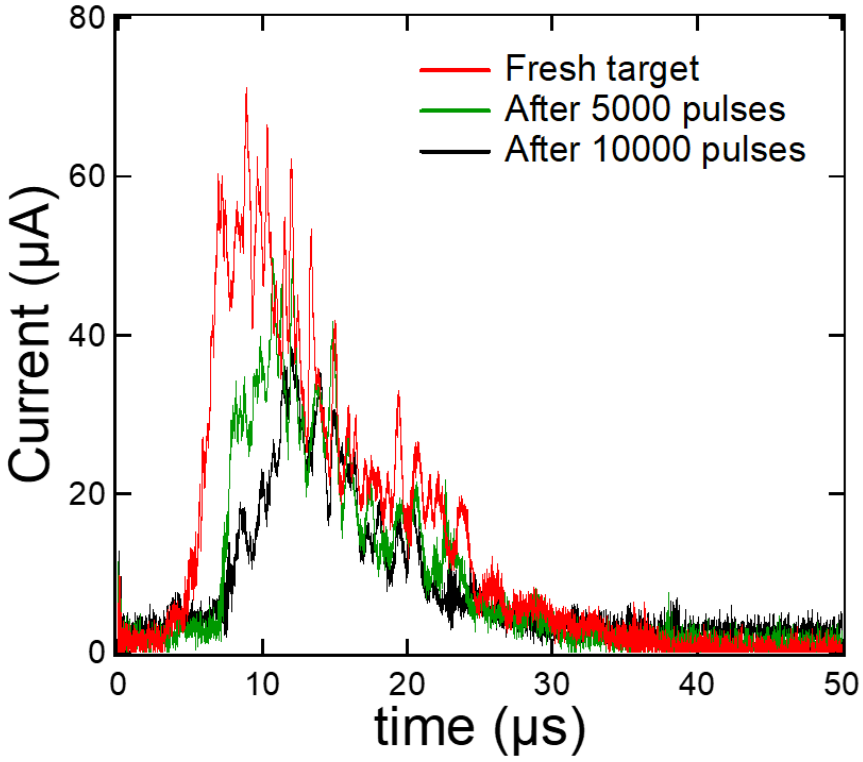

FIGURE 4.23: Ion time of flight signals for increasing number of pulses, laser intensity: 5 GW/cm^2

4.2.2 Effect of number of pulses

Figure 4.23 shows the time-of-flight signals after repeated ablation at 5 GW/cm^2 laser intensity. After repeated ablation, the current signals shift to later times. Considering the C_3 ion peak at 7.1 μs TOF, a 1.6 μs shift towards later time is observed after 5000 pulses while the shift is 2.5 μs after 10000 shots. Ion current intensity decrease is also observed, where the current intensity is approximately half of that the fresh target after 10000 pulses. The peak current of the ion distribution is plotted versus the retarding potential bias shown in Fig. 4.24a. Peak current after 30000 pulses reduced to 20 percent from the fresh target condition. After subsequent shots, reduction in ion energy is observed, which is indicated by the value for which the peak current rapidly decreased as the retarding potential is increased. Fig. 4.24 shows the ion energy dependence on the number of laser shots. For the fresh target condition, the ion energy is measured between 220 and 290 eV. Significant ion energy decrease is observed for the first 12000 pulses, which remained at approximately 100 eV for subsequent pulses.

In order to investigate the energy gain after the formation of target cavity, varying laser intensities were incident on the target. Fig. 4.25 shows the normalized peak current for varying retarding potential bias at varying laser intensity after 30000 pulses. Relative to the peak current at 5 GW/cm^2 laser intensity at 0 V retarding plate bias, the peak current increase is 2.7, 5, and 6 times for 10, 15, and 20 GW/cm^2 laser intensity, respectively. Increase in laser intensity resulting to increased ion current amplitude. A threshold V_{th}

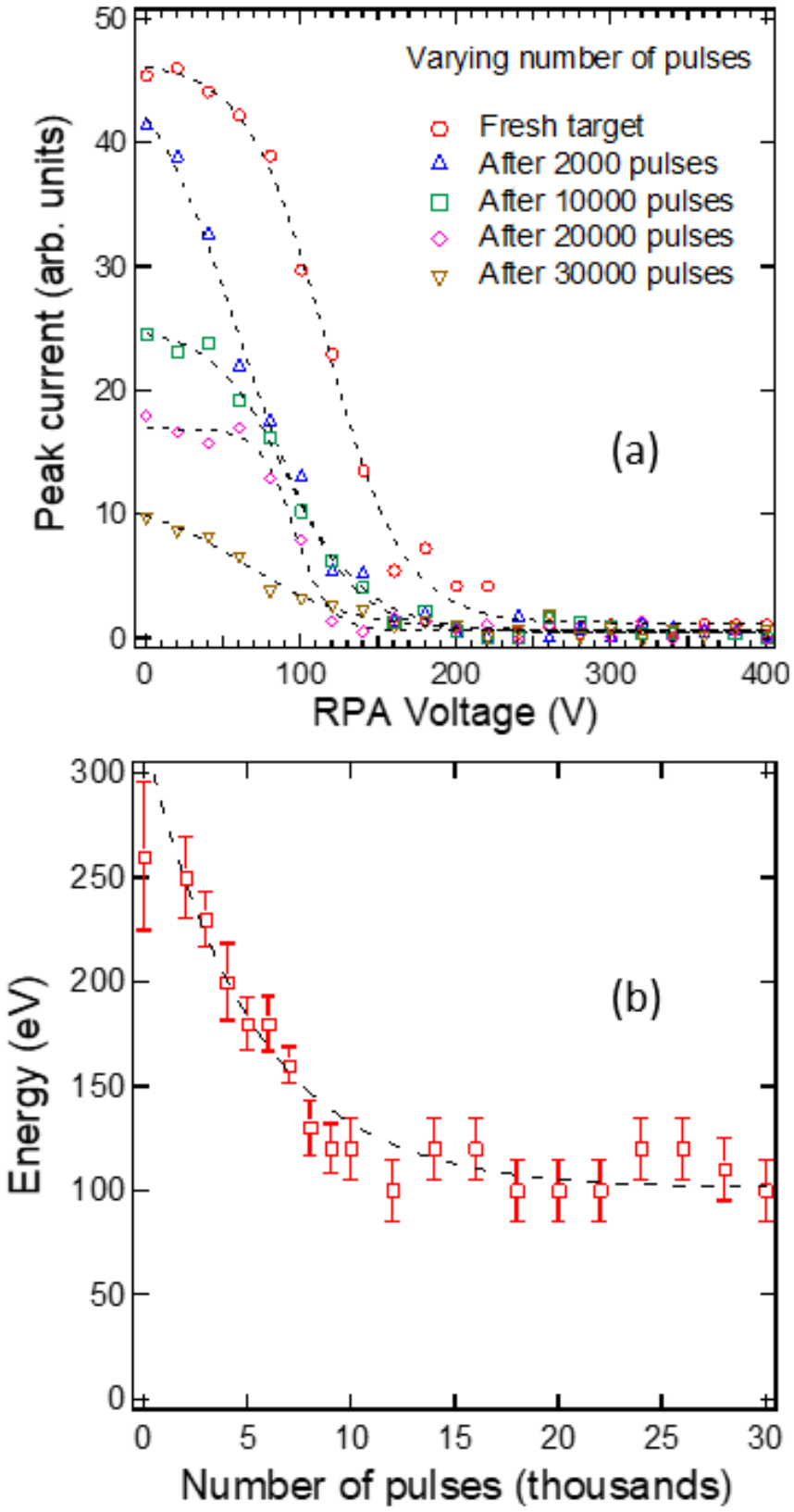

FIGURE 4.24: (a) Peak current versus retarding potential analyzer bias for increasing number of pulses (b) Estimated ion energy for increasing number of pulses

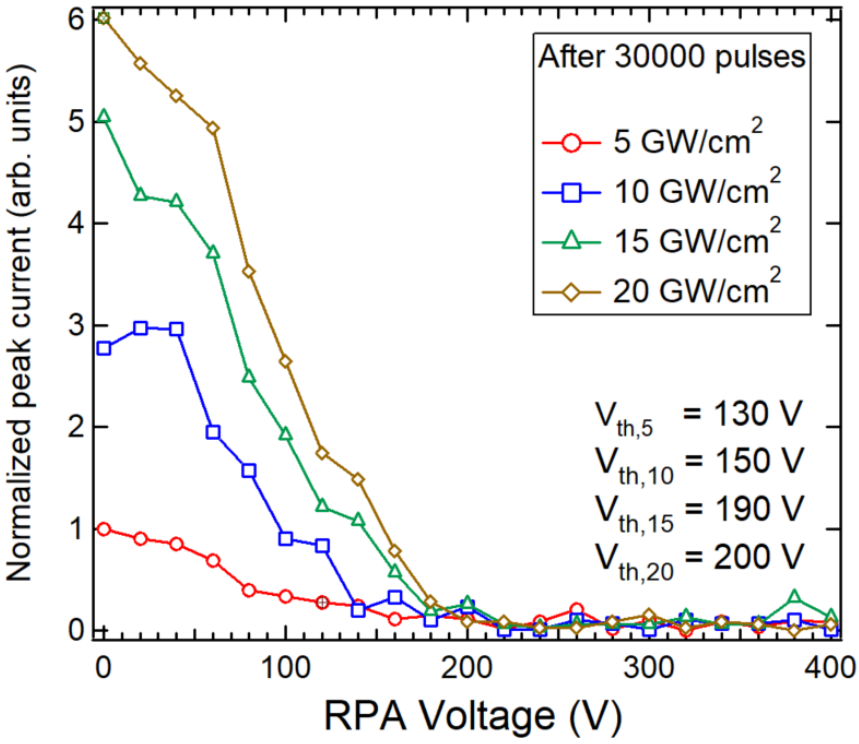

FIGURE 4.25: Peak ion current for varying retarding potential bias at increasing laser intensity after 30000 pulses, V_{th} represents the voltage at which the current is reduced to zero

is defined as the voltage at which the peak current falls to zero, or when there are almost no charge collected for increasing RPA voltage. Increase in laser intensity to 20 GW/cm^2 increases V_{th} of the ion current by 70 V relative to the peak current at 5 GW/cm^2 laser intensity.

4.3 Discussion on positive ion production

When a plasma is produced by the laser, electrons, ions, and neutrals from the plasma are produced just above the target surface at a microsecond order. In a freely expanding plasma without the cavity, these constituents would undergo inelastic collisions, which results to ions having an overall velocity distribution as they propagate downstream. Increasing the ion energy by increasing the extraction voltage results to increase in velocity. The trajectory of these high energy ions would be deflected past the collector, thus showing the decrease in the current signal of the FC 4 as shown in Fig. 4.22. In terms of focusing, ion current is at its highest below 100 V shown in Fig. 4.21, which shows that the lens voltage has a significant contribution in decreasing the ion beam focal length when the lens bias is increased. Comparing the shape of this graph to the retarding potential analysis graph in Fig. 4.22, there exists a threshold both in ion focusing and ion energy analysis. For ion focusing, this threshold is at 80 V, while for the RPA, the threshold is around 250 V for the fresh target, from which the ratio between lens voltage

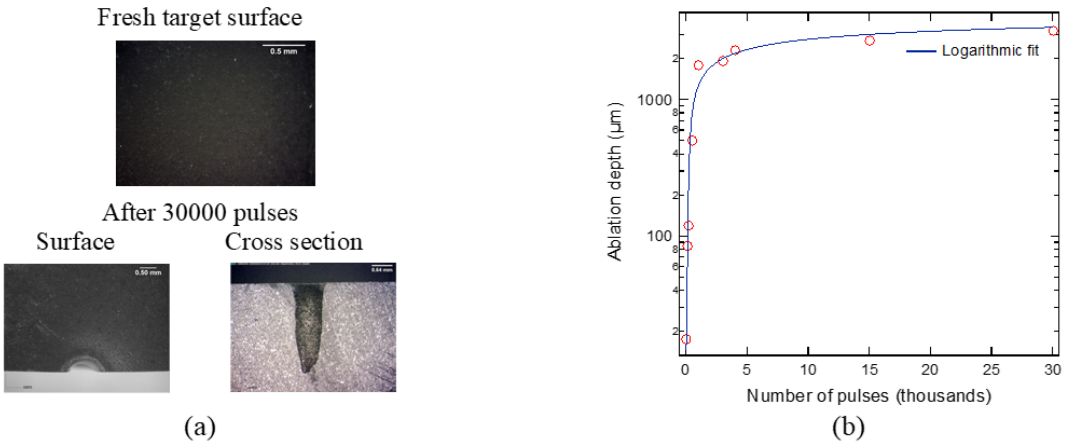

FIGURE 4.26: (a) Images of target surface for fresh and after 30000 pulses ablation (b) Ablation depth for varying number of pulses at 5 GW/cm^2 drilling pulse

and RPA voltage is approximately 0.3. This ratio is close to that obtained from the trajectory simulation in Fig. 4.13, where the 0.25 ratio between lens voltage and RPA voltage shows ion focusing on the leftmost (bottommost in experiments) Faraday cup. The values of the two thresholds are not equal, since the ion signals comprise of energy and mass distributions. Ions of equal mass but different energies traverse different focal lengths. Meanwhile, ions with equal energies but different mass may be deflected at different radii.

In the presence of a cavity, the motion of the constituents become restricted as the plasma is initiated within the hole. Figure 4.26a shows the surface and cross section images of the target surface after 30000 pulses ablation. The ablated target consists of a 2 mm depth cavity with a 1 mm diameter hole. Figure 4.26b shows the ablation depth for varying number of pulses. Increasing the number of pulses results to a logarithmic dependence on the ablation depth where the depth saturation starts from 5000 pulses.

At the time of plasma initiation on the surface, the time duration the formed constituents spend within the cavity facilitates higher probability of interaction not only within the constituents but also with the inner cavity formed by repeated laser ablation. Due to these interactions, ion energy losses occur, which is reflected by shifts in TOF spectra towards later times after repeated number of pulses, as shown in Fig. 4.23. Increasing the number of pulses effectively cools down the ions and slows down their propagation due to the inelastic collisions inside the cavity. This 'cooling down' is interpreted as a reduction in ion energy rather than the reduction in the vaporized plume temperature. As the plasma cools down, some ions are prevented to propagate outside the hole, thereby decreasing the ion current. The energy loss is measured in Fig. 4.24, which shows a limit which approaches 100 eV, starting from 8000 pulses. This threshold is due to the reduction in the ablation rate for increasing number of pulses [18]. When the laser is initiated from the cavity, the plasma acts as a barrier which absorbs further incoming laser energy incident on the target [19]. The decrease in the rate of current increase for increasing laser intensity is

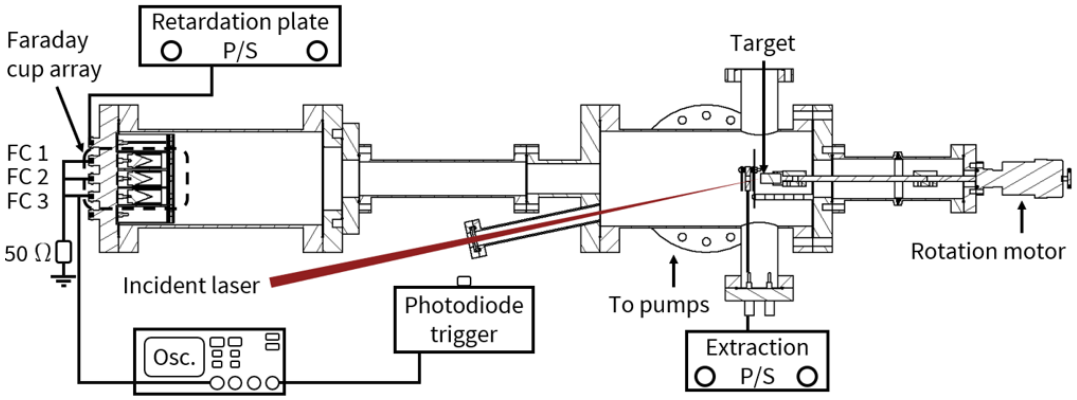

FIGURE 4.27: Experimental schematic for negative ion detection

shown in 4.25, where increase in laser intensity resulting to increased peak current leading to increased energy for ablation. Under cavity confinement, the volume at which the plasma is formed is reduced, thus leading to the further absorption of laser energy. When the laser intensity is increased to 20 GW/cm^2, the resulting energy is equivalent to that of the fresh target. This shows the effect of the cavity in reducing the energy of the ions, as a higher intensity laser is required to match the energy of the free expansion condition.

4.4 Negative ion production

In the detection of negative ions, the ion beam is extracted with a negative potential. Figure 4.27 shows the experimental setup for negative ion detection. In this experiment, the focus is towards the detection of ions along the axis, since negative ions are assumed to be heavy ions. The laser (λ = 1064 nm, pulse width = 5 ns, repetition rate 10 Hz, laser intensity 5 GW/cm^2) is incident on a graphite surface and is extracted using a high voltage power supply. The laser intensity by tuning the amplifier delay from the optical pumping. An extraction electrode with a 5 mm aperture is placed 9 mm from the target surface. Ions are collected by the Faraday cup array, where the FC 2 is labelled as the Faraday cup along the target axis. The Faraday cup array is contained with a stainless steel shield. In order to ensure electron suppression, permanent filter magnets of 300 G flux density were attached to the Faraday cup array shield. The retarding potential analyzer is attached to the Faraday cup array. The signals are collected by an oscilloscope connected to a 50 Ω termination resistor.

From the ion time of flight signals, the charge yield is obtained by integrating the ion current with respect to time. Figure 4.28 shows the charge yield obtained for increasing number of pulses. As in the case of Fig. 4.23, the ion current decreased for increasing number of pulses. The significant decrease is observed from 5000 pulses, followed by a lower rate of charge

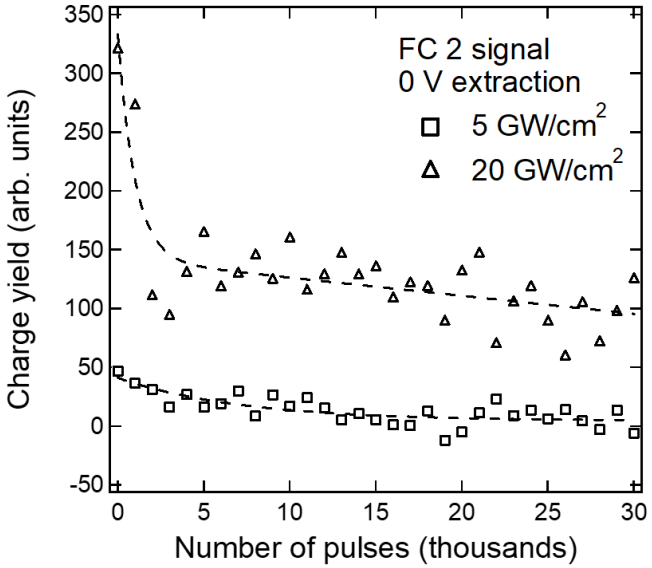

FIGURE 4.28: Charge yield for increasing number of pulses

yield decrease. Increase in charge yield is observed for 20 GW/cm^2 laser intensity.

Biasing the retardation plate enables the negative ion detection located above the main carbon peak located at 5 μs. Figure 4.29 shows the ion signals for increasing retarding potential analyzer voltages collected by the FC 2, or the Faraday cup along the target axis. The main peak corresponds to C_3^+ ion peak. Broad peak distributions are observed from 25 to 28 3μs TOF from 500 to 600 V bias. The onset of emergence of negative peaks occur when the bias is above 100 V. Time of flight signals corresponding to 20 GW/cm^2 laser intensity showed distinct peaks at 30 μs, which could be due to the increased collisions provided by increased laser ablation as the intensity is increased. Distinct peaks ranging from 29 to 33 μs with a sharp peak at 31 μs at 600 V retarding potential were observed for increasing retardation plate bias, which corresponds to masses of approximately 1440 amu. Figure 4.30 shows the time-of-flight signals after 30000 pulses for varying RPA voltages at -3 kV extraction voltage. Decrease in the 5 μs positive peak is observed as the cavity is formed with no detection of sharp negative ion peak. Broad negative distributions were observed from 400 to 600 V retarding potential voltage are detected 25 to 32 μs with the highest negative peak observed at 27 μs.

Ion signals for varying number of pulses at -3 kV extraction at 400 V retarding potential analyzer bias is shown at the left of figure 4.31. Following the main positive ion peak, broad negative signal are observed from after 10μs time-of-flight. From a sharp peak at 30 μs peak in the fresh target condition, distinct ion peaks are shown from fresh to 20000 pulses ablation, with a formation of double peak at 24 and 28 μs shown after 20000 pulses corresponding to C_{26}^- and C_{35}^- ions respectively.

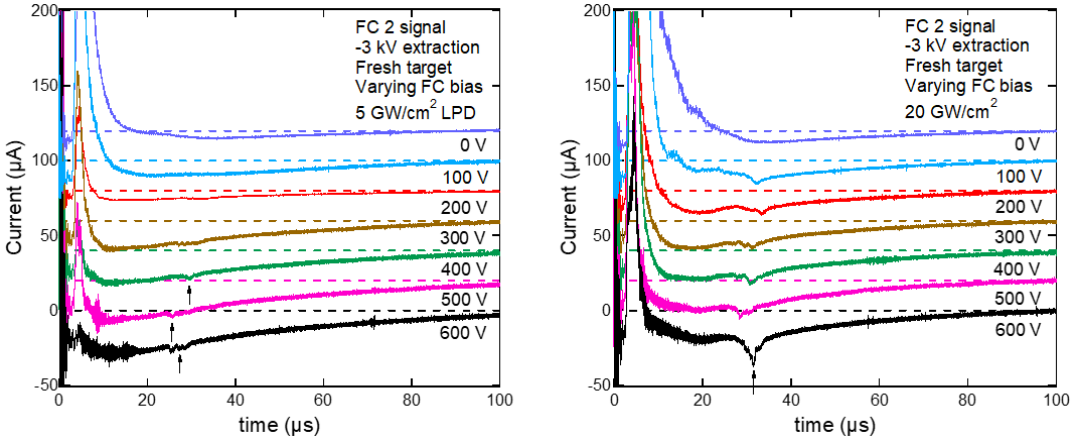

FIGURE 4.29: Ion time of flight signals collected by FC 2 (middle Faraday cup) for varying retarding potential analyzer voltage for a fresh target (left) laser intensity: 5 GW/cm^2 (right) laser intensity: 20 GW/cm^2

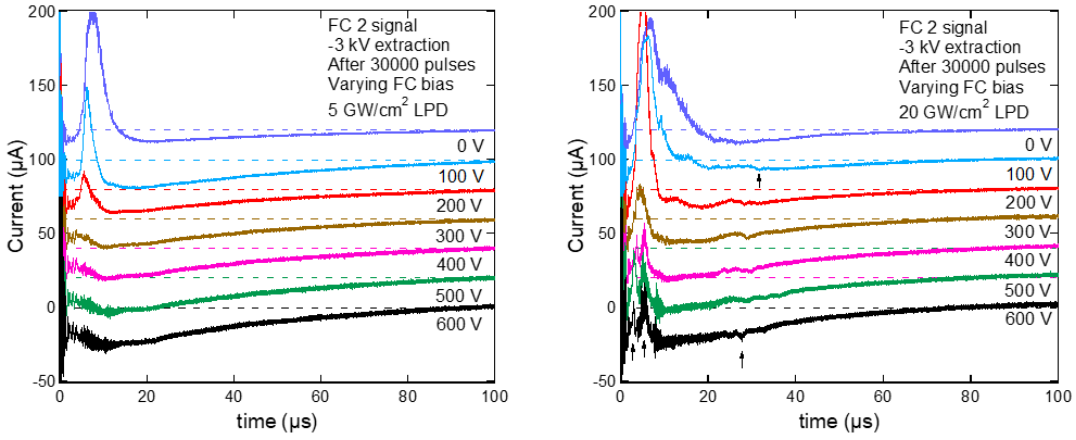

FIGURE 4.30: Ion time of flight signals collected by FC 2 (middle Faraday cup) for varying retarding potential analyzer voltage after 30000 pulses (left) laser intensity: 5 GW/cm^2 (right) laser intensity: 20 GW/cm^2

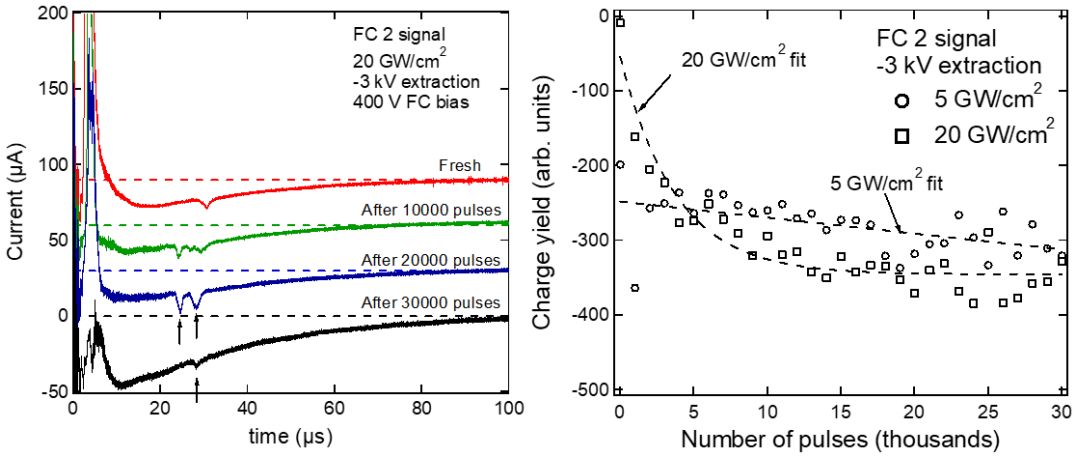

FIGURE 4.31: (Left) Ion time of flight signals collected by FC 2 (middle Faraday cup) for varying number of pulses at 400 analyzer bias voltage at 20 GW/cm^2 laser intensity (right) Charge yield for 5 and 20 GW/cm^2 laser intensity for varying number of pulses, dashed lines indicate line fits

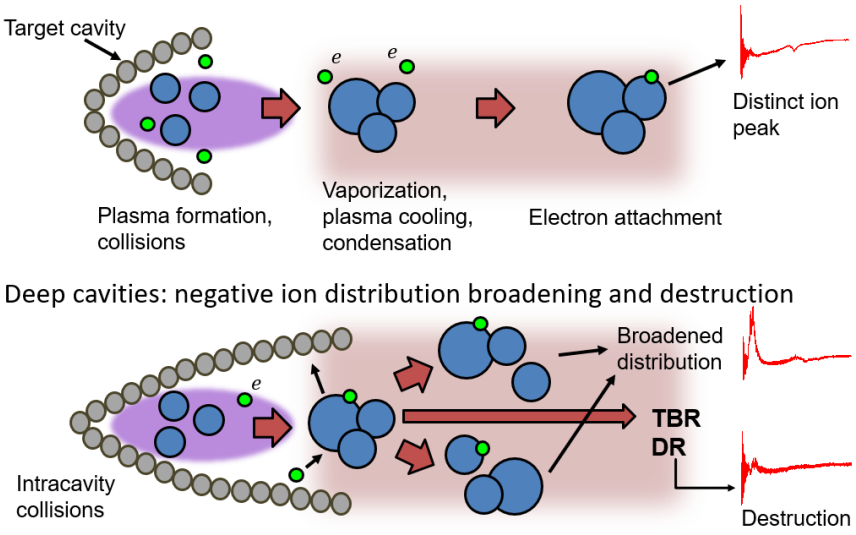

FIGURE 4.32: Mechanisms involved in negative ion production under the influence of cavity formation

4.5 Discussion on negative ion production

As with the formation of positive ions, the formation of negative ions are significantly influenced by collision induced processes. During free expansion, electrons, ions, and neutrals are formed near the target surface and propagate in the direction of the target normal. Plasma initiation within the cavity causes a shift in the ion peaks toward later times. At high enough extraction voltage, negative ions may also be extracted. The kinetic energy change ΔKE from with and without the cavity is calculated by:

$$\Delta KE = \frac{1}{2}m\left[\left(\frac{d+h}{t_{30000}}\right)^2 - \left(\frac{d+h}{t_{fresh}}\right)\right] \tag{4.37}$$

where m is the mass of C_3^+ ion, d is the flight distance form the target surface, and h is the ablation depth. With a depth of 3 mm, ΔKE is approximately -2 keV, or approximately 40 eV per nucleon. If the ion is a carbon single positive, the energy loss would be approximately 160 eV per nucleon, which is comparable to the energy loss for increasing number of pulses shown in Fig. 4.23 measured by the retarding potential analyzer. Escape of ions are impeded due to the formation of the cavity and ions lose kinetic energy. In describing the vaporized plume, it is assumed that the plume follows a 1-D Maxwellian distribution [20]. The surface vapor velocity $v_{vap,s}$ at a surface temperature T_s may be approximated by:

$$v_{vap,s} = \sqrt{\frac{2kT_s}{\pi m}} \tag{4.38}$$

where k is the Boltzmann constant. For $T_s = 15000K$ at 5 GW/cm^2 laser intensity, the corresponding vapor velocity and propagation time through the 3 mm cavity are 1.4 km/s and 2 μs, respectively [21]. The time duration for nanosecond pulse incidence, formation of plasma plume, graphite target vaporization, laser-induced surface temperature increase was reported to be within 50 ns [21]. Since the decrease of ablation rate can be interpreted as the onset of vapor cooling, the propagation time of the vapor inside the cavity consists of the entire process of plume initiation, propagation, and collision-induced cooling by the cavity.

In describing the role of the cavity negative ion formation, one of the main mechanisms for negative ion production in laser plasmas is collision induced electron attachment which is given by:

$$A^0 + 2e^- \rightarrow A^- + e^-. \tag{4.39}$$

With the plasma plume constricted in the cavity, the mean free path of the plume constituents decreases with the propagation volume thus increasing the probability for electron attachment to neutral atoms. The cavity wall contributes to the above mechanism and is suggested to undergo a three-body recombination (TBR) process, as a neutral component M representing the cavity wall, assuming elastic collisions of electrons with the cavity:

$$A^0 + 2e^- + M \rightarrow A^- + e^- + M \tag{4.40}$$

Assuming the vapor temperature of $T_S = 25000K$ at 20 GW/cm^2, the corresponding energy is 2.15 eV, which is less than the graphite work function of 4 eV. Therefore, no additional electrons are formed in the collision of the plume to the cavity walls. From Fig. 4.30, the formation of the cavity also induces negative ion destruction, due to the transition from sharp negative peaks for a fresh target towards broad ion distributions after 30000 pulses. For a large carbon cluster negative ion AB^- interacting with the neutral cavity wall M, the mechanisms involved in negative ion destruction are electron detachment and dissociative attachment and are respectively given by [11, 22]:

$$AB^- + e^- + M \rightarrow AB^0 + 2e^- + M \tag{4.41}$$

$$AB^- + e^- + M \rightarrow A^- + B^0 + 2e^- + M \tag{4.42}$$

Comparing the negative ion peak distributions between the ion signals at 20000 and 30000 pulses, the C_{26}^- and C_{35}^- ion peaks after 20000 pulses is more distinct than that of 30000 pulses. This suggests that the cavity formation reaches a depth at which the negative ion formation process is preferred. After which, the negative ion destruction mechanisms become more significant, thus resulting to a broader negative ion distribution. Accurate determination of the dissociation energies of these large negative ions are difficult to obtain as both formation and destruction processes occur inside the hole. Charge yield results from Fig. 4.28 shows the increased negative ion yield for increasing number of pulses, which indicates that negative ion processes occur for increasing pulses. At lower laser intensities, distinct negative ion peaks after 30000 pulses were not observed. This indicates that a greater initial ion energy is required in order to extract the negative ions from the hole.

4.6 Summary

This chapter involved experiments and analysis on positive and negative ion formation. Discussions on the possible mechanisms of ion formation, and destruction, and influence of the cavity were also performed. Experiments involved the design of a magnetic deflector system aiming to steer ion trajectories for mass analysis. From the retarding potential analyses, the ion beam produced by the laser is estimated to be 250 eV, whose energy increase is determined by $\Delta\epsilon/\epsilon$. Ion species consist of C_2^+ and C_3^+ positive ions, and C_{26}^- and C_{35}^- negative ions. An electrostatic lens is also developed to perform ion focusing, where a lens-to-ion retarding potential ratio of approximately 0.3 was found to maximize ion focusing.

Energy losses due to the cavity are also evaluated by retarding potential analysis for positive ions as well as energy difference for negative ions,

where a 150 eV energy difference was found from fresh target to after 30000 pulses ablation for RPA analysis. Negative ion charge yield suggested collision-induced mechanisms such as electron detachment and dissociative attachment are involved in the destruction of negative ions.

References

[1] A. Yamaguchi, K. Sako, K. Sato, N. Hayashizaki and T. Hattori, Rev. Sci. Instrum 32 02B921 (2014).

[2] T. Ikegami, S. Ishibashi, Y. Yamagata, and K. Ebihara, J. of Vac. Sci. Technol. A 19, 1304 (2001).

[3] W. R.Creasy and J.T.Brenna, Chem. Phys. **123** 2-3 453-468 (1988).

[4] X. Kong, S. Li, S. Zhang, Y. Huang, Y. Cheng, J. Am. Soc. Mass Spectrom. **22** 11 (2011).

[5] X. Kong, Y. Huang, Y. Chen, J. Mass Spectrom. **47** 4 523-528 (2012).

[6] M. Lenner, A. Kaplan, Ch. Huchon, and R. E. Palmer, Phys. Rev. B **79** 184105 (2009).

[7] R. Casaes, R. Provençal, J.Paul, and R. J. Saykally, J. Chem. Phys. **116** 6640 (2002).

[8] F.Kokai, Y.Koga, and R.B. Heimann, Appl. Surf. Sci. **96-98**, 261-266 (1996).

[9] M. S. Tillack, D. W. Blair and S. S. Harilal, Nanotechnology **15** 390–403 (2004).

[10] L. Hanley and S. Anderson J. Phys. Chem. **91**, 5161-5163 (1987).

[11] S. S. Alimpiev, M.E. Belov, V.V. Mlinsky, S.M. Nikiforov, V.I. Romanjuk, C. D. Smith, and E. F. Jones, Appl. Phys. A 58, 67-72 (1994).

[12] A. A. Tuinman, A. S. Lahamer, and R. N. Compton, Int. J. Mass. Spec. **205**, 309-323 (2001).

[13] T. Moriwaki, H. Shiromaru, Y. Achiba, Z. Phys. D 37, 169-174 (1996).

[14] X. Wang, S. Zhang, X. Cheng, E. Zhu, W. Hang, B. Huang, Spectrochim. Acta B **99** 101–114 (2014).

[15] L. Torrisi, S. Gammino, L. Andò, L. Laska, J. Appl. Phys. **91** 4685–4692 (2002).

[16] M. Szilagyi, *Electron and Ion Optics*, Plenum Press, 1988.

[17] P. Dahl, *Introduction to Electron and Ion Optics*, Academic Press, 1973.

[18] A. E. Wynne and B. C. Stewart, Appl. Phys. A, **76**, 373–378, (2003).

[19] N. A. Vasantgadkar, U. V. Bhandarkar, and S. S. Joshi, Thin Solid Films 519 1421-1430 (2010).

[20] A. Bogaerts, Z. Chen, R. Gijbels, A. Vertes, Spectrochim. Acta B 58 1867–1893 (2003).

[21] S. Sinha, J. Laser Appl. 30, 012008 (2018).

[22] E. Stoffels, W. W. Stoffels, and G. M. W. Kroesen, Plasma Sources Sci. Technol. 10, 311-317 (2001).

Chapter 5

Optical spectroscopy of confined laser produced plasmas

5.1 Introduction

Laser plasmas have received a lot of attention due to the production of electrons and ions within the laser pulse. Within the plasma burst and afterglow, interactions within the plasma constituents pose significant interest. One of the methods in characterizing the radiation within the plasma is via optical emission spectroscopy (OES). In OES, light from the plasma is incident on a spectrometer or spectrometer array which converts the light into a band of wavelengths. A typical output of this spectra is the wavelength-resolved emission intensity, which qualitatively reflects the amount of ions and excited atoms which have recombined. One well-known applications of optical spectroscopy of laser ablation plumes is laser-induced breakdown spectroscopy, or LIBS. In LIBS, a fast spectrometer, typically with spectrometer gate delays of nano to microsecond order, is utilized to identify the evolution of the emission spectra [1, 2]. With the laser pulse producing singly and multiply charged ions, the ion characteristics of the (typically solid) sample can be obtained in a single shot though the emission lines of produced ions. Applications of laser plasma spectroscopy range from space exploration [3, 4, 5] to forensic analysis [6, 7]. For the case of extraterrestrial exploration, optical spectroscopy of laser produced plasmas are employed in the observation of Martian soils, where carbon is one of the main components [8].

When the laser ablates the solid, the initial phase involves electron production, followed by ion production via electron ionization. In plasma spectroscopy, an important assumption is considered, that is, when the electrons and ions are in thermal equilibrium. In this case, the plasma constituents exhibit a common temperature, which is approximated from the spectral intensity. Thermal equilibrium assumes the Maxwellian distribution of ions and electrons in the plasma, which is dependent on the electron and ion density. Once the ions reach a certain density called the McWhirter criterion, the plasma is stated to be at a local thermal equilibrium (LTE) [9, 10]. The case of LTE states that the probability of inelastic collisions with electrons leading to bound states higher than an energy level is higher than radiative decay to that energy level [11]. This significantly differs

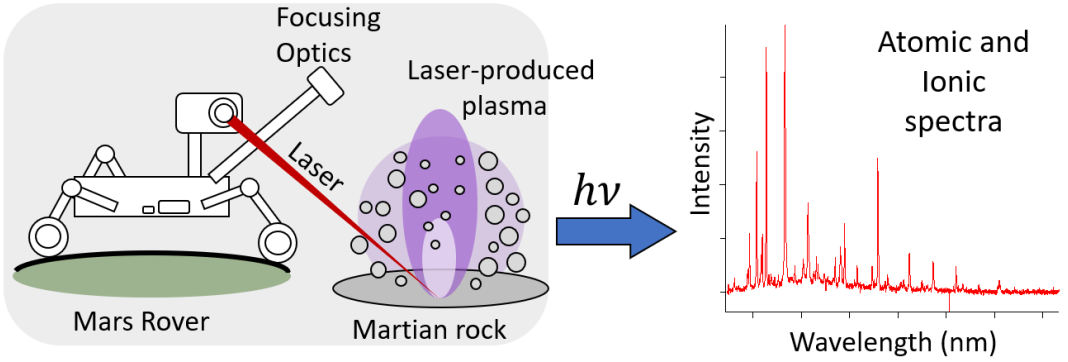

FIGURE 5.1: Diagram showing an application of LIBS for space applications

with the case of the laser plasma, since this type is transient as well as nonhomogenous as electron induced excitation dominates over radiative decay. In order to characterize whether the plasma is in LTE, the difference between an ionizing character and recombining character needs to be identified, where the *deviations* from the LTE can be determined. Thus, not only that the electron density, ionization and recombination rates (via Boltzmann and Saha equations) must also be considered to provide a more accurate description whether the plasma is in LTE [11]. Especially in the initial stages of plasma formation, the plasma is in the nonequilibrium state since simultaneous ablation, electron ionization, and laser absorption occur.

From the above requirements in labelling the laser plasmas as a system under LTE, such condition is not assumed in this work. The focus in this work involves the direct investigation on the effect of the target cavity on the laser plasma. From the previous chapter, ion current decrease is observed as the cavity is being formed. The ions collected by time-of-flight are represented by only those which have escaped the cavity. This shows a limitation of time-of-flight analysis in characterizing cavity confined plasmas. On the other hand, optical diagnostics enable the characterization of laser plasmas at any angle with respect to the target surface, thus offering versatility compared to the charge collection method. However, a limitation is that from the intensity, the mass of the excited atom cannot be deduced, since there are no known spectral emission lines corresponding to the heavy cluster ions. From the design of the laser ion source which includes a shallow angle incidence, emission spectra in two directions: parallel and perpendicular to the cylindrical target axis, corresponding to the regions inside and outside the cavity are investigated.

5.2 Experiment schematic

Figure 5.2(a) shows the experimental setup for the collection of emission spectra [12]. A nanosecond Q-switched Nd:YAG laser (pulse width = 5 ns, λ = 1064 nm) is incident 12 degrees from the axis of a cylindrical graphite pellet target using a converging lens (focal length = 300 mm). The target

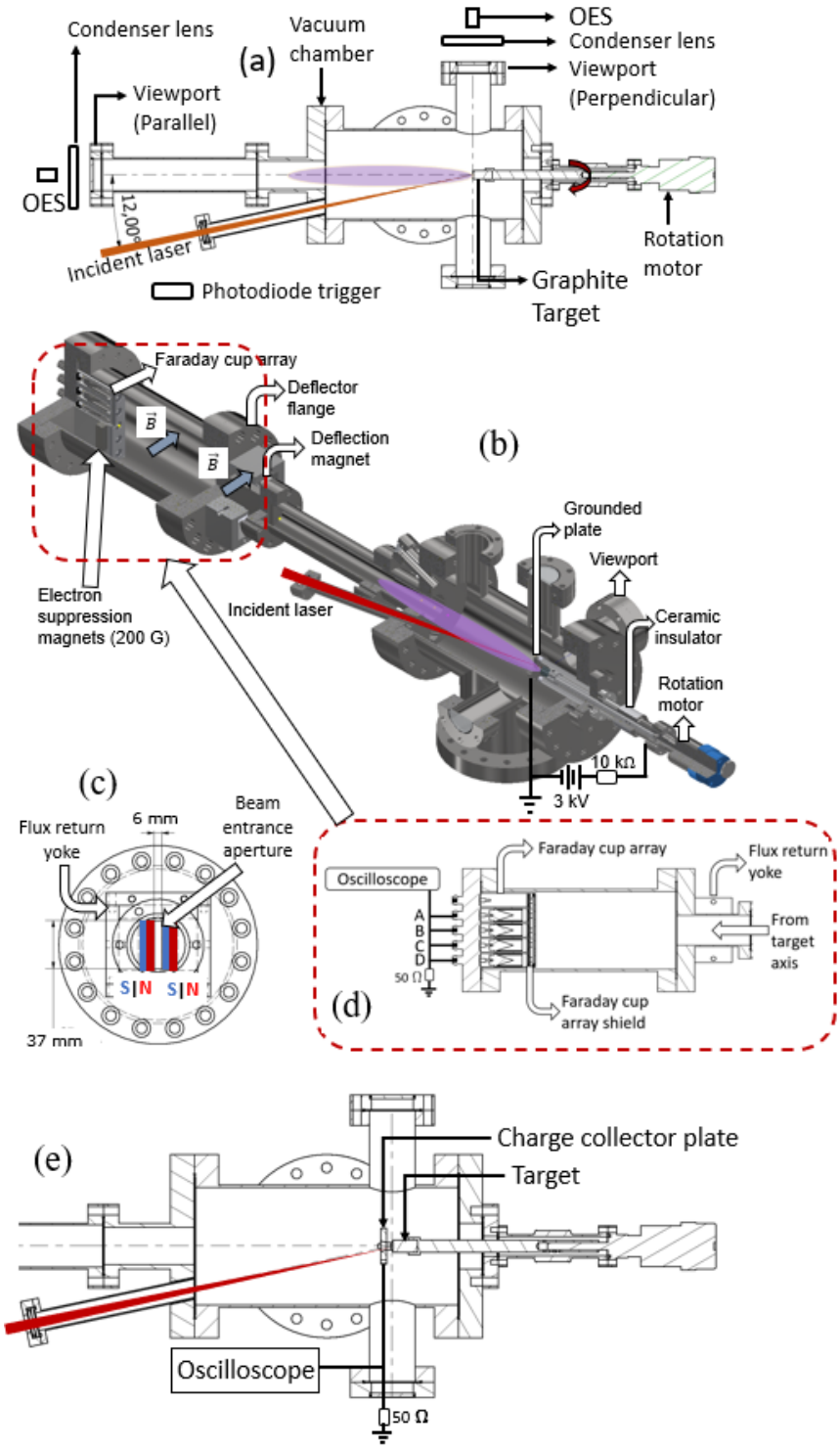

FIGURE 5.2: (a) Laser ablation schematic for emission spectra collection (b) TOF measurement schematic (c) Faraday cup array schematic (d) Deflection region schematic (e) Near-target charge collection experiment schematic

diameter and height are 10 mm, and 20.5 mm, respectively. The laser creates a spot diameter around 1 mm at the center of the target surface. The laser is aligned so that the laser ablates the same spot on the target during rotation at 20 revolutions per minute via a DC motor attached to a vacuum rotational motion feedthrough. The optical emission spectra are collected from two sides: parallel and perpendicular to the target axis via viewport flange attachments. For both arrangements, a converging lens (focal length = 150 mm) focuses light towards an optical fiber connected to an emission spectrometer (USB4000). The data rate of the CCD array of the spectrometer is approximately 0.5 MHz. The wavelength, and sensitivity of the as-received spectrometer were calibrated. However, effects due to the degradation of the internal components of the spectrometer were not evaluated. Nevertheless, the purpose of this work is to compare the relative intensity of the emission spectra parallel and perpendicular to the target axis, thereby foregoing the need for identifying the absolute emission intensity for each corresponding wavelength. The integration time of the spectrometer is set to 1 s to ensure collection of the spectra. An average of 10 spectra is collected during laser ablation at 10 Hz repetition rate. Spectra are collected for every 1000 pulses up to 10000 pulses at 5 GW/cm^2 laser intensity. The time evolution of the emission spectra in LIBS is typically recorded. However, since the aim of this work is to compare the accumulated emission spectra in both parallel and perpendicular regions of the constricted discharge, and estimating an apparent temperature from these spectra, the time-resolved emission measurement is not performed. Moreover, obtaining the time-resolved spectra with delay times below 1 μs, typically performed in LIBS is beyond the capability of the optical emission spectrometer employed in this work. A cylindrical aluminum target (diameter = 10 mm, length = 25 mm) is also employed to replace the graphite target for emission spectra measurements.

In order to investigate the ions present in the laser plasma, the target is biased at 3 kV extraction voltage via a stainless steel target holder while a 5 mm thick aluminum grounded plate is placed 5 mm from the target surface. Then, a time-of-flight (TOF) spectrometer is assembled, as shown in Fig. 5.2 (b), where the incident port of the spectrometer replaces the viewport attachment parallel to the target axis. Neodymium permanent magnets were installed 47 cm from the target which deflect the incoming laser produced plasma at a 200 G magnetic field intensity. Figure 5.2 (c) shows the schematic of the deflection flange. As in Chapter 4, the deflection flange consists of a 37 mm by 6 mm aperture for the incident beam. Neodymium permanent magnets with peak flux density of 670 G are installed, where the deflection magnetic field induces a Lorentz force in the direction of the gravitational force. The total deflection region distance is 4 cm. The TOF signals are collected at an average of 16 pulses at 5 GW/cm^2 laser intensity. The TOF spectrometer consists of a Faraday cup array with four terminals situated approximately 65 cm from the target, shown in Fig. 5.2(d). Each of the cups is terminated by a 50 Ω resistor, and are labelled A-D, where the distance between the axes of each cup is 18 mm. Faraday cup A collects the current against the Lorentz force direction. Faraday cup B collects the

Species	Emission line (nm)
C I	426.9
C II	513.9
C III	465.2
C IV	772.6

TABLE 5.1: Selected carbon emission lines for spectral analysis

current directed along the target axis. Faraday cups C and D collect signals which are deflected along the Lorentz force direction. Electron suppression magnets with 300 G flux density are attached to the grounded Faraday cup array shield.

Figure 5.2(e) shows the schematic for the near-target collection experiment, where current signals from the expanding plume are collected by a 5 mm thick aluminum plate with a 9 mm aperture. The plate is placed 5 mm from the target surface, and is connected to a 500 MHz oscilloscope terminated by a 50 Ω resistor. Experiments are performed at 6×10^{-6} Pa pressure.

5.3 Emission spectra for varying number of pulses

Figure 5.3 shows the emission spectra collected parallel and perpendicular to the target axis. In both directions, the spectra consist of a superposition of multiple carbon peaks ranging from C I to C IV, and continuum radiation. For the emission spectra parallel to the target axis shown in Figure 5.3 (a), the continuum radiation is present up to approximately 930 nm, with the peak at 500 nm. On the other hand, the continuum radiation is present up to 800 nm for the case of 0 to 1000 pulses ablation perpendicular to the target axis shown in Figures 5.3(b) and (c), where the continuum peak ranges from 480 to 520 nm. The carbon species are identified assuming the peaks represent atomic transitions, whose spectroscopic data are obtained from NIST database [13] shown in Table 5.1.

Figure 5.4 shows the continuum radiation intensity evolution for increasing number of laser pulses. The intensities for both parallel and perpendicular directions are normalized with respect to that after 1000 laser shots. Increase in continuum intensities are observed parallel to the target axis until 6000 pulses, where the peak intensity at 510 nm reached almost twice that of the intensity after 1000 shots. Further increasing the number of pulses after 6000 shots results to a decrease in the continuum emission intensity. For the direction perpendicular to the target axis, the continuum emission intensity decreases to around 15 percent of that of after 1000 pulses intensity. After which, the rate of intensity decrease slows down after 8000 pulses.

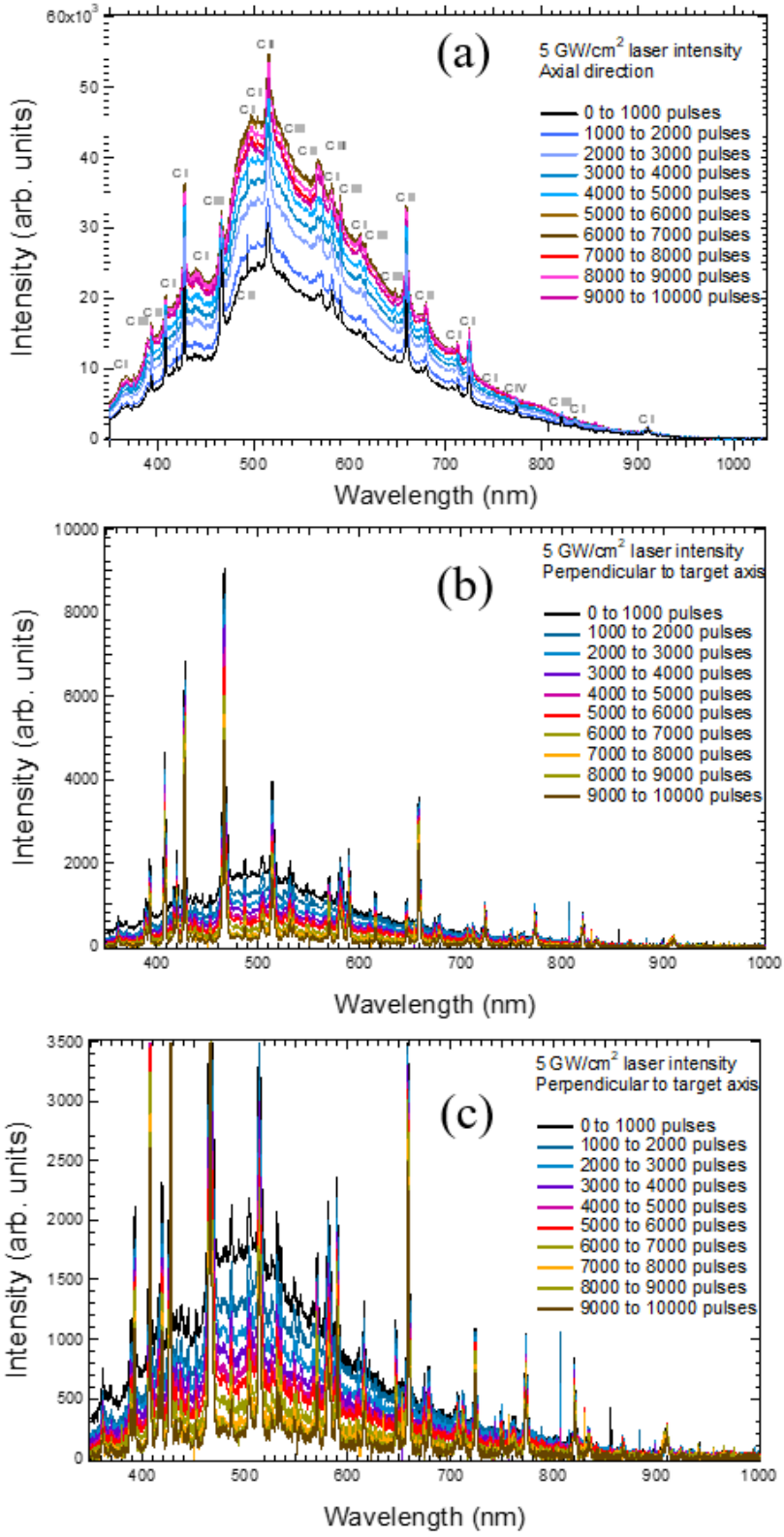

FIGURE 5.3: Emission spectra of carbon due to emission spectra collection (a) parallel and (b) perpendicular to the target axis for increasing number of pulses (c) An enlarged view of (b) along the ordinate axis

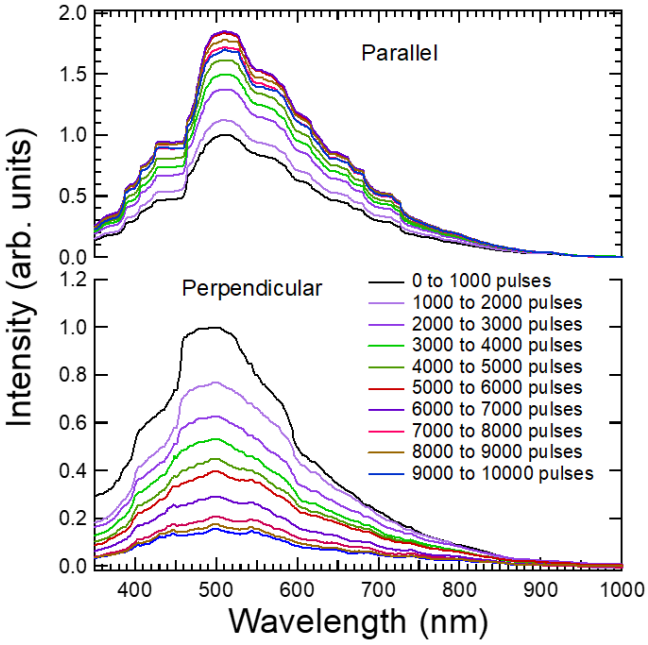

FIGURE 5.4: Carbon continuum spectra for increasing number of pulses

5.3.1 Fits to the Continuum emission

In the emission spectra involving laser induced breakdown of carbon, three fits were attempted for the continuum emission: sum of normal and lognormal distribution, sigmoidal fit, and Planck-like continuum fit. Continuum emission spectra was treated as a Planck-like distribution [14, 15]. The term 'Planck-like' is significant, since for the blackbody distribution case, the assumption is thermal equilibrium. However, as the laser plasma is not in such a condition, the purpose of employing the blackbody fit to the continuum spectra is for attempting to find an apparent temperature. In this subsection, these attempts in fitting the continuum emission are shown.

Sum of distribution functions

The emission intensity is described as:

$$I(\lambda[nm]) = \frac{I_1}{\sigma_1\sqrt{2\pi}} e^{\frac{\lambda-\mu_1^2}{2\sigma_1^2}} + \frac{I_2}{\sigma_2\sqrt{2\pi}} e^{-\frac{(\ln(\lambda-\mu_2)-\mu_3)^2}{2\sigma_1^2}} \tag{5.1}$$

where σ_1, σ_2, μ_1, μ_2 and μ_3 are all fitting parameters. The choice of the parameters is due to the shape of the continuum distribution having two major peaks at 430 and 530 nm. Figure 5.5 shows the fitting of the emission spectra continuum at 5 GW/cm^2 laser intensity after 1000 pulses and 30000 pulses. After 30000 pulses, intensity Despite apparent close agreement with experimental data, this method of fitting only describes the central wavelength of the observed continuum peaks, as well as the intensities of

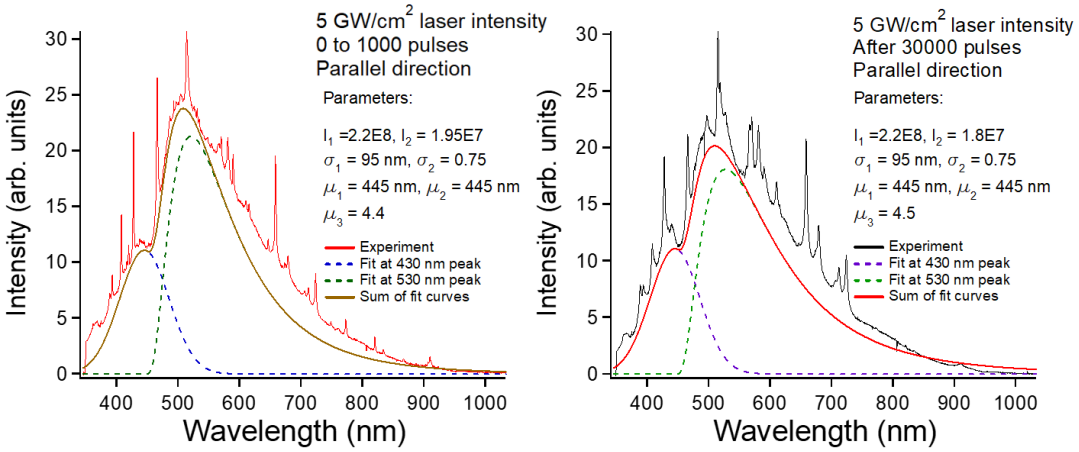

FIGURE 5.5: Continuum emission peak fits of carbon spectra using a normal and lognormal distribution curve shown in Eq. 5.1 at 5 GW/cm^2 laser intensity after (left) 1000 pulses and (left) after 30000 pulses

these peaks represented by I_1 and I_2. Changing the other parameters only changes the width of the distribution, but no physical parameters such as apparent temperature can be extracted from the fits.

Sigmoidal fitting

The sigmoidal fitting is performed since the integral of the Planck distribution resembles the sigmoidal function. As the continuum emission ranges from 291 THz to 857 THz (350 - 1030 nm), $I_{pl}(\nu, T)$ is integrated over all frequencies using trapezoidal rule and is assumed to follow a sigmoidal function given by

$$S_{pl}(\nu, T) = \int I_{pl}(\nu', T)\, d\nu' = \frac{A}{1 + \exp(\frac{\nu_{0.5} - \nu}{\tau})}, \tag{5.2}$$

where $A, \nu_{0.5}$, and τ are fitting parameters. Fitted integrated spectra for both axial and perpendicular directions are shown in Fig. 5.6. The fitting errors for $\nu_{0.5}$ and τ are within the order of 0.1 THz. The intensity of the Planck-like continuum A is obtained by equating the fitting parameter A to the prefactor of Eq. 5.5, where we have $\tau = \frac{kT}{h}\left(1 - \frac{\nu_{0.5}}{\nu}\right)$, and $A = \frac{2h\nu^3}{c^2}\tau$. The estimated average temperature due to the integration over the emission spectrum is then obtained from τ:

$$\begin{aligned} T(\nu)_{ave} &= \frac{1}{\nu_2 - \nu_1} \int_{\nu_1}^{\nu_2} \frac{h\tau\nu'}{k(1 - \frac{\nu_{0.5}}{\nu'})}\, d\nu' \\ &= \frac{1}{\nu_2 - \nu_1} \frac{h\tau}{k} \left(\nu_{0.5} \ln \left| \frac{\nu_2 - \nu_{0.5}}{\nu_1 - \nu_{0.5}} \right| + \nu_2 - \nu_1 \right) \end{aligned} \tag{5.3}$$

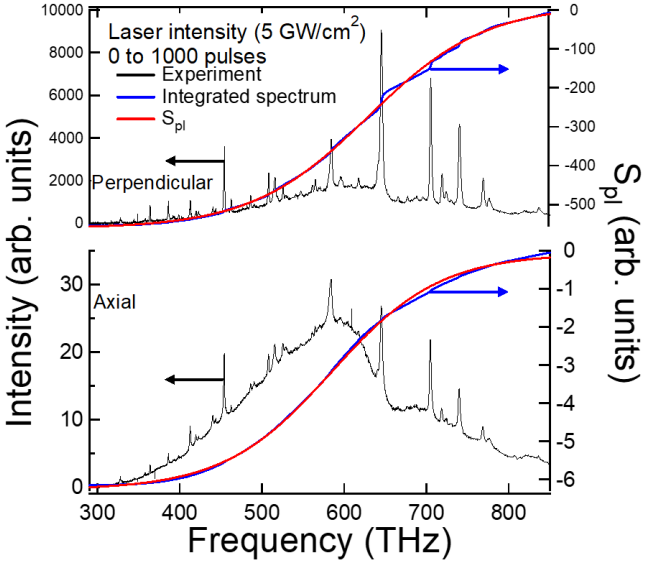

FIGURE 5.6: Sigmoidal fit for carbon emission spectra after 1000 pulses, equation shown in Eq. 5.2

Planck-like Blackbody Fits

The case of thermal equilibrium is not assumed, thus it is noted also that the distribution is not strictly a conventional blackbody. The continuum intensity is fitted under such distribution in order to quantify the evolution of continuum radiation intensity in the formation of the cavity. In the wavelength parametrization, an estimation of the apparent temperature can be obtained by first taking the continuum radiation from the raw spectra. Then, from the Planck blackbody equation:

$$I_{pl}(\lambda, T) = \frac{\lambda^5}{2\pi hc^2} = \exp(\frac{hc}{\lambda k}) \tag{5.4}$$

where h, k, T are the Planck constant, Boltzmann constant, and apparent continuum temperature, respectively. Taking the natural logarithm of both sides, the apparent temperature can be obtained from slope of the line of the $\ln \frac{\lambda^5}{2\pi hc^2}$ vs $\frac{hc}{\lambda k}$ plot. Figure 5.7 shows the Planck-like plot in the wavelength parametrization after 1000 pulses. At 2000 K apparent temperature fits, the fit matches well with the experimental data from 300 to 700 nm, but diverges at higher wavelengths. A least squares fit is performed on the experimental data, which results to be closest to the 2900 K fit, which is near to the 3000 K result in [15].

In the frequency parametrization, the intensity $I_{pl}(\nu, T)$ is then given by

$$I_{pl}(\nu, T) = G\nu^5 e^{-h\nu/kT}, \tag{5.5}$$

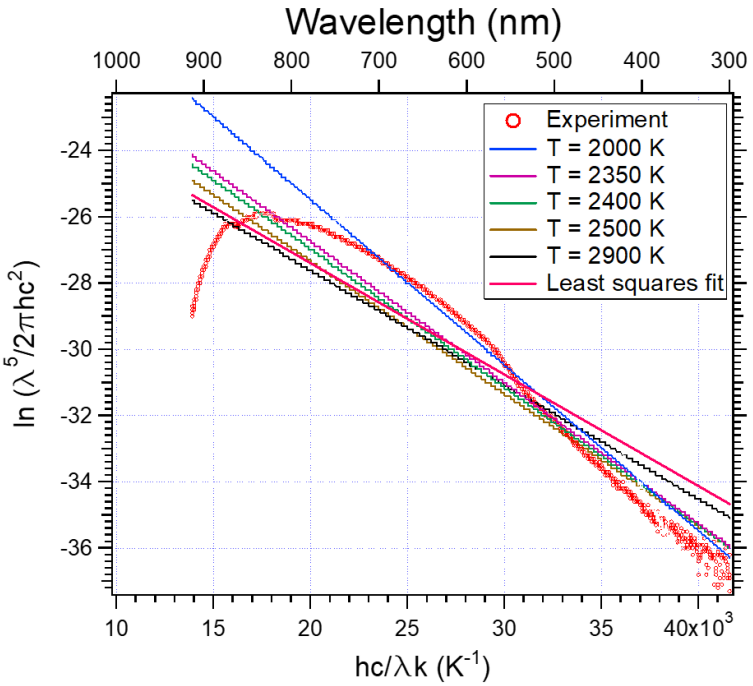

FIGURE 5.7: Plots of $\ln \frac{\lambda^5}{2\pi hc^2}$ vs $\frac{hc}{\lambda k}$ after 1000 pulses, red straight line is the least squares linear fit for the experimental data

where G, ν are the exponential prefactor and emission frequency, respectively. Taking the natural logarithm of both sides, we have

$$\ln\left(\frac{I_\nu}{\nu^5}\right) = \ln G - \frac{h\nu}{kT} \tag{5.6}$$

where the apparent temperature can be obtained from the slope of the line formed by (I_ν/ν^5) versus ν. Figure 5.8 shows the apparent continuum temperature for increasing number of pulses. Since the left-hand side of Eq. 5.6 in the entire optical frequency range consists of a positive and negative slope, only the region with the negative slope, corresponding to wavelengths from 500 nm was taken. Within this region, the following optical frequency ranges were chosen: 500-358 nm, 500-374 nm, 500-390 nm, 500-405 nm, and 500-421 nm. The spectra corresponding to these optical frequencies were fitted to Eq. 5.6 where, from the slope, the average and the standard deviation of the apparent temperature are obtained. Fitting was performed on the spectra from 1000 to 10000 pulses. The obtained apparent temperature is plotted with the number of pulses and is shown in Fig. 5.8. The estimated apparent continuum temperature is higher in the perpendicular direction than that in parallel direction. The obtained standard deviation of the apparent temperature in the parallel direction ranges from 51 to 65 K, while a deviation from 48 to 316 K is calculated in the perpendicular direction. An increase of approximately 200 K in the average apparent temperature in the perpendicular direction for increasing pulses is observed, whose rate decreased after 6000 shots. Since the error increases for increasing number

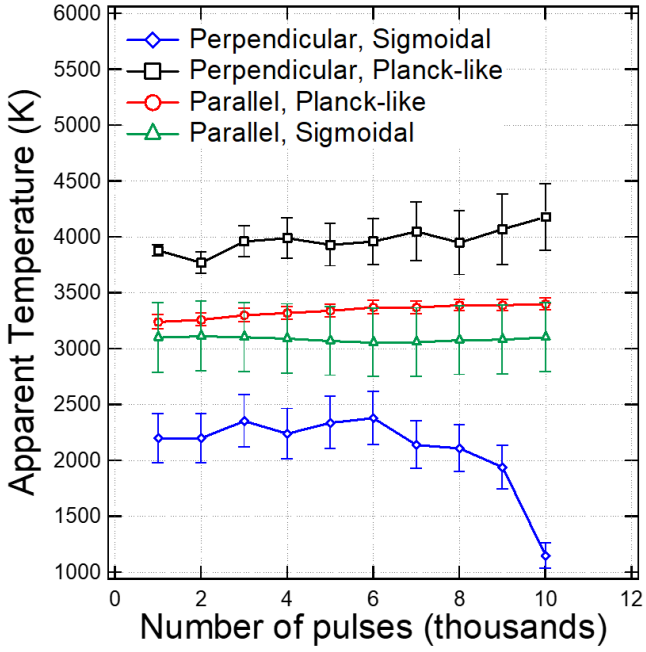

FIGURE 5.8: Apparent continuum temperature for increasing number of pulses in the parallel and perpendicular directions for sigmoidal and Planck-like fits

of pulses, no significant correlation in the apparent temperature with the number of pulses is observed in the perpendicular direction. Comparing the plots in the perpendicular direction for sigmoidal and Planck-like fits, there is a significant discrepancy between the values obtained from the two fits. This is due to the lower continuum intensity present in the perpendicular direction, leading to higher errors in the measurement. For the plot for sigmoidal fitting, the temperature decrease to 1000 K after 10000 pulses indicates the sensitivity of the sigmoidal fit in the apparent temperature measurement as continuum intensity decreases.

5.3.2 Atomic and ionic emission line spectra

Since the emission spectra consist of atomic transitions and continuum radiation, the latter should be subtracted in order to observe the evolution of the carbon emission line transitions as the number of pulses is increased. Performing this subtraction, the peak evolution of the emission line intensities corresponding to emission lines of C I (427.0 nm, $2s^2 2p 3s \leftarrow 2s^2 2p 5p$), C II (514.0 nm, $2s2p(^3\mathrm{P}^o)3s \leftarrow 2s2p(^3\mathrm{P}^o)3p$), C III (465.2 nm, $1s^2 2s 3s \leftarrow 1s^2 2s 3s$), and C IV (772.8 nm) are shown in Fig. 5.9. For the spectra directed perpendicular to the target axis, decrease of approximately 40 percent is observed for the C III ion after 10000 pulses ablation. The intensity change perpendicular to the target is plotted with an exponential fit, where C II has the highest rate of decrease with a calculated rate constant of 5.7×10^{-5}/pulse. A similar trend was observed for the C I, C III, and C IV lines in this direction. On the other hand, the emission line evolution

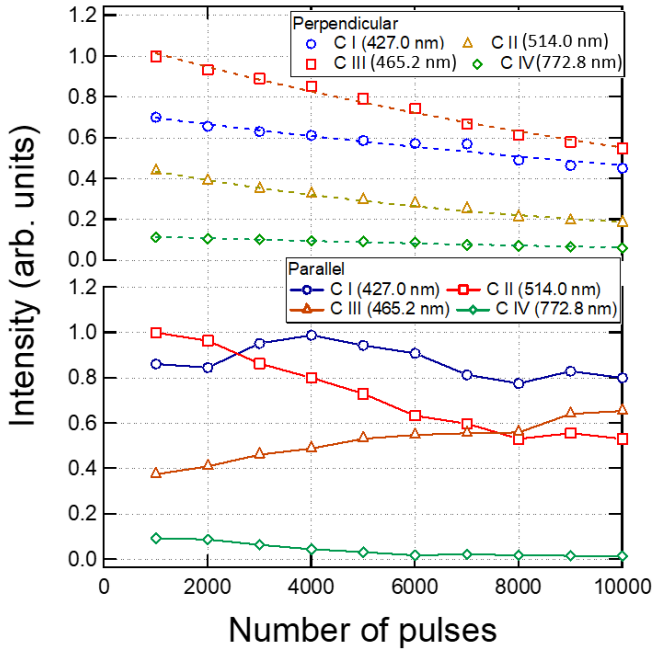

FIGURE 5.9: Emission line peak evolution of carbon spectral lines from C I to C IV for increasing number of pulses, dashed lines represent exponential fits

for increasing number of pulses parallel to the target axis shows an initial increase in the C I intensity from after 1000 pulses to after 4000 pulses, and in C II intensity from after 1000 pulses to 10000 pulses. The C II and C IV line emission intensities decrease as the number of pulses is increased, where the rate of decrease of C III slows down after 8000 pulses. The intensity of C III is higher than that of C I until after 2000 pulses, while the C II emission exceeds that of C III from after 8000 pulses. Parallel to the target axis, the emission intensity increases up to 7000 pulses, followed by a subsequent decrease for increasing number of pulses. On the other hand, the emission spectra perpendicular to the target axis decreases for increasing number of pulses.

Boltzmann fitting

The Boltzmann analysis for electron-induced excitation is employed in laser induced breakdown plasmas as a form of obtaining an excitation temperature [10, 16]. The Boltzmann form for a species p with an equilibrium temperature T_p is given by

$$\ln\left(\frac{I_k}{g_k A_k \nu_{ki}}\right)_p = -\frac{E_k}{kT} + \ln\left(\frac{N_p}{Z(T_p)}\right), \tag{5.7}$$

where I_k represent the intensity, g_k the degeneracy of the charged species, A_k the transition probability, k_b the Boltzmann constant, ν_{ki} the photon frequency of transition from higher level k to lower level i, E_k the upper level energy, N_p, the number density, and $Z(T)$ the temperature-dependent

TABLE 5.2: Selected spectral lines of C I and C III from the laser plasma and corresponding spectral data of $g_k A_k$ and E_k obtained from [13]

Species	Wavelength (nm)	$g_k A_k (10^7)$	$E_k\ (cm^{-1})$
C I	427.0	10	85399.8
	580.6	0.041	81311.1
	705.88	0.048	83877.3
	711.7	1.53	83761.2
C III	466.0	6.81	329706.4
	534.7	1.48	340127.5
	589.5	5.55	340101.8
	646.2	6.60	358732.9

partition function. From the linear plot between the left hand side with E_k, the electron temperature can be obtained from the slope. In this work, only the electron temperature is estimated. The selected spectral lines of C I and C III are shown in Table 5.2.

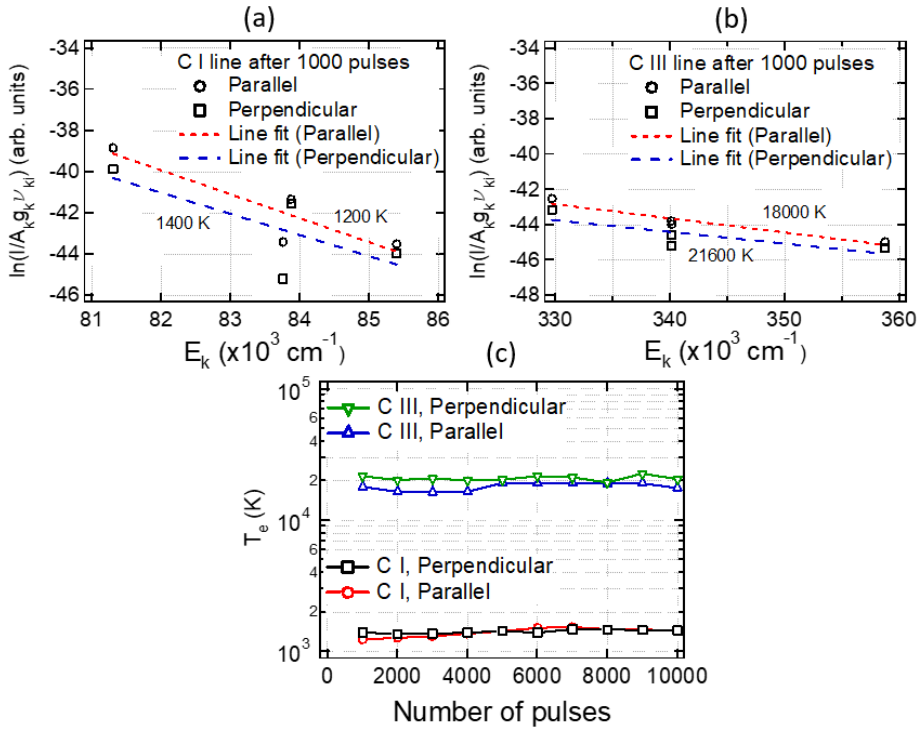

FIGURE 5.10: Boltzmann plots of the (a) C I and (b) C III emission spectra for axial and perpendicular emission from 0 to 1000 pulses (c) Electron temperature obtained from Boltzmann analysis for increasing number of laser pulses

In obtaining the intensity for the emission spectra containing the continuum, a reference wavelength for each emission line is selected. The intensity difference corresponding to the the peak and the reference wavelength is taken as the emission line intensity without the continuum.

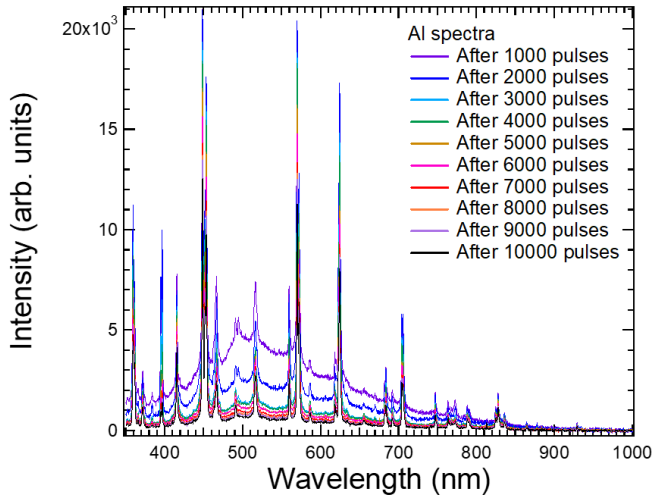

FIGURE 5.11: Emission spectra of aluminum plasma at 5 GW/cm^2 intensity ablation

Species	Emission line (nm)
Al I	669.6
Al II	624.1
Al III	447.9
Al IV	462.6

TABLE 5.3: Selected aluminum emission lines in the perpendicular direction for spectral analysis

Figure 5.10 shows the Boltzmann fit for the C I and C III emission after 1000 pulses. In both species, the electron temperature obtained in the perpendicular direction is higher than that in the axial direction. The electron temperature corresponds to approximately 0.14 and 0.17 eV for the axial and perpendicular directions, respectively, both of which are far below the laser photon energy. On the other hand, the electron temperature in C III line emission correspond to 2.23 and 2.67 eV, for the axial and perpendicular directions respectively. Figure 5.10 shows the electron temperature evolution for increasing laser pulses in both directions. The estimated electron temperature did not significantly vary as the number of laser shots increased, and is within the 13000-20000 K and 1000-2000 K range for the C III and C I emission lines, respectively.

Aluminum emission spectra

Figure 5.11 shows the emission spectra of aluminum for increasing number of pulses in the perpendicular direction. As with the carbon spectra, continuum emission spectra along with the atomic and line spectra are also observed to decrease for increasing number of laser shots. Selected lines for Al are shown in Table 5.3.

Figure 5.12 shows the peak continuum intensity evolution for increasing number of pulses. Continuum emission decay is observed for increasing

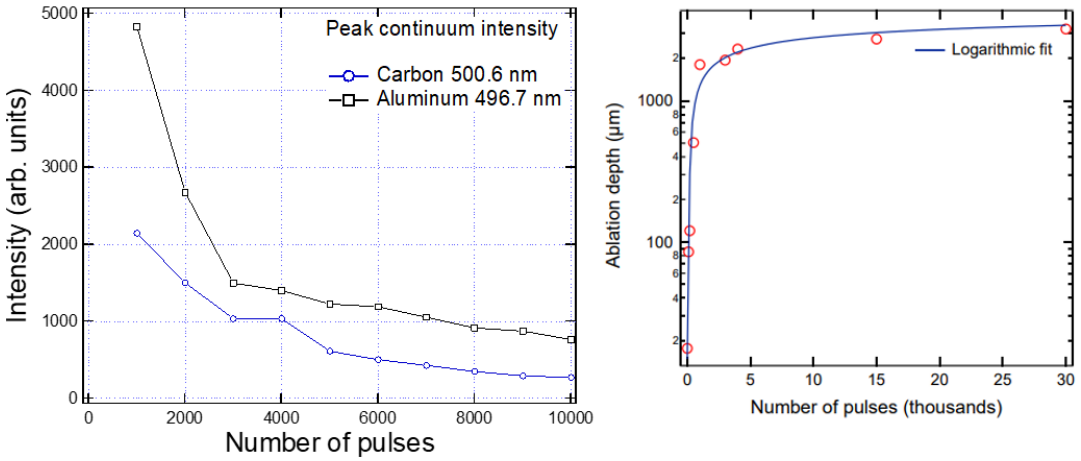

FIGURE 5.12: (left) Peak continuum emission intensities of carbon (500.6 nm) and aluminum spectra (496.7 nm) for increasing number of laser shots (right) ablation depth for increasing number of pulses

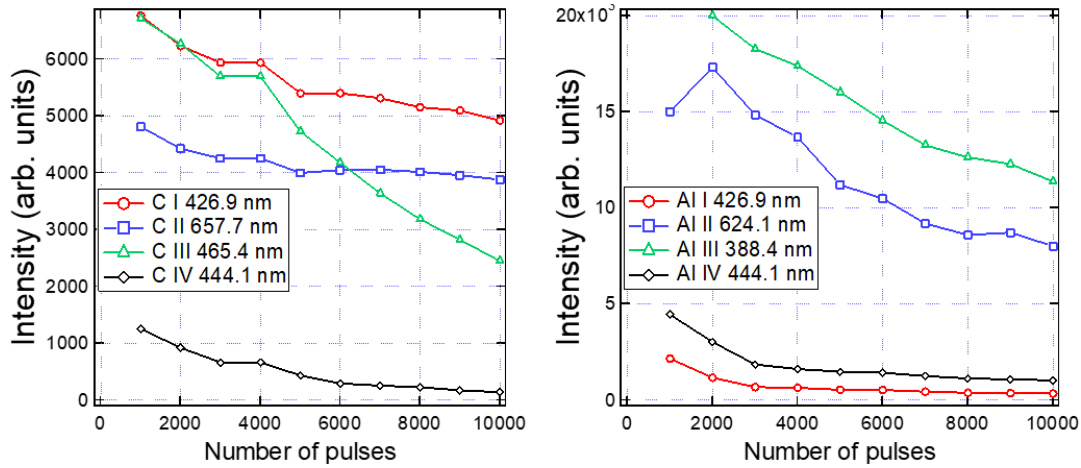

FIGURE 5.13: Peak emission line intensity of (left) carbon and (right) aluminum at perpendicular directions for increasing number of pulses

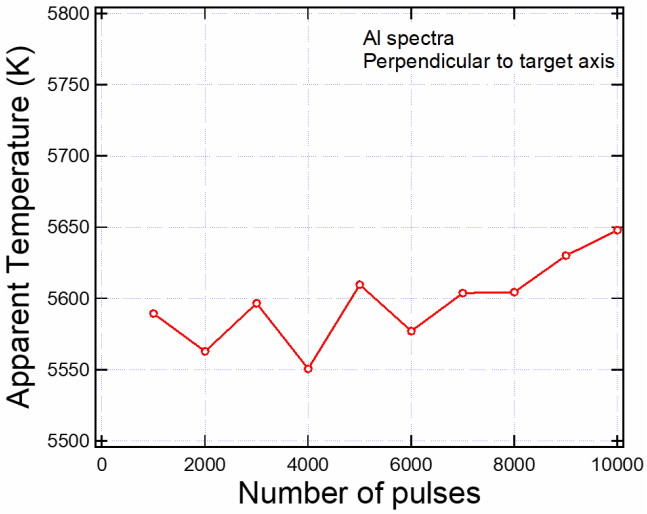

FIGURE 5.14: Apparent temperature obtained from Al target using Planck-like fitting

number of laser shots. Aluminum spectra is observed to have a higher continuum intensity than carbon. This is due to the increased number of recombination electrons produced by the laser on the aluminum surface. Figure 5.14 shows the apparent temperature obtained from the Planck-like fitting of Eq. 5.5 in the optical frequency range from 436 THz to 868 THz (345 to 430 nm). The obtained temperature is similar to the 6000 K value obtained from nanosecond laser of Al [15].

Figure 5.13 shows the peak line intensities for carbon and aluminum peaks. Both targets show decrease in line intensity for increasing number of laser shots. Comparing the peak intensities, aluminum showed a higher ionic line (C III versus Al III) line intensity with aluminum having almost three times intensity than that of carbon. On the other hand Al I atomic line intensity is lower than that of atomic carbon line C I. In order to evaluate the ions produced for increasing cavity confinement, the ionization fraction I_{ion} is defined as

$$I_{ion} = \frac{I_{A^+}}{I_A}, \tag{5.8}$$

where I_{A^+} and I_A represent the intensity of the carbon or aluminum ionic and atomic line, respectively. Figure 5.15 shows the ionization fraction of carbon and aluminum for increasing number of pulses. Line intensity fo singly ionized carbon C II is observed to increase slightly for increasing number of pulses, while the doubly and triply ionized carbons C III and C IV decrease. At around 6000 pulses the line intensities of C II and C III are approximately equal, after which C III line intensity decreases to half of the original intensity. For aluminum the Al II and Al III ion line significantly increased for until 3000 pulses. After which the increase slowed down. Al II, Al III, and Al IV emission line ionization fraction of aluminum is observed to be approximately 30, 27, and 10 times greater than that of carbon, respectively.

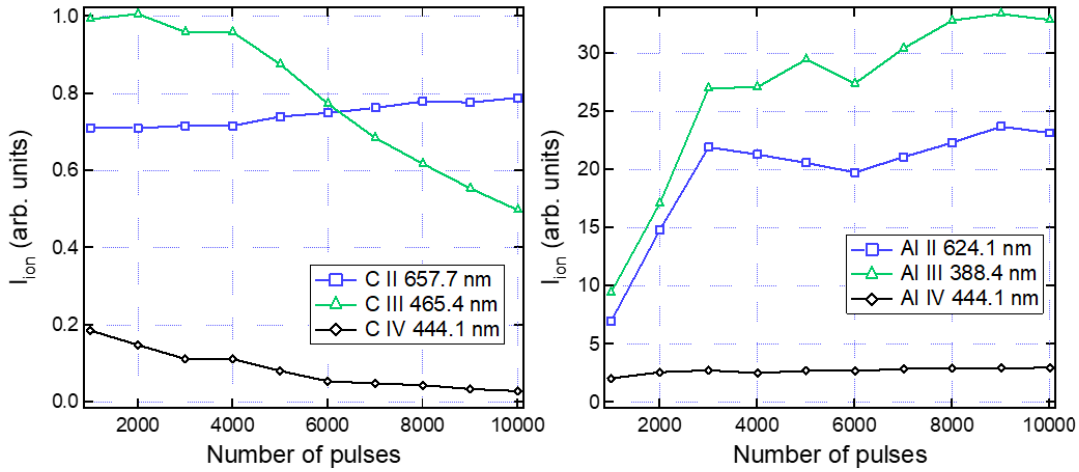

FIGURE 5.15: Ionization fraction of emission lines in (left) carbon and (right) aluminum emission spectral lines

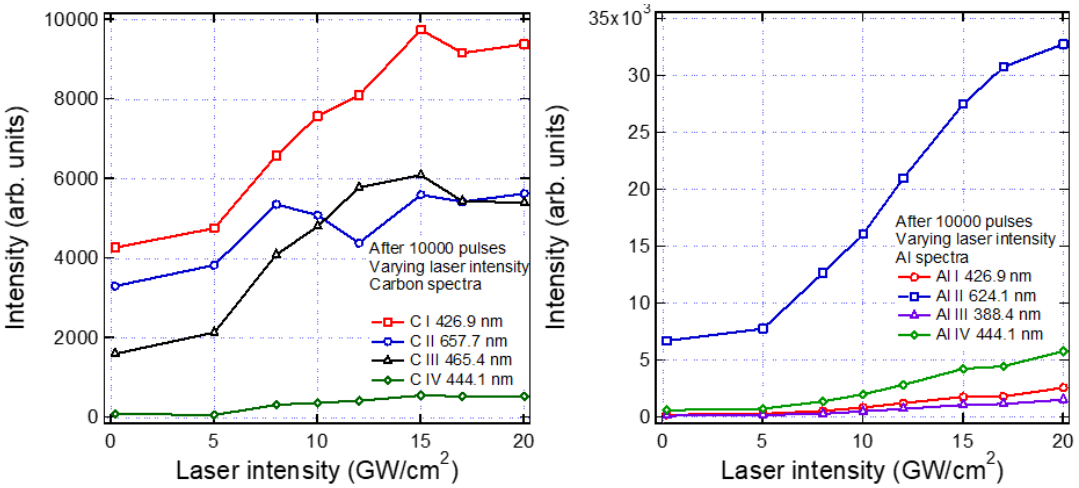

FIGURE 5.16: Peak line intensity of (left) carbon lines for increasing laser power density

Figure 5.16 shows the peak line intensity of carbon and aluminum lines for increasing laser power density. Increasing atomic and ionic lines are observed for both targets. For carbon emission spectra, C I emission line is highest. Ionic lines C II and C III are observed to be similar intensities from above 10 GW/cm^2 above which C III exceeds C II and dropping so approximately same line intensities from 17.5 GW/cm^2. For aluminum, the ionic line Al II peak intensity is significantly higher than that of the other emission peak lines, while the rate of increase slows down above 17.5 GW/cm^2 laser intensity. Peak intensity of Al IV is observed to be higher than that of the Al I and Al II. Figure 5.17 shows the ion fraction at 10000 pulses for varying laser intensity. Ion peak C II shows a decrease above 7.5 GW/cm^2 while I_{ion} C III and C IV is observed to increase. Al II ion fraction decrease is observed, while Al III and Al IV ion fraction has not changed significantly.

In order to find a correlation in the charge evolution of both carbon

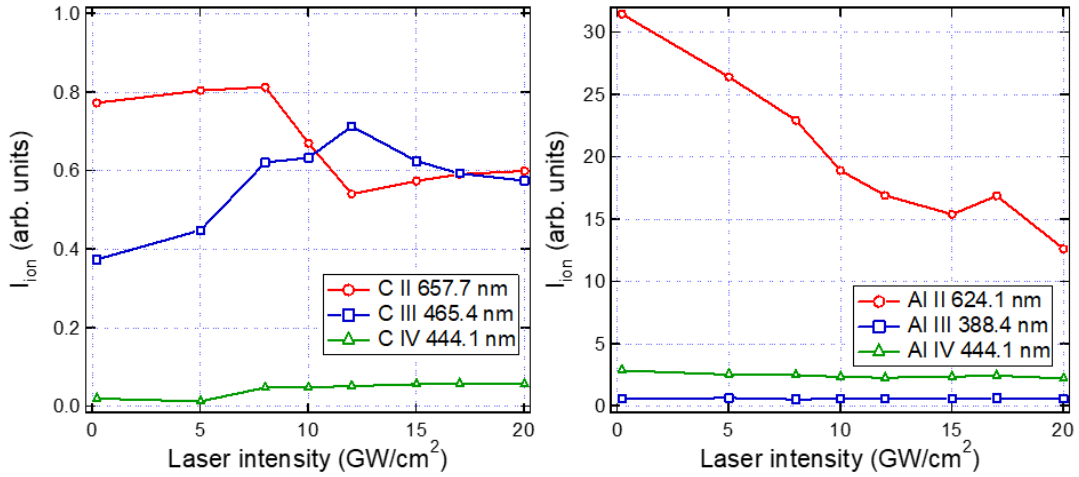

FIGURE 5.17: Ion fraction of (left) carbon and (right) aluminum lines for increasing laser power density

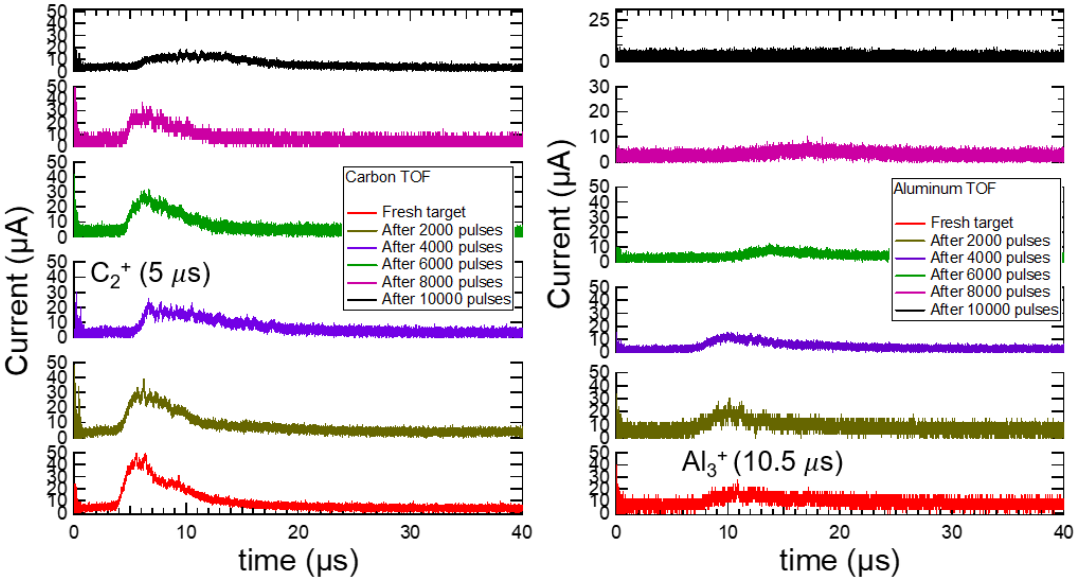

FIGURE 5.18: Time-of-flight signals of (left) carbon and (right) aluminum target collected by FC 4 (bottommost Faraday cup) for increasing number of pulses

and aluminum, the time-of-flight signals for both targets collected by the FC 4 (bottommost Faraday cup) are shown in Figure 5.18. As with the previous chapter for carbon TOF, C_2^+ ions serve as dominant ions, and ion current intensity increase is observed. For carbon, current distribution corresponding to later times are also observed. For aluminum, ion peak intensity decrease as well as shift towards later times were also observed for increasing number of pulses.

5.4 Discussion

The optical emission spectra consist of continuum and emission line peaks. From the previous section, ions represented by emission line peaks are formed by electron ionization, while continuum radiation is ascribed with radiative recombination due to free-bound transitions [17]. When the number of laser shots is increased, the plasma is initiated inside the cavity. Electron density inside the cavity would increase, and electron ionization probability increases. The increase in continuum intensity in the spectra directed parallel to the target axis until 6000 pulses shown in Fig. 5.3 suggests the increase in radiative recombination in the cavity due to collisions from the dense plume. On the other hand, only a decrease in the emission line, as well as continuum intensity is observed, since these spectral lines are represented by ions and neutrals which have escaped the cavity hole and underwent recombination or de-excitation, which decreases for increasing number of pulses. The same may explain the lower continuum intensity perpendicular, as compared with that parallel to the target surface. Electrons produced within the cavity from the initial expansion participate in the recombination, while those fewer electrons which have escaped the cavity would lead to the emission perpendicular to the surface.

Not only that radiative recombination increases when the cavity is present, three body recombination mechanisms also played a role in converting ions to neutrals. The exponential decrease of the line intensity suggests the decrease in ablation rate as the number of laser shots increased, shown in Fig. 5.12.

In the comparison of the different methods for obtaining the apparent temperature due to the continuum radiation, while the sum of normal and lognormal distributions do not show physical parameters apart from continuum intensity, the sigmoidal fitting and the Planck radiation spectra, although it employed the range of frequencies in the emission spectra, $T(\nu)$ is in Eq. 5.3.1 is observed to be independent of spectral intensity. This indicates that the intensity as a form of distribution must be included, since the intensity relates to the population, and therefore the electron density. The significant difference between sigmoidal and Planck-like distribution in Fig. 5.8 shows the effect of continuum intensity on the obtained temperature. From 6000 to 10000 pulses, the obtained apparent temperature in the perpendicular direction lowers down to 1000 K, despite the ablation rate not significantly changing from this interval. This indicates a further limitation in the sigmoidal plot. However, for the direction parallel to the target axis,

the sigmoidal and Planck-like fitting almost match at approximately 3000 K apparent temperature. The attempt at fitting using the Boltzmann plot shown in Fig. 5.10 aims to find an electron temperature for increasing pulses. The C III line temperature, compared to the C I line is approximately 10 times higher, due to the higher ionization energy required to produce higher ionization states. This temperature can be comparable to that of a result based on a thermal model, where the surface temperature reaches approximately 15000 K [18]. In the early stage of the plasma, electron energy is highest, therefore participate in the collisions. As the electrons lose energy through radiative and nonradiative collisions, the electron temperature goes down. Once the electrons escape in the cavity, the excited states recombine to a lower transition energy, thus lower temperature. One point to consider is that the spectra is collected at an accumulation, rather than a delayed collection, which means that the early stage of the plasma is not captured. How can electrons be stated to dominate the initial stage of the plasma? The time-of-flight signals from the near target charge collection results in Fig. 3.9 and 3.12 showed the initial signal corresponding to a burst of electrons, which have slowed down for increasing number of pulses. This explains the reduced obtained temperature from the emission. However, the time-of-flight signals obtained a temperature, assuming an electron energy $(3/2)kT_e$, of 6700 K for a fresh target, which is about one-third that of the obtained value from the Boltzmann plot. Therefore, a 'proper' temperature cannot be obtained from the simple accumulation of the optical spectra. The apparent temperature from the continuum radiation, however, suggests a closer relation to the obtained temperature from the electron time-of-flight.

In the peak intensity comparison between carbon and aluminum spectra shown in Fig. 5.13, the peak continuum intensity of Al is higher than that of carbon. This is due to the lower ionization energy of aluminum of 5.9, where electrons are easily produced than carbon. The aluminum peak continuum intensity also decreases for increasing number of pulses due to the electron energy loss. Compared to carbon, the intensity of ionic lines Al II and Al III shown in Fig. 5.13 is higher than the atomic lines. This indicates that the probability of ion formation is higher in these spectral lines. From the ionization fraction shown in Fig. 5.15, the enhancement of only lower ionized states indicates the increase in electron density outside cavity participating in electron ionization with a lower energy. Increasing cavity depth for increasing number of pulses shows the energy loss which lead to ionization of lower charge states. For aluminum, the higher ion fraction corresponding to Al II and Al III similarly correspond to the higher ionization probability for lower charges. Increase in ionization fraction from 1000 to 3000 pulses suggests an increase in electrons recombined on the surface that would increase the formation of singly and doubly charged ions.

After 10000 pulses when the laser intensity is increased, the increase in peak intensity indicates the increase in the amount of ablated target. The increase in intensity reaches a threshold, indicating the reduction of ablation rate with the intensity increase. For aluminum, the higher intensity of Al II shows the increase in ionization of singly charged Al compared

to higher states. as for carbon, C II ionization is higher until 10 GW/cm^2, shown also in the ion fraction in Fig. 5.17 where C III ion fraction exceeds C II until 15 GW/cm^2 intensity. This is due to more electrons available for higher charge state ionization. For Al, the decrease in Al II ion fraction for increasing intensity indicates the increase of Al I intensity as well, since both lines increase with intensity. Since more electrons and ions are produced, three-body recombination probability is also increased, leading to the de-excitation of the ionic species.

5.5 Summary

In this chapter, optical emission spectra of laser produced plasmas under cavity confinement were investigated in the directions parallel and perpendicular to the target axis by accumulation during 10 Hz repeated ablation on a rotating target. Continuum enhancement is observed parallel to the target axis, while continuum decrease is observed for increasing number of pulses perpendicular to the target axis. Apparent continuum temperature is obtained through sum of normal-lognormal, sigmoidal, and Planck-like fits, for which advantages and disadvantages of these fitting methods were described. Carbon apparent continuum temperature parallel to the axis was found to be approximately 3000 K, while perpendicular direction, sigmoidal and Planck-like values show significant discrepancies. Peak intensity evolution showed the effect of the cavity contributing to increase in electron density leading to increase in collisions and radiative, as well as three body recombination among plasma constituents. Perpendicular to the target surface, ion fractions corresponding to the ratio of emission to ionic lines were evaluated, where the decrease of ionic intensity are shown as a consequence of increasing confinement and electron energy loss. Energy loss is correlated with the energy loss from charge collection experiments.

References

[1] S. Amoruso, R. Bruzzese, N. Spinelli, and R. Velotta, J. Phys. B **32**, R131–R172 (1999).

[2] J. P. Singh and S. Thakur, ed., *Laser-Induced Breakdown Spectroscopy* (Elsevier, Cambridge, 2007) p. 3-5.

[3] A. K. Knight, N. L. Scherbarth, D. A. Cremers, and M. J. Ferris, Appl. Spec. **54**, 3, pp. 331-340 (2000).

[4] D.A. Cremers, Space Applications of LIBS. In: Musazzi, S., Perini, U. (eds) Laser-Induced Breakdown Spectroscopy. (Springer Series in Optical Sciences, vol 182. Springer, Berlin, Heidelberg, 2014).

[5] W. Wang, S. Li, H. Qi, B. Ayhan, C. Kwan and S. Vance, 2014 6th Workshop on Hyperspectral Image and Signal Processing: Evolution in Remote Sensing (WHISPERS), pp. 1-4 (2014).

[6] B. Bhatt, K. H. Angeyo and A. Dehayem-Kamadjeu, Anal. Methods, **10**, 791-798 (2018).

[7] S. C. Jantzi and J. R. Almirall, Forensic Applications of LIBS. In: Musazzi, S., Perini, U. (eds) Laser-Induced Breakdown Spectroscopy. (Springer Series in Optical Sciences, vol 182. Springer, Berlin, Heidelberg, 2014).

[8] A. A. Voevodin, J. G. Jones, and J. S. Zabinski, J. Appl. Phys. **92** 724 (2002).

[9] R.W.P. McWhirter, in: R.H. Huddlestone, S.L. Leonard (Eds.), Plasma Diagnostic Techniques, Academic Press, New York, 1965, pp. 201–264, Chapter 5.

[10] T. Fujimoto, *Plasma Spectroscopy* (Clarendon Press, Oxford, 2004) p. 205-212.

[11] G. Cristoforetti, A. De Giacomo, M. Dell'Aglio, S. Legnaioli, E. Tognoni, V. Palleschi and N. Omenetto Spectro. Acta B **65** 86–9 (2010).

[12] J. E. A. Hernandez II, S. Yamada, S. Sasaki, A. V. Catapang and M. Wada, Plasma and Fusion Res. 17, 2406018 (2022).

[13] National Institute of Standards and Technology (NIST) Atomic Spectra Database, NIST Atomic Spectra Database (U.S. Department of Commerce, 1999), http://physics.nist.gov/ cgi-bin/AtData/main_asd.

[14] L. Nemes, A. M. Keszler, C. G. Parigger, J. O. Hornkohl, H. A. Michelsen and V. Stakhursky, Appl. Opt. **46** 19 (2007).

[15] A. De Giacomo, R. Gaudiuso, M. Dell'Aglio and A. Santagata, Spectrochim. Acta B **65** 385-394 (2010).

[16] S. S. Harilal, C. V. Bindhu, R. C. Isaac, V. P. N. Nampoori and C. P. G. Vallabhan, J. Appl. Phys. **82** 2140 (1997).

[17] A. De Giacomo, Spectrochim. Acta Part B **58** 71–83 (2003).

[18] S. Sinha, J. Laser Appl. **30**, 012008 (2018).

Chapter 6

Thin film production via pulsed laser deposition

6.1 Introduction

Following the investigation of ions and electrons from the previous chapters, it is of significance to investigate the neutral particle production via pulsed laser. Nanosecond laser ablation is also sought for its capability to produce thin films with a minimum requirement of only a laser source and a vacuum chamber. Pulsed laser deposition, or PLD, is the process of thin film production by directing the substrate to the ablation plume near the target surface [1]. Some advantages of PLD over traditional physical vapor deposition (PVD) methods such as molecular beam epitaxy (MBE) involve the high thin film production rate (3 to 5 magnitudes faster than MBE) [2]. In terms of deposition control, deposition rate in PLD can be controlled through the change in laser repetition rate. Applications of PLD involve the deposition of virtually any target [2] since the laser power can be modified readily. For carbon, diamond-like films were formed using PLD [3, 4].

Mechanisms involving the thin film production for PLD applications involve condensation from the vaporized plume. In the case of typical laser ablation without a cavity, free expansion of the plume is followed by condensation of the primary particles [5]. This condensation is the reason why in typical PLD applications, the ablation is injected with a buffer gas to assist the plume cooling process [6], where the gas particles increase the probability of collision-induced cooling with the ablated constituents, also resulting to confinement near the target surface.

In the work of Inoue *et. al* where onion-like carbon nanoparticles were produced via repeated ablation of graphite with and without a target cavity, as shown in Fig. 6.1. Confinement of the plume expansion is also argued for which the ablated constituents get re-vaporized after multiple irradiation [5]. Introduction of reactive gas assists the condensation process and further cools down the plume.

In this chapter, carbon films deposited during the time of flight experiments performed in Chapters 4-5 are investigated. In the aforementioned experiments, a buffer gas was not introduced, therefore only the cavity assists the collisions within the produced plume.

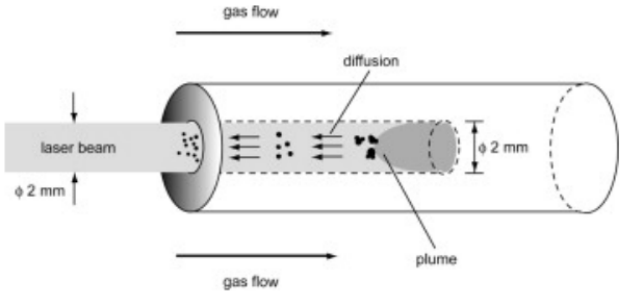

FIGURE 6.1: Schematic of cavity-induced PLD. Adopted from Ref. [5]

6.2 Experiment schematic

The schematic of the PLD experiment is shown in Fig. 6.2. A Q-switched Nd:YAG laser (wavelength = 1064 nm, repetition rate = 10 Hz) is incident on the axis of a target surface at 12 ° measured from the cylindrical target axis at 5 GW/cm^2 laser intensity while being rotated along the target axis. The laser makes a hole diameter of 1 mm with the target. Substrates were installed at two distances: 4 mm and 8 mm from the target surface, indicated by the labels 'back plate' and 'extraction plate', respectively. The substrates are held with an aluminum substrate holder. The materials used for the substrates are 0.25 mm thick SUS 304 sheets and 1 mm thick glass slides attached to the substrate holders via carbon and polyimide tape. The material used for the target is graphite. In this chapter, only the film morphology are characterized by scanning electron microscopy (SEM). Current from the extraction plate is measured by a 500 MHz oscilloscope.

6.3 Results

Figure 6.3 lists the substrate images 4 mm and 8 mm from the target surface after 10000 pulses. The diameter at which the deposition can be observed for the holder 4 mm from the target surface is 20 mm, while this diameter is 12 mm at the holder 8 mm from the target surface. Figure 6.4 shows the scanning electron micrographs of graphite sample on a SUS304 substrate at 4 and 8 mm from the target surface after 10000, 20000, and 30000 pulses. At 4 mm from the target surface, columnar, tipped structures are observed after 10000 pulses. The structures have an average of 1 μm width and an angle of 30°. As the number of pulses is increased, the conical structures became fewer, and spherical deposits with diameters from 100 nm, emerge at the cone tips. After 30000 pulses, the tip of the columnar structures became duller, and spherical structures are formed at the tips. For the substrates placed 8 mm from the target surface, the film structure are observed to be rounded and compact, where after 20000 pulses the the round particles become smaller. After 30000 pulses, the particles were observed to be smaller. In estimating the particle size difference for varying number of pulses at this distance, the micrograph is post-processed using

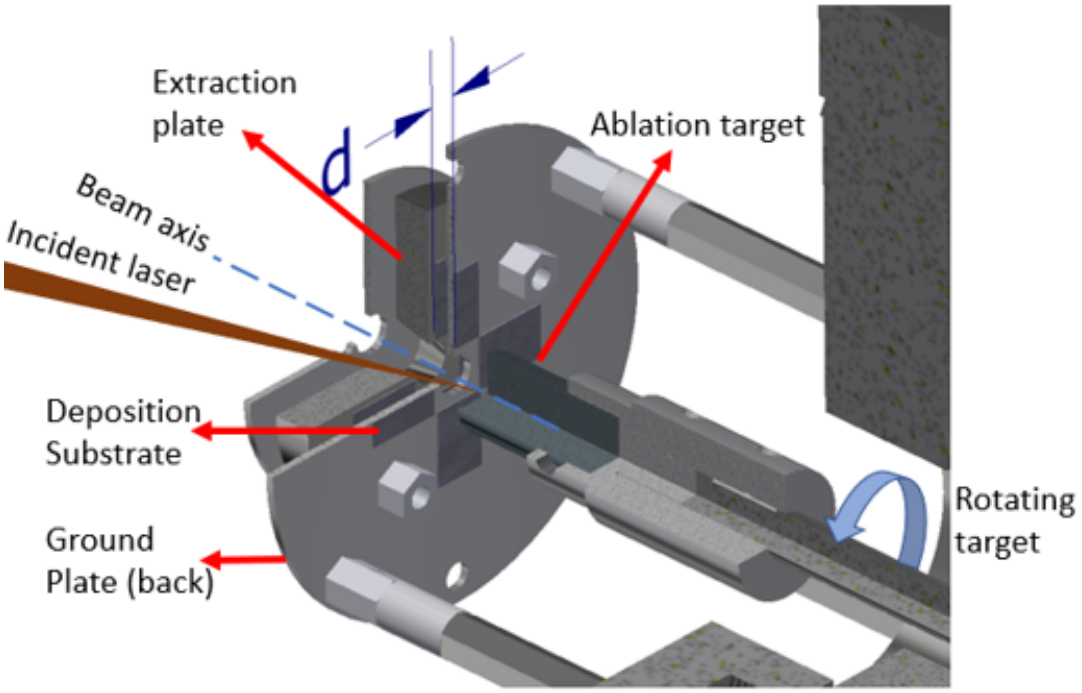

FIGURE 6.2: PLD experimental schematic

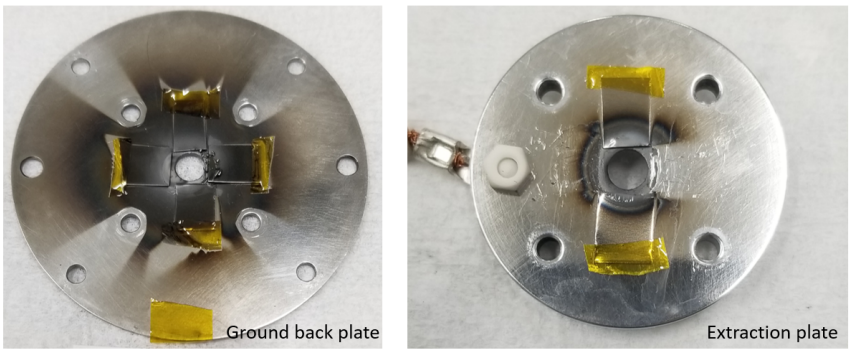

FIGURE 6.3: Substrate holder images (a) 4 mm (b) 8 mm from the target surface after 10000 pulses

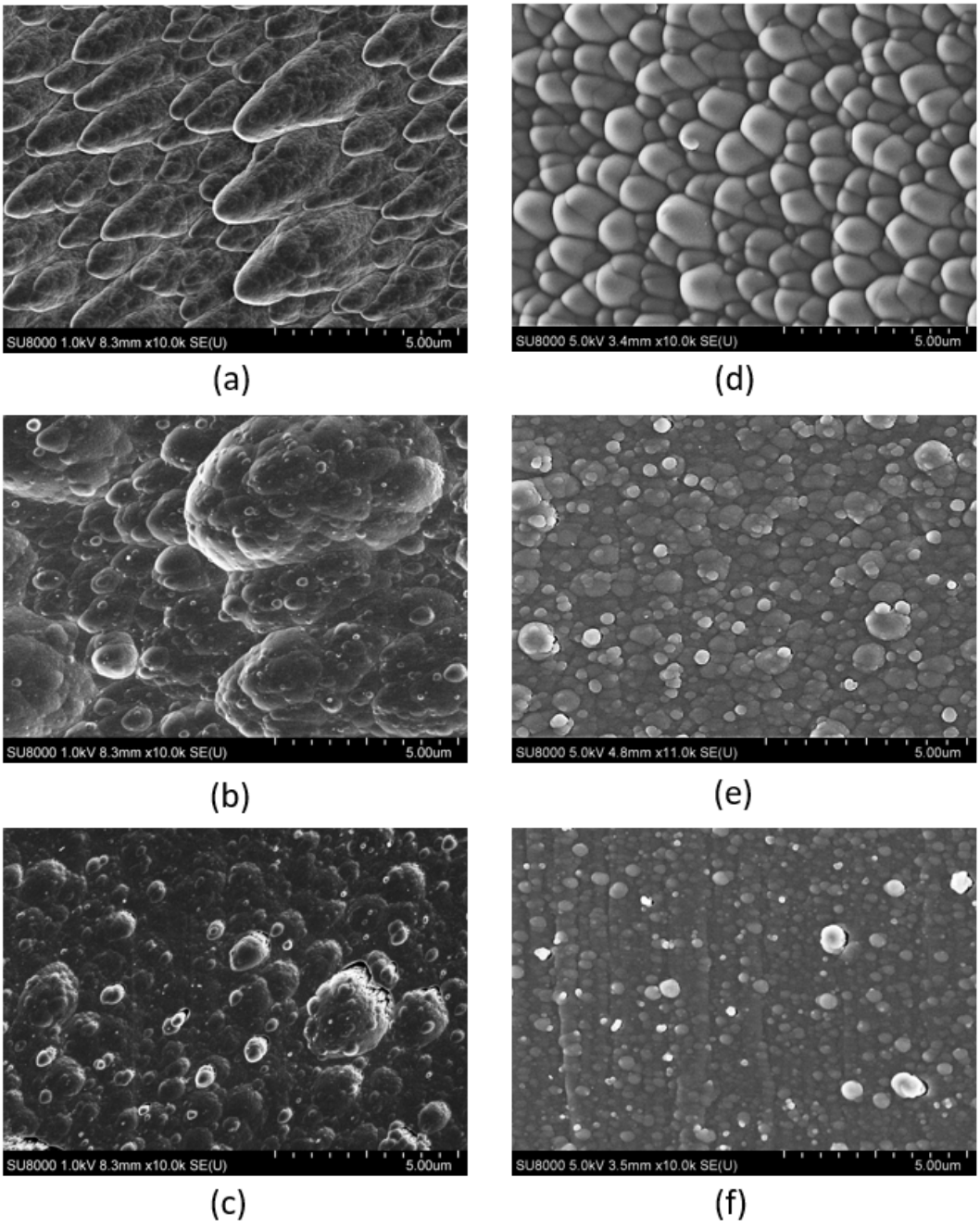

FIGURE 6.4: Scanning electron micrographs of carbon on SUS304 substrates (a-c) 4 mm from the target surface (a) After 10000 pulses (b) After 20000 pulses (c) After 30000 pulses, (d-f) 8 mm from the target surface (d) After 10000 pulses (e) After 20000 pulses (f) After 30000 pulses

TABLE 6.1: Mean particle area for d = 8 mm for increasing number of pulses

Number of pulses	Mean particle area (μm^2)
10000	0.00518
20000	0.00391
30000	0.00188

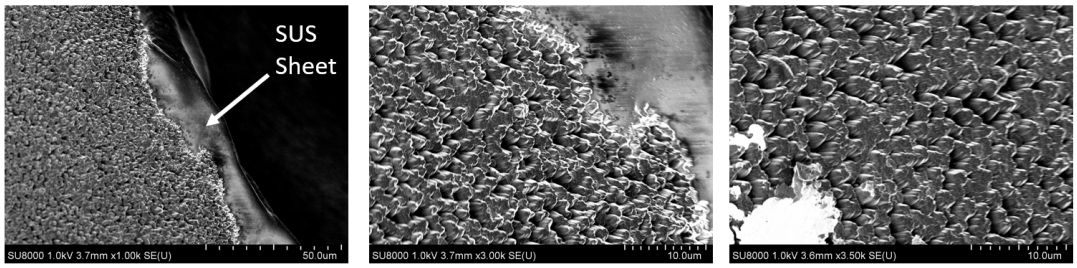

FIGURE 6.5: Scanning electron micrographs of graphite film on SUS304 substrate at a distance 4 mm from the 3h ablated target surface, deposition time: 1 h

ImageJ software by adjusting the threshold and using the Analyze Particles function, followed by obtaining a size distribution from a calibrated scale [7]. Table 6.1 shows the mean particle area obtained from Fig. 6.4 for increasing number of pulses. Decrease in mean area of about 25 percent is observed after 20000 pulses, which further decreases to 36 percent of the original particle size.

In investigating the effect of depositing on the target surface with an existing cavity, the target is ablated for 3h while rotating about the axis at 30 rpm. Then, a SUS 304 sheet is attached to the substrate holder. A polyimide tape is attached to the end of the sheet to prevent block the deposition on this region. The deposition is performed for 1 h with the all parameters kept constant. After deposition, the tape is removed and characterization is performed. An approximately 3 mm hole depth is measured from the target. Figure 6.5 shows the scanning electron micrographs of the 1h deposition of the target with 3h pre-drilling. Similar to the case in Fig. 6.4 (a-c) conical structures are observed. However, it can be observed that the protrusions overlap more than that observed from the tipped structure. The film thickness is obtained approximately 2 μm from the deposition.

In order to determine the effect of substrate on the film deposition, 1 mm thick pre-cleaned glass substrates were used, whose deposition after 30000 pulses is shown in Fig. 6.6. As with the stainless steel substrates, columnar structures were observed. Therefore, carbon is indeed deposited on the substrates and no significant damage to the substrates was observed during deposition.

Deposition at a long distance is investigated. SUS304 substrates with 0.25 mm thickness are placed 100 mm from the target surface. After 30000 pulses,

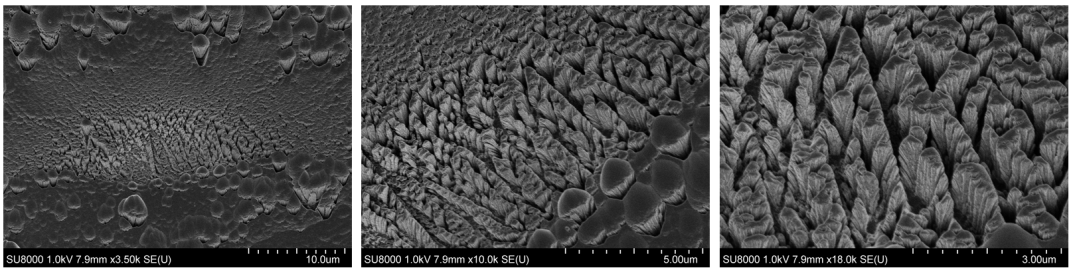

FIGURE 6.6: Scanning electron micrographs of carbon film on glass substrates after 30000 pulses at (a) 3500x (b) 10000x and (c) 18000x magnification

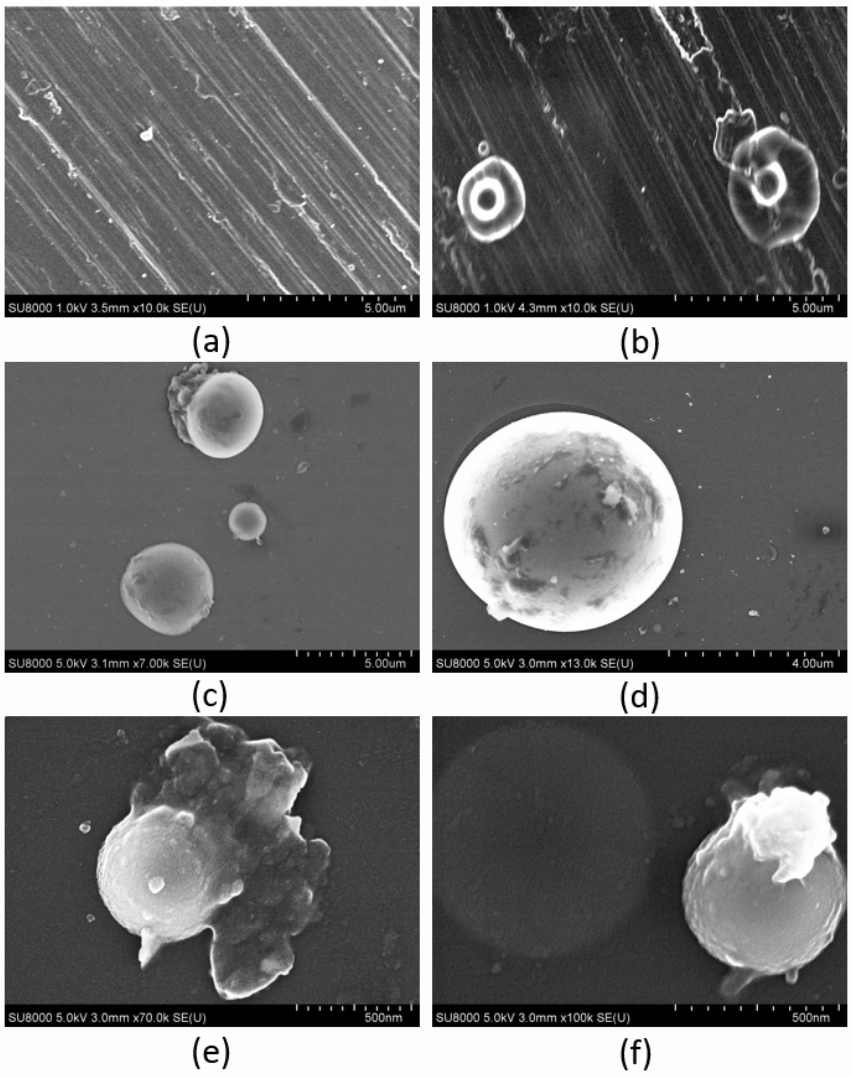

FIGURE 6.7: Scanning electron micrographs of carbon deposits on SUS304 substrates located 100 mm from the target surface, (a) After 1h deposition (b) After 1 h deposition with a 2 mm (c-f) After 3h deposition for (c) 7000x (d) 13000x (e) 70000x (f) 100000x magnifications

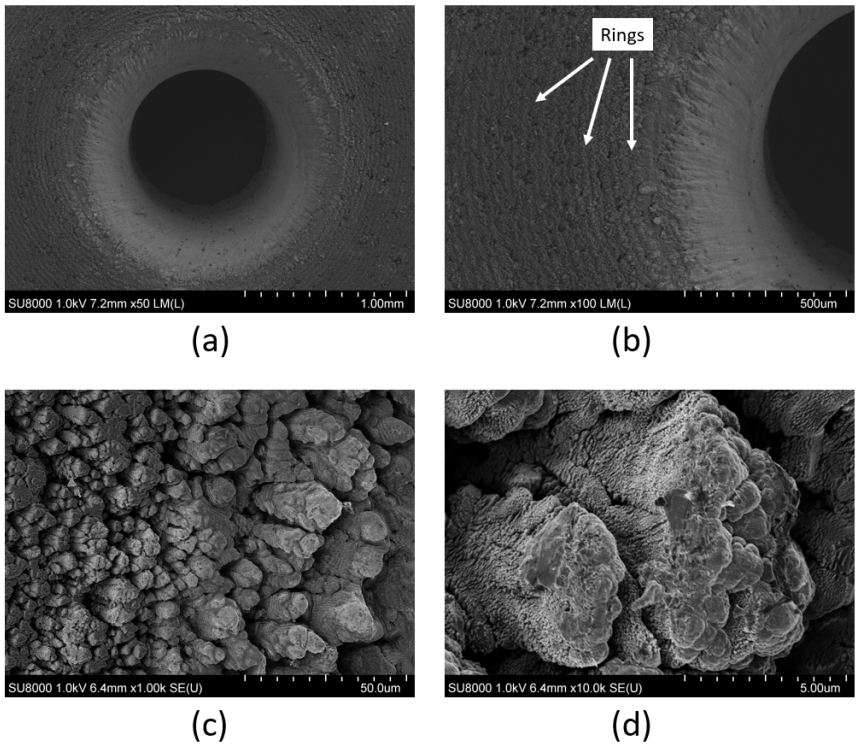

FIGURE 6.8: Scanning electron micrographs of the graphite target cavity after 30000 pulses at (a) 50x (b) 100x (c) 1000x, and (d) 10000x magnifications

no significant film formation was observed. Similarly, for 1 h deposition shown in Fig. 6.7 no significant film formation was observed. Deposition with a 3 mm cavity formed by 3 h ablation, however, spheres with diameters of approximately 1 μm were observed, as shown in 6.7(b). Figures 6.7(c-f) show the deposition after 3 h ablation. Spheres with diameters ranging from 500 nm to 5 μm are observed. In the spheres on 6.7 (e) and (f), residual carbon surrounds the particulates.

The influence of deposition on the target surface is investigated. Figure 6.8 shows the target images after 30000 pulses. Ringlike structures which are approximately 30-40 mm apart, are observed near the cavity rim. Zooming in on the ringlike structures, columnar structures are observed. However, unlike the depositions observed in the glass and stainless steel substrates, these structures have no defined shape.

Figure 6.9 shows the current signals collected from the ground and extraction plate, measured 4 mm and 8 mm from the target surface respectively. Increasing number of laser shots decrease the positive signals for both regions. After 30000 pulses, negative signals corresponding to fast electrons increase for the current collected at the back plate. The positive current signal at the back plate consists of an initial peak at 0.5 μs, followed by a broad distribution until approximately 8 μs. The positive ion peaks in both plates also shift to later times, where a significant shift occurs from after 10000 to 20000 pulses. Signals corresponding to both back and extraction plates showed increase in electron signal at 300 ns for increasing number

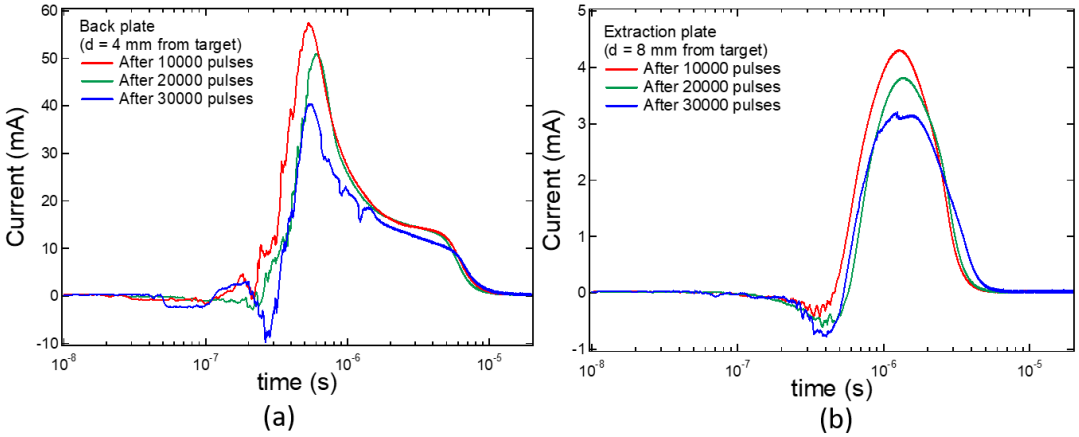

FIGURE 6.9: Current signals collected from (a) the ground back plate (4 mm from the target surface) and (b) from the extraction plate (8 mm from the target surface)

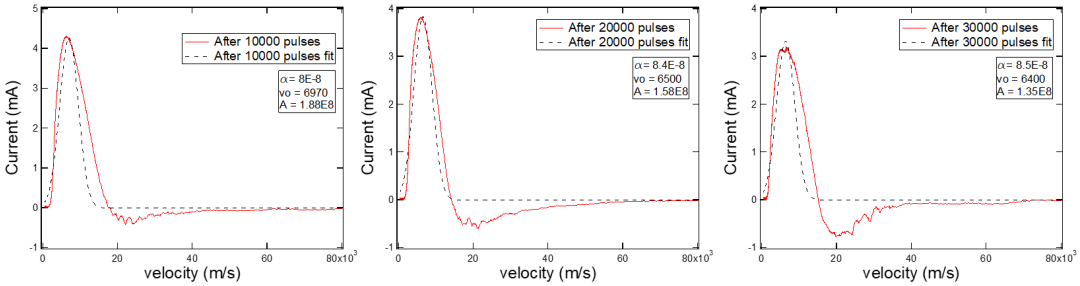

FIGURE 6.10: Current signals collected from extraction plate (8 mm from the target surface), dashed line represents Maxwellian distribution (left to right) After 10000, 20000, 30000 pulses

of pulses. For the extraction plate, the peak is detected at 1 μs, where no subsequent distribution is observed.

The time-of-flight signals collected from the extraction plate is fitted by a Maxwellian distribution given by:

$$f(v) = A\alpha^{3/2}e^{-\alpha(v-vo)^2}, \tag{6.1}$$

where α, vo are fitting parameters. The Maxwellian fit is performed using a least squares method via the GRG nonlinear method in the Solver function. In a velocity distribution the fitting parameter $\alpha = m/kT$. The width of the distribution then depends on $1/\alpha$. Figure 6.10 shows the time-of-flight signals collected by the extraction plate, along with the Maxwellian fit according to Eq. 6.1. The fitted curves shows a decrease in current, as well as a slight increase in width. From the parameter α, assuming a mass of 4×10^{-26} kg (C_2 mass), the ion temperatures of the distribution are estimated to be 36300, 34600, and 34300 K after 10000, 20000, and 30000 shots, respectively.

6.4 Discussion

In the production of carbon clusters focusing on neutral particle formation, two main pathways are first considered: laser ejection of fine particles leading to subsequent cooling, and nucleation [8], and the thermal vaporization followed by nucleation and growth. Since the laser pulse width employed is of the nanosecond order, there is sufficient time to thermalize and allowing for energy transfer to the target lattice [9]. Therefore, the explanation of thermal vaporization is considered. In the following discussions, since the detailed process of nucleation as well as optimized deposition parameters are not known, we refer to the mechanisms towards the production similar microstructures produced by laser ablation from other works.

From the deposition results, there is a significant difference in morphology arising from the substrates given only the 4 mm distance from each other. For the back plate situated 4 mm from the target surface, cone-shaped columnar structures are observed. Although there are studies which concern the formation of carbon *nanocones* [10, 11], the cones produced in those experiments are significantly smaller (< 500 nm) than that produced in the current experiments (approx. 1 μm), we obtain insights of their formation mechanisms. In the work of Zhao and coworkers, where nanocones are formed on the periphery of the femtosecond laser-ablated target, the nanocone formation is directed perpendicular to the polarization direction [11]. However, no such nanocones were observed in the target, as shown in Fig. 6.8. In the work considering the formation of microcones by Tsing-Hua, et al using femtosecond pulses under buffer gasses, the formation of microcone structures are due to the propagation of the recrystallization front in different locations. The observation region in this case is the target in which no sharp microcones were observed. A possible mechanism is then, in alignment with [9], the cause of the microcone formation is the ablation followed by plume vaporization followed by cooling on the substrate instead of the target. Another explanation, which is adopted from Ref. [13] is the occurrence of capillary forces due to melting and vaporization causing the microcone formation. When the target is ablated, melting and evaporation occurs, and the pressure difference between the target and the irradiated region induces forces that directs the melt flow. If this explanation is to be applied in the current experiment, then the neutrals from the plume would encounter such forces on the substrate from which they form the microcones. On another note, an explanation of the absence of such microstructures on the target hole is the repeated melting of the target causing only blunt, columnar structures present in the cavity periphery, as shown in Fig. 6.8c. Since the influence of heating is higher with nanosecond pulses, the cavity may have suffered repeated deformation due to continual ablation. Moreover, the microstructures on the cavity may be affected by the target rotation during ablation.

Increasing the number of pulses as shown in Fig. 6.4 b and c, the conical structures are hardly visible, and spherical particles attached to the larger

deposits could indicate the influence of the cavity as a cooling region for the ablation plume. When the cavity depth increases, the laser absorbs the laser energy, resulting to lower laser power striking the surface. Fewer neutrals get vaporized relative to a lower cavity depth and, few undergo condensation, which results to reduction in volume. This reduction in ablation also applies to ions, shown in Fig. 6.9, where the decrease in positive ion signal corresponds to decrease in the reduction in ablation.

As the substrate distance is increased, more spherical structures are observed for the deposits, as shown in 6.4 (d-f). After 10000 pulses, the drastic change in the morphology compared to that on the back plate indicates the difference in front and behind the back plate. Behind the back plate, recoil pressure from the plume interaction with the plate formed conical microstructures. Before the plume arrives the extraction plate, the plume is constricted further from the 4 mm aperture, which then diverged towards the extraction plate. Since from the high speed images of the expanding plume in Chapter 2, the plume vapor density is decreasing with distance, therefore the neutrals do not experience high vapor pressure difference compared to the back plate region, thus forming only amorphous deposits. The constriction due to the aperture may have further cooled the expanding plume. Increasing the number of pulses shows the similar trend where smaller spherical particulates are deposited on the substrate.

From the 1h deposition on a pre-formed cavity shown in Fig. 6.5, shorter conical deposits were observed. When a cavity is already formed, the pressure difference outside the cavity is reduced, since the expansion energies are lowered down. This also resulted to a dependence of conical structure morphology on the cavity, and may be utilized as a metric in measuring expansion energy losses.

At 100 mm from the target, almost no deposits, except for nano or micro-sized spheres were observed. This indicates the low amount of neutrals able to maintain its propagation at longer distance. This is also observed from the high speed images from Chapter 2, as there is a limit of expansion especially when a cavity is already formed.

From the deposition patterns for varying distances, a schematic of the plume expansion can be constructed, where, coming from an initial expansion, vapor pressure difference and nanocone formation occurs near the surface, followed by the reduction in pressure at increasing distance, leading to smaller particles.

The current signals in Fig. 6.9 shows the behavior of how charges are collected from the surface. As for the peak current, the back plate collects more than 10 times the signal, due to the distance from the target. The back plate also collects the initial propagating charges, while the extraction plate only collects the charges after these pass through the 4 mm aperture. For the back plate, the increase in negative signal with the number of pulses corresponds to increase in initial propagating electrons or light negative ions. Since there is a decrease in positive signal while an increase in negative signal, negative ions may have been formed due to increase collisions from electron attachment. Another reason for the increase in negative

signals may be the increase of electrons due to increase in the production of multiply charged ions from an increase in collisions. However, since the ion distributions all exhibit energy losses, electron production due to increase multiply charged ions may less likely to occur. Another reason further still, may be the increase in electrons which participate in recombination of atomic states, while having the same number of ionic states. From the optical emission results in Chapter 5 where an increase of continuum is observed, it is likely that the lower energy atomic states prevail than the ionic states due to collision-induced energy losses. With this stated, a maximum number of ionic states is observed for a free expansion, and as the cavity increases the energy loss of the plasma, ions are reduced, and atomic excited states recombine with the electrons. The decrease in the estimated ion temperature indicates the energy loss compared to the plume at lower number of the pulses. Although the Maxwellian distribution is able to fit the ion currents and provide temperature estimates, the thermal equilibrium condition may not be strictly valid for the laser plasma.

6.5 Summary

Carbon films at 4 mm and 8 mm target to substrate distance are produced by nanosecond pulse laser ablation of graphite. Conical structures were observed 4 mm the target, while amorphous, spherical structures were observed 8 mm from the target surface. Increasing the number of pulses leads to the deposition of smaller particulates due to plume interaction with the cavity walls as well as vapor pressure differences within the deposition regions. Charge collection at the substrate holders show decrease in positive ion current, while increase in negative signal is observed for increasing number of pulses which is attributed to negative ion and electron production when the cavity region is further increased.

References

[1] H. U. Krebs, M. Weisheit, J. Faupel, E. Süske, Scharf, T., Fuhse, C., M. Buback, Pulsed Laser Deposition (PLD) – A Versatile Thin Film Technique, in Advances in Solid State Physics, 505–518 (2003).

[2] M. J. Aziz, Appl. Phys. A (2008) 93: 579–587.

[3] J. A. Martin, L. Vazquez, P. Bernard, F. Comin, and S. Ferrer, Appl. Phys. Lett. 57, 1742 (1990).

[4] M.C. Polo, J. Cifre, G. Sánchez, R. Aguiar, M. Varela, and J. Esteve, Diam. Relat. Mater. **4** 780-783 (1995).

[5] A. Inoue, T. Seto, and Y. Otani, Carbon. **50** 1116-1122 (2012).

[6] P.M. Ossi et al., Thin Solid Films 482 2–8 (2005).

[7] C. A. Schneider, W. S. Rasband, and K. W. Eliceiri, (2012). NIH Image to ImageJ: 25 years of image analysis. Nature Methods, 9(7), 671–675.

[8] Y. A. Yang, P. Xia, A. L. Junkin, and L. A. Bloomfield, Phys. Rev. Lett. **66**, 9 1205-1208 (1991).

[9] B.N. Chicbkov, C. Momma, S. Nolte, F. yon Alvensleben, A. Tünnermann, Appl. Phys. A 63, 109-115 (1996).

[10] C. K. Tan, K. P. Loh, J. T.L. Thong, C. H. Sow, and H. Zhang, Dia. Rel. Mat. **14** 902-906 (2005).

[11] Q. Z. Zhao, F. Ciobanu, and L. J. Wang, J. Appl. Phys. **105**, 083103 (2009).

[12] T. H. Her, R. J. Finlay, C. Wu, S. Deliwala, and E. Mazur, Appl. Phys. Lett. **73**, 1673 (1998).

[13] S.I. Dolgaev, N.A. Kirichenko, A.V. Simakin, G.A. Shafeev, Quantum Electron. **37** 645 (2007).

Chapter 7

Conclusions

7.1 Main results

In this work, a time-of-flight ion mass spectrometer is designed and developed mainly for obtaining ion distributions for nanosecond pulsed laser ablation plasmas under target induced cavity confinement. The target confinement is performed by focusing the incident laser on the target surface at a shallow angle towards its axis during rotation at 10 Hz repetition rate, a method performed for the first time. The resulting target consisted of an axially symmetric cavity with 2 mm depth after 30000 pulses at 5 GW/cm^2 laser intensity. The work consisted of design modifications and electromagnetic field simulations to improve the collected signal such as installing a deflector magnet to steer the ion trajectory, einzel lens to refocus propagating ions, and retarding potential analyzer to quantify the ion energy. These modifications resulted to improvements in the resolution on the ion signals, and served as quantitative assessments of the ion energy coming from a highly non-equilibrium plasma source.

The spectrometer is also utilized for optical emission and pulsed laser deposition experiments aiming to understand the effect of cavity formation on the ion distributions. These experiments demonstrated the applications of the device for simultaneous measurement of the plasma characteristics inside and outside the cavity. In pulsed laser deposition experiments, conical structures of 2μm height are able to be formed, and substrate distance-dependent morphologies were observed, which are also dependent on the cavity formation. In the following, the main results are categorized into: electron and ion production, plasma expansion, and optical characterization.

For electron and ion production, the plasma plume consists of fast electrons followed by positive ion distribution at 5 μs time-of-flight, corresponding to C_2^+ cluster ions. Fast electrons collected 4 mm from the target surface are described by a Maxwellian distribution. Increasing laser intensities increases ablation at a logarithmic rate, which does not significantly increase after 10000 pulses. From the energy analysis using the retarding potential analyzer, ion current for the fresh target decreases for a retarding potential bias from 200 V. Positive ion distribution encounters energy losses as the cavity depth is increased, starting from a 200 eV ion distribution energy. The effect of energy loss decreases down to approximately 100 eV with the increase in cavity depth due to plasma

confinement and plasma shielding which causes the decrease in further ablation. The ion distribution is found to be sensitive with lens voltage bias, whose ion signal significantly decreased after 50 V. Positive, as well as negative ions are formed as a result of collision-induced processes, where the latter mechanism primarily involves collision-induced electron attachment leading to heavy negative ions such as C_{26}^- and C_{35}^- cluster ions, where the cluster peaks increase after 10000 shots, followed by subsequent decrease. Signals for both near (4 mm and 8 mm) and far from the target (Faraday cup, 650 mm) collected tend towards negative, leading to the reduction of positive signal.

For plasma expansion, the initial plasma consists of a glow discharge until 100 μs, followed by subsonic expansion speeds of the particles at around 110 m/s primarily directed perpendicular to the target surface. The concentration of plasma rapidly decreases with distance, where, at 5 GW/cm^2 laser intensity, the glow can be observed within 50 mm from the target surface. The plume creates a variation in the pressure near the target surface which facilitates the formation of microcones, due to the interaction of the plume with the substrates. Increasing the formation of the cavity reduces the ion energy, as well as the amount of ablated constituents, thus producing smaller and fewer neutrals. With the decrease ion production for increasing cavity formation, smaller and fewer neutrals are deposited when the number of pulses are increased.

Optical emission results performed on graphite, as well as aluminum targets revealed continuum radiation superposed with emission lines ranging up to C IV and Al IV. Continuum emission spectra along the target axis showed an apparent temperature fit of 3000 K, which was obtained by the Planck-like and sigmoidal fitting. This temperature did not change significantly for increasing number of pulses, indicating that the apparent temperature measurement is independent of emission intensity. However, continuum radiation directed perpendicular to the target axis showed inconsistencies using the fitting and was attributed to lower continuum intensities. Following the optical characterization results directed perpendicular to the target axis, decrease in ions are observed with the decrease in emission lines, as well as continuum spectra outside the cavity. Within the cavity, higher electron recombination due to higher continuum are observed. Higher continuum and lower emission line intensity indicated the contribution of plume confinement in the reduction of escaped ions, as well as radiative recombination.

In all experimental results, collision-induced energy loss is the primary mechanism of cavity formation. From the time-of-flight peak shifts, time-of-flight current decrease, ion energy decrease, to emission line decrease outside the cavity, and continuum increase within the cavity, the energy loss is due to plume confinement. From the film deposition results, plume confinement may also function as a metric on how much energy is lost near the target surface from the evolution of conical structures, apart from retarding potential analysis. However, like the typical laser ablation plasmas, the mechanisms of laser plasma formation within the cavity at the

time of formation has still not been fully determined. Therefore, further characterization is required to explain the processes occurring with the plasma confinement.

7.2 Future work

Several experiments have been performed in order to improve ion detection in the current setup. However, significant improvements still have to be undertaken to further the understanding of cavity produced plasmas. One of such improvement is the mass resolution enhancement of the device. Despite having determined C_2^+ cluster ions from the main plume, heavier cluster ions may have been present, whose mass needs to be accurately defined. Another needed improvement is the determination of optical emission spectral evolution. Since the methods employed only involved spectral collection in the accumulation mode, the continuum as well as the emission line evolution may be recorded to understand the time development of the plasmas escaping the cavity, or forming within the cavity. Finally, a needed improvement is the determination effect of inner cavity confinement in the hole. When the cavity is confined, investigating the time-of-flight and optical emission spectra on the condition of further enhanced confinement by magnetic fields would increase the understanding on the effect of electron confinement on the resulting plasma species.